AN EXPERIMENTAL INVESTIGATION OF THE EFFECT OF A DENSITY GRADIENT ON SHEAR LAYER INSTABILITY

Thesis by

Robert F. Davey

In Partial Fulfillment of the Requirements

For the Degree of

Doctor of Philosophy

California Institute of Technology

Pasadena, California

1971

(Submitted March 12, 1971)

ACKNOWLEDGMENTS

The author wishes to express his appreciation for the guidance of his advisor, Professor Anatol Roshko, and for the timely assistance of Professor Donald Coles and the many helpful suggestions of Dr. Garry Brown. The author is also grateful for the instruction in experimental techniques given by Dr. Ivar Tombach.

The assistance of Mr. Lewis Balthasar and Mr. Ray Wagoner in the construction of experimental equipment and the dedicated service of Mrs. Geraldine Krentler, who typed the manuscript, is gratefully acknowledged.

The author is indebted to the National Science Foundation for financial assistance and to the Office of Naval Research for the support of the research program.

The deepest appreciation is expressed for the patience and encouragement of the author's wife, Julie.

ABSTRACT

Measurements of mass flow rate and mean density have been made in separated laminar boundary layers having large transverse density gradients. A 3/8 in. by 1½ in. rectangular half-jet was used to generate a two-dimensional shear layer and the density heterogeneity was produced in an incompressible flow by exhausting one gas into a reservoir of another gas having a different molecular weight. Two Freons were used having a density ratio of 1.98 and unique properties which permitted the measurement of the mass flow rate in all mixtures of the gases with a single hot wire.

Mean density and mass flow rate profiles were compared to the Holmboe model used in theoretical hydrodynamic stability analyses. Fluctuations in the mass flow rate were analyzed and the frequency, wave number and amplification rate of the most unstable oscillation were measured and compared to theoretically predicted values. The oscillations were found to have a higher amplification rate, lower wave number and lower frequency than homogeneous flow when the lighter gas flowed into the heavier one, in agreement with the theoretical predictions. Opposite trends were observed with the heavy gas flowing.

The development of harmonic frequency oscillations in the non-linear region is discussed briefly.

TABLE OF CONTENTS

TABLE OF CONTENTS (cont.)

LIST OF TABLES

LIST OF FIGURES

LIST OF FIGURES (cont.)

LIST OF FIGURES (cont.)

I. INTRODUCTION

Interest in the stability of the separated boundary layer dates back almost a century to the work of Lord Rayleigh. Only rather recently, however, has the problem been modeled with sufficient accuracy to bring the results of theoretical and experimental investigations into essential agreement. Freymuth's results (Ref. 1) in particular indicate that, at least for the homogeneous, incompressible case, the problem is now well in hand. An enlightening survey of the progress made in understanding the homogeneous free shear layer has been prepared by Michalke (Ref. 2). In the same paper, Michalke comments on the limited progress in the non-homogeneous case and specifically notes the absence of experimental work.

Most of the theoretical investigations of the heterogeneous free shear layer have been devoted to examining the effect of buoyancy forces on stratified flows, no doubt because of the obvious applications to atmospheric and oceanographic phenomena. The stability criteria first proposed by Taylor (Ref. 3), namely that the velocity gradient be everywhere non-zero and that the Richardson number exceed 1/4, were verified by Miles (Ref. 4) and others.

Discussions of the case where the Froude number is large and the dominant heterogeneous effects are due to

inertial forces produced by the density gradient have been less numerous. Gropengiesser (Ref. 5) analyzed the stability of compressible shear layers for Mach numbers up to three and for several temperature ratios. Menkes (Ref. 6) analyzed an incompressible flow with a hyperbolic tangent velocity profile and an exponential density variation (i.e., $\bar{\rho} = \exp(-2\,Ly)$). He reached the misleading conclusion that any density gradient would reduce the disturbance amplification rate.

Using the physically more realistic flow model proposed by Holmboe, namely:

$$\bar{u} = 1 + \tanh y$$

$$\bar{\rho} = \exp(-\beta \tanh y),$$

Maslowe (Ref. 7) found that a density gradient could either increase or reduce the disturbance amplification rate depending upon its direction and magnitude. Specifically, an increase could occur when the density was lower in the high speed portion of the shear layer (i.e., $\beta > 0$). Maslowe's analysis included cases for both large and small Froude number and examined both temporally and spatially amplifying waves.

The present research effort was an outgrowth of a continuing effort at Caltech directed towards developing an understanding of separated flows. The development of a

new facility for studying the turbulent, heterogeneous, two-dimensional mixing layer led to an interest in the laminar transition region between the separation point and the developed turbulent flow. Spark shadowgraphs taken by Tombach (Ref. 8) showed that the transition to turbulence of an axisymmetric jet was markedly affected by a density heterogeneity. Photographs of a helium jet exhausting into air showed a very rapid transition to turbulence while those of an air jet flowing into helium showed a gradual transition with a pronounced wave-like structure. More recent shadowgraphs taken of the turbulent mixing layer revealed that a similar, large scale structure exists within the turbulent region and persists relatively far downstream. It was felt that the differences in transition characteristics were related to the stability properties of the shear layer formed at the nozzle exit. Consequently, an apparatus was built to study the shear layer itself with the following goals in mind. First, measurements of mean velocity and density were desired for comparison with those used in theoretical analyses, particularly the Holmboe profiles used by Maslowe. Second, a determination of the disturbance amplification rate was sought to aid in understanding the jet transition phenomenon. Finally, measurements of the instability wave parameters, including frequency, wave-length, phase variation, and the transverse variation of

the fluctuation amplitude, were desired, especially after Maslowe's work provided some basis for comparison.

The shear layer was formed by exhausting a 1½ in. by 3/8 in. rectangular half-jet of one gas into a closed tank containing a second gas with a significantly different molecular weight. The jet velocity was about 5 ft/sec for the heavy gas and 10 ft/sec for the light gas. All tests were made with the tank pressure set at 7 psia to achieve the desired combination of Reynolds and Froude numbers.

Because of the very small dimensions involved (the shear layer was about one millimeter thick at the nozzle exit) and the frequency response needed for the measurement of wave parameters, sensor requirements were particularly stringent. In fact, such time response and spatial resolution could be achieved only with a hot wire aligned spanwise to the flow. Unfortunately, a single hot wire is, in general, unusable in a heterogeneous flow because the variations in the signal due to the changing fluid properties (e.g., thermal conductivity, viscosity, etc.) cannot be distinguished from changes due to the flow parameters that one wishes to evaluate. Although some success has been achieved recently by Way and Libby (Ref. 9) using two wires and mixing the signals to obtain simultaneous velocity and density readings, their probes required crossed sensors and, therefore, lacked the desired spatial resolution. An

examination of the equation governing hot wire performance indicated that a single wire could be used to measure mass flow rate in a heterogeneous medium if the gases possessed certain unusual properties. A search revealed two Freons having the desired characteristics and a density ratio of 1.98.

Hot wire measurements were made at several downstream stations for the two flow cases: heavy gas (Freon 114) exhausting into light (Freon 22) and light gas into heavy. The traverses covered the region where the disturbances grow exponentially and extended downstream into the so-called non-linear region. Signals were recorded on magnetic tape and later converted to digital form for computer processing.

Mean density profiles were obtained at several downstream locations using a density sensitive aspirating probe similar in design to those developed by Brown and Rebollo (Ref. 10).

Following techniques developed by Sato (Ref. 11) and used by Browand (Ref. 12), Freymuth and others, a loudspeaker was used to excite the shear layer oscillations at a particular frequency. Browand showed that such excitation does not change the character of the flow except for narrowing the frequency band of the disturbance oscillations. The technique simplifies the analysis of the flow oscillations by providing a known fundamental frequency and an accurate

phase reference.

Sections II through V contain detailed descriptions of the experimental equipment and the procedures used to acquire and process the data. The results of the experiments are presented in section VI.

II. EXPERIMENTAL EQUIPMENT

2.1 Flow Geometry

A two-dimensional shear layer with a large transverse density gradient was produced by exhausting one Freon from a rectangular half-jet into a sealed tank containing a second Freon with a different molecular weight. The rectangular jet was formed at the exit of a two-dimensional circular-arc nozzle which contracted fifteen-to-one to the exit dimensions, 3/8 in. by 1½ in. Three of the four nozzle faces were extended downstream using flat walls. The flow from the remaining 1½ in. face was allowed to separate to form the desired shear layer (Fig. 1). The resulting flow geometry was similar to that produced downstream of a rearward facing step.

A slide valve was installed across the nozzle to keep the different gases separated until the flow was turned on (Fig. 2). The slide was machined from 3/16 in. brass plate. It was carefully fitted to a stainless steel guide to make a nearly gas-tight fit. The open position of the valve was adjusted to provide a smooth alignment with the back wall of the nozzle. Minor difficulties were experienced with leaking and jamming but the complete absence of obstructions to the desired flow geometry made the valve design desirable.

The valve was actuated by a single-action air cylinder, spring loaded to the closed position. Compressed air was

used to open the valve and a vacuum was used to assist the spring in closing it. Solenoid valves controlled the gas flow to the air cylinder.

2.2 Settling Chamber

A concerted effort was made to reduce the turbulence in the jet flow to the lowest possible level. Because of the relatively small size of the apparatus, some problems were encountered different from those associated with turbulence reduction in larger wind tunnels.

A relatively large settling chamber was placed upstream of the circular-arc nozzle (Fig. 3). Two very fine cell honeycomb sections, three inches long with cells measuring about .02 in. by .03 in., were inserted upstream of the nozzle. They were fabricated by laminating sheets of finely corrogated stainless steel and thin, flat stainless steel. Two large cell honeycomb sections were placed further upstream to act as flow straighteners and to support fine mesh screens. These sections improved the uniformity of the flow entering the fine honeycomb.

The four honeycomb sections and the contraction reduced the turbulence level only to .3%. Using smoke injection, flow instabilities were found near the nozzle walls immediately downstream of the fine honeycomb. A hot wire velocity survey indicated that a 1/8 in. wide, high-speed free jet was present about 1/4 in. from the nozzle

walls, apparently caused by a variation in the pressure drop across the honeycomb. Triangular flow deflectors placed upstream of the final honeycomb section smoothed the velocity profile entering the nozzle, eliminated the regions of unstable flow, and reduced the turbulence level to .25%.

A spectral analysis indicated that the remaining fluctuations were concentrated at a single frequency near 2500 Hz. A hot wire survey along the nozzle centerline showed a pattern of nodes and peaks, indicating that the fluctuations were acoustic. A number of unsuccessful attempts were made to attenuate the sound. These included trying different nozzle shapes and a variety of sound absorbing materials. The source of the sound was eventually identified as the gas entry port far upstream. A plastic foam ring was fabricated and placed in the entry duct. This apparently prevented the formation of sound producing vortices at the exit of the duct. The acoustic fluctuations were eliminated and the turbulence dropped to .17%.

Oscilloscope traces of the remaining fluctuations showed that they were intermittent with a frequency near 60 Hz. An AC solenoid valve was identified as the source. Between the valve and the nozzle were four feet of tubing, the foam ring and a two foot contracting flow chamber containing four honeycomb sections and five fine mesh screens, yet the oscillations were clearly evident at the

jet exit. Moving the valve upstream of the flow regulator eliminated the oscillations and reduced the fluctuation level to an acceptable .06% of the jet velocity.

Two lessons applicable to the design of small, low turbulence flow devices were learned from the problems encountered. First, acoustic fluctuations can occur at relatively high frequencies and amplitudes. Second, fluctuations, once produced, are very difficult to attenuate in the distances available. They are better handled by identifying and then eliminating the sources.

2.3 Gas Controls

Gas was supplied from cylinders containing liquid Freon. Electrical heating tapes were used to replace the heat lost from boiling. The heating rate was set to maintain a vapor pressure close to that produced by the ambient temperature.

The jet flow rate was controlled by a pressure regulator and a sonic needle valve. The relationship between the jet velocity and the needle valve setting and flow pressure was determined from calibrations made using a 1/8 in. diameter pitot tube and a Datametrics Barocel electronic manometer. Measurement of the jet velocity was not trivial because the flow was entering a sealed tank and, consequently, the static pressure was increasing. Although the increase was not large enough to alter the

shear layer characteristics being studied, it was very large compared to the dynamic pressure produced by the jet. Thus, the fast time response of the electronic manometer was needed to obtain accurate differential pressure measurements. In addition, the static pressure source was made identical in diameter and length to the pitot tube and was connected to the manometer with the same length and size of tubing. This was done to keep the time response of the two pressure sources identical and further improve the accuracy of the measured pressure difference.

Prior to each run, the entire system was evacuated. The settling chamber and the tank were then filled simultaneously with the different Freons. The filling rate was set to keep the pressure in the two sections equal, thereby reducing leakage across the slide valve. The final pressure could be held at any level since the system was completely sealed. All runs were made at 7 psia to obtain the desired combination of Reynolds and Froude numbers.*

2.4 Tank

The enclosing tank was about 2½ feet high and had a 15 inch diameter. Figure 4 is a drawing of the jet facility showing both the tank and the settling chamber.

Windows in the tank were used for flow visualization studies. The inside of the tank was lined with polyurethane

---

* This is discussed in detail in section 4.1.

foam to reduce sound reflections and lower the background noise level. A two-directional traverse was installed which allowed the positioning of instrumentation to accuracies of $\pm$ .001 in. A small fan was installed to blend the gas mixtures used for calibrating the density sensitive aspirating probe. The loudspeaker used to excite the shear layer oscillations was mounted at the bottom of the tank. The speaker was driven by an audio oscillator.

2.5 Electrical Controls

Because of the steadily increasing tank pressure and the contamination of the tank gas by the jet gas, the running time was limited to about two seconds. This made on-line data processing infeasible. Therefore, all data signals were recorded on magnetic tape and processed later.

A series of relays and timing circuits was used to interface the tape recorder with the jet facility and make the operation of the experiment virtually automatic. A run was initiated by starting the tape recorder. When the tape reached its operating speed, a signal was generated by the recorder which was used to turn on the flow and trigger the timing circuits. After a preset delay, a stop command was sent to the recorder which, in turn, sent signals to turn off the flow and reset the timing circuits. The running sequence is summarized in table 1.

III. INSTRUMENTATION

3.1 Hot Wires

Although hot wires have been used with great success for measuring the temperature and velocity in homogeneous flows, their use in heterogeneous media is complicated by the fact that the signals produced are dependent upon the properties of the fluid as well as the flow parameters.

Following an analysis by Corrsin (Ref. 13), several investigators have used sensors with two or more hot wires, relying upon differences in overheat, length and wire diameter to obtain different sensitivities to composition and velocity. Recently, Way and Libby (Ref. 9) have obtained a usable calibration with such a probe in mixtures of helium and air. Unfortunately, even with minimum wire lengths and spacing, the smallest dimension of a probe using two wires would be at least one half millimeter. Since the thickness of the shear layers being investigated was only one millimeter in some places, such a sensor would span far too large a portion of the flow. Adequate spatial resolution could be obtained only by using a single wire oriented spanwise.

The relationship between a hot wire signal and the flow parameters is given by some form of King's law, which may be expressed as:

$$Nu = A + B\ Re^{n}$$

with: $Nu = \frac{e^2}{r_w \pi l k \Delta t}$; e = voltage across wire

r_w = wire resistance

l = wire length

k = thermal conductivity

Δt = overheat

$Re = \frac{\rho_f u d}{\mu_f}$ d = wire diameter

A,B = calibration constants

The power law exponent, n, was given as .45 for the applicable Reynolds number range by Collis and Williams (Ref. 14). This value was verified by the present calibrations. The subscript "f" indicates that the property is evaluated at the "film" temperature which is the mean of the wire and fluid medium temperatures.

If the relation is rewritten to represent a particular sensor operating at a fixed overheat, the overheat and all the parameters describing the wire can be included in the calibration constants leaving:

$$e^2 = A*k + B* \frac{k}{\mu_f{}^n} (\rho u)^n$$

If two gases could be found with equal thermal conductivities and viscosities, a single hot wire could be used to provide a measurement of mass flow rate in all mixtures of the gases. Since the shear layer experiments sought to determine the effect of a density gradient, a large difference in molecular weight was also desired. In

general, these requirements are incompatible since the thermal conductivity usually decreases with increasing molecular weight. However, two Freons were found with a density ratio of 1.98 which nearly satisfied the requirements. Their properties are summarized in table 2.

Several calibration experiments were performed to verify the theoretical predictions. In every case, the data fell within the variation predicted by the theory. The probe used was the same one employed in the shear layer experiments. The hot wires were 90% platinum, 10% rhodium, with a diameter of .0001 in. Three parallel wires, each one millimeter long and spaced one millimeter apart, were mounted on the probe. The wires were operated at a $300^{\circ}F$ overheat using Thermosystems constant temperature hot wire equipment. The results of one of the calibration tests which covered the mass flow rates used in the shear layer experiments are shown in figure 5. The center dashed line is a least-squares fit to all the data points. It is bounded by lines showing the predicted variation due to the small inequalities in the thermal conductivities and viscosities.

Although the results were positive and the technique was considered usable, it should be noted that a certain inherent uncertainty remains in the measured mass flow rate. Given a particular signal voltage, the error introduced by the difference between the corresponding mass flow rates

for pure Freon 22 and pure Freon 114 increases from about $\pm$ 1.6% of the jet mass flow rate in the low speed portion of the shear layer to as much as $\pm$ 3.6% in the high speed region. This inherent inaccuracy was the fundamental limitation in the present experiments.

3.2 Density Sensitive Aspirating Probe

An aspirating probe similar to those developed by Brown and Rebollo (Ref. 10) was used to measure mean density. The operation of the probe is based upon the relative insensitivity to upstream velocity of the mass flow rate through a sonic throat. The one-dimensional, isentropic, perfect gas relations give *:

$$\frac{\rho^*}{\rho_o} = \left(\frac{2}{\gamma + 1}\right)^{\frac{1}{\gamma - 1}} \quad ; \quad \frac{u^*}{a_o} = \left(\frac{2}{\gamma + 1}\right)^{\frac{1}{2}}$$

$$\rho^* u^* = \rho_o a_o \left(\frac{2}{\gamma + 1}\right)^{\frac{\gamma + 1}{2(\gamma - 1)}}$$

$$= \rho_\infty a_\infty \left(\frac{2}{\gamma + 1}\right)^{\frac{\gamma + 1}{2(\gamma - 1)}} \frac{\rho_o}{\rho_\infty} \frac{a_o}{a_\infty}$$

$$= \rho_\infty \sqrt{\gamma R T_\infty} \left(\frac{2}{\gamma + 1}\right)^{\frac{\gamma + 1}{2(\gamma - 1)}} \left(1 + \frac{\gamma - 1}{2} M_\infty^2\right)^{\frac{\gamma + 1}{2(\gamma - 1)}}$$

Thus, for small free stream Mach numbers and uniform

---

* The superscript * refers to sonic throat conditions. The subscripts o and ∞ refer to total and free-stream conditions respectively.

temperatures, the mass flow rate is dependent only upon the properties of the gas (i.e., ρ_∞, γ, R).

Since the signal from a hot wire is related to the mass flow rate over the wire and the gas properties, it is possible to obtain a unique calibration for various mixtures of two gases by placing a hot wire downstream of a sonic throat.

The probe design is shown in figure 6. The construction is similar to that described by Brown and Rebollo. The only significant modification was the use of an extended narrow neck to reduce to a minimum the disturbance to the flow caused by the probe. The small sonic orifice was formed by carefully softening the end of the narrow section in a flame.

Although Brown and Rebollo reported very large signals when the probe was used in helium and nitrogen, the Freons used in the present experiments lacked the large difference in thermal conductivity and, therefore, yielded far smaller signals. Typically, the voltage across the wire would change only .05 volts from pure Freon 22 to pure Freon 114. Nevertheless, a repeatable calibration was obtained as shown in figure 7.

The small signals limited the accuracy of the density measurements to about $\pm$ 2% of the mean density and made infeasible any attempt to measure density fluctuations.

3.3 Magnetic Tape Recorder

All data signals were recorded on one inch magnetic tape using a Bell and Howell VR 3400 recorder. The machine has provisions for seven channels of FM recording and four channels of direct recording.

Signals from four hot wire anemometers, the electronic manometer and the audio oscillator used to drive the loudspeaker were recorded on six of the FM channels. The last FM channel was used to record a control signal needed for data processing.

Playback tape speed was controlled to $\pm$ .02% by a phase locking system tied to a 200 kHz signal recorded automatically on one of the direct channels. The other three direct channels were not used.

The recording amplifiers used for the hot wire signals were set for the maximum sensitivity, $\pm$ .7 volts full scale. Mercury batteries were used to subtract most of the DC voltage from the hot wire signals, leaving an input which stayed within the amplifier limits. This was done to reduce the playback error. The linearity specifications for the recorder guaranteed $\pm$ .5% of the full scale voltage along a best fit line passing through zero. Using the highest sensitivity, this gave a $\pm$ .0035 volt accuracy. However, calibration tests showed that most of the error was due to zero shifting. By recording known voltages near the full

scale limits and using them to calibrate the playback, the accuracy was improved to better than $\pm$ .002 volts. This compared favorably with the noise level and drift of the hot wire equipment.

3.4 Electronic Manometer

A Datametrics electronic manometer and Barocel differential pressure sensor were used to measure the jet velocity, as described in section 2.3, and to measure the pressure level of the acoustic excitation. The sensitivity of the manometer could be set as high as .01 mm Hg/volt, sufficient for an accurate evaluation of the sound levels used in the experiments.

The time response of the manometer was adequate for evaluating the 100 to 200 Hz frequencies used for forcing. One sensor port was fitted with a long, 1/4 in. diameter plastic tube with a .010 in. diameter orifice at the end. This reduced the frequency response of the port essentially to zero while keeping the average differential pressure across the ports small. The open port then became the sound pressure sensor.

Readings were taken to determine the speaker driving voltage needed to produce a sound pressure level of about 75 db (i.e., rms pressure level of 1.05 dyne/cm^2) at the excitation frequency. Subsequently, the sound level was maintained by monitoring the voltage and frequency of the

audio oscillator output.

3.5 Other Instrumentation

The temperature of the jet gas was monitored with a thermocouple located in the settling chamber. With the heating tapes set to keep the vapor pressure of the Freon near the level obtained at the ambient temperature, no temperature changes were observed during the experiments.

Standard dial pressure gauges were used to monitor the tank pressure and set the flow pressures for the jet gas and the gas used to fill the tank. In addition, a gauge was used to monitor the pressure difference across the slide valve during the filling operation.

IV. EXPERIMENTAL PROCEDURES

4.1 Selection of Flow Rates

Spark shadowgraphs were used to evaluate the flow qualitatively and to plan the experiments. A spark source was placed at the focal point of an eight inch parabolic mirror to produce a parallel light beam. The light was directed through a tank window, across the flow field and onto a sheet of film mounted on the opposite window.

Pictures of air and helium flows showed the same transition characteristics that had been observed in the axisymmetric jet photographs taken by Tombach (Ref. 8). The shear layer that formed when helium flowed into air became turbulent very quickly while the layer that formed when air moved into helium at the same Reynolds number showed a gradual transition with a definite wave-like structure (Fig. 8). The shadowgraphs also showed the expected shortening of the transition distance when the Reynolds number was increased (Fig. 9).

The first pictures of the flow using the Freons showed that, at the selected flow rates, the transition distance was very short (Fig. 10). This was due to the higher Reynolds numbers produced by the dense gases. The short transition distance would have made the measurement of disturbance amplification rates and other parameters describing the downstream development of the flow very

difficult.

When the velocity was lowered to reduce the Reynolds number, buoyancy effects became evident. The shear layers developed a pronounced curvature, toward the jet when the heavy gas flowed into the light and away from the jet in the opposite case (Fig. 11). An analysis of the equations governing the shear layer stability showed that buoyancy forces could be neglected if the Froude number was much greater than one with:

$$Fr = \frac{U_o^2}{g\delta} \; ; \quad U_o = \text{wave speed} \simeq \tfrac{1}{2} \text{ jet speed}, \quad \delta = \text{shear layer thickness}$$

To make Fr $\simeq$ 100, a velocity of about 150 cm/sec was required. Therefore, the Reynolds number could be reduced only by lowering the tank pressure. With the pressure set at 7 psia, shadowgraphs showed that the transition distance was adequately long (Fig. 12).

The Reynolds number at these conditions and with Freon 114 flowing was about 120 with:

$$Re = \frac{\rho U \theta}{\mu} \; ; \quad \theta = \text{shear layer momentum thickness}, \quad U = \text{jet velocity}$$

Freymuth (Ref. 1) showed that the flow could be considered inviscid if the Reynolds number was greater than about 60.

The flow rate for Freon 22 was set to give the same momentum thickness Reynolds number. This required a velocity of 330 cm/sec with the tank pressure at 7 psia. The resulting Froude number was over 300.

A summary of the selected flow conditions and estimated non-dimensional parameters is given in table 3.

4.2 Selection of Running Time

High speed motion pictures were taken to study the starting process of the jet flow and to determine the time required to reach a relatively steady state. The pictures were taken with a Redlake Hycam camera operating at 1000 frames per second. Kodak estar base 16 mm film was used. The parabolic mirror was used with a mercury vapor lamp to produce a continuous parallel light source. The light was projected through the flow region and onto a ground glass. The camera was then focused on the ground glass image.

The pictures brought out two serious problems. First, the starting process was long and complex. Steady conditions were not reached until almost a second after the flow was turned on. Large amplitude oscillations were caused by the flow regulator diaphragm which "hunted" before stabilizing at the delivery pressure position. A better regulator was installed but the starting time could be reduced only to .7 seconds with Freon 114 flowing and

.5 seconds with Freon 22.

The second difficulty involved excessive contamination of the reservoir gas when the lighter gas, Freon 22, was flowing into the heavier gas. Although the buoyancy forces were not great enough to affect the shear layer stability characteristics, they did cause the light gas to float up from the low speed portion of the shear layer into the entrainment flow region.* The problem was solved by inverting the entire jet facility for the runs where Freon 22 flowed into Freon 114. The light gas then floated away from the entrainment flow region leaving it virtually uncontaminated even after three seconds of running.

The final determination of the running time was made using tape-recorded hot wire signals. A hot wire was placed in a position where the instability oscillations were large but still nearly sinusoidal. The recorded signal was played back at 3 3/4 inches per second (i.e., 1/32 of the recording speed) into an x-y plotter. The plots showed that the violent oscillations from the starting process decreased continuously, becoming negligible after about .7 seconds. The flow was then reasonably steady except for a slight drift caused by the slowly increasing static pressure. The interval between .8 and 1.4 seconds after

---

* The "entrainment flow region" refers to the area adjacent to the low speed portion of the shear layer from which gas is entrained by the jet.

the flow was started was selected as most representative. Slightly over one half second of the recorded signal was used in the actual processing.

A time delay circuit was set to close a relay .8 seconds after the flow was started. The resulting step signal was recorded on the magnetic tape and was used to trigger digitizing equipment during the data processing.

A second time delay circuit was set for 1.7 seconds and used to stop the recorder and shut off the flow. The extra running time was provided to allow for small variations in the timing circuits.

4.3 Jet Velocity Profile Measurements

Hot wire velocity surveys were taken across the jet in both the transverse (y) and spanwise (z) directions. Velocity variations in the core of the jet (i.e., between the wall boundary layers) did not exceed one percent. A transverse profile taken one half millimeter downstream is shown in figure 13.

4.4 Measurement of Natural Oscillation Frequency

A downstream station was first located where the shear layer oscillations had amplified enough to give a strong hot wire signal but were still reasonably sinusoidal. Hot wire signals were then recorded at about 36 points across the shear layer. The tape was played back at 3 3/4

inches per second (i.e., 1/32 of the recording speed) into an x-y plotter. The oscillation frequencies were thereby reduced from about 200 Hz to about 6 Hz, well within the capabilities of the plotter.

The plotter was first calibrated using a previously recorded signal of known frequency. Traces were then made of the hot wire signals. The plotter was started when the delayed step signal changed level, indicating the beginning of the usable data. The time interval for about 75 cycles was computed from the measured plotting distance and the calibration. An average frequency was thereby determined.

An accurate determination of the frequency could be made at only about five of the 36 points. The other signals had either too small a fluctuation amplitude or wave shapes too distorted to give an accurate cycle count.

A typical trace used for the computations is shown in Fig. 14.

4.5 Selection of Sound Levels

Acoustic forcing was used to provide a frequency and phase reference for the analysis of the shear layer oscillations. The sound level was set high enough to provide a definite relationship between the shear layer oscillations and the speaker signal but not high enough to distort or significantly amplify the flow fluctuations. The forcing frequency was set at or near the previously determined

natural oscillation frequency.

A hot wire was again placed at a point where the oscillations were large but sinusoidal. The hot wire signal and the output from the audio oscillator were fed into a dual beam oscilloscope whose sweep was triggered by the audio oscillator. The sound level was increased until the hot wire signal showed a definite relation to the forcing. Short flow bursts were used for checking. The jet facility was pumped out whenever reservoir contamination became evident. The voltage input to the speaker was noted and a full run was made after the system was evacuated and refilled. Photographs of the oscilloscope traces were taken during the run.

The sound level was then increased until the amplification of the shear layer oscillations by the acoustic forcing first became noticeable. The oscillator voltage was again noted. The voltage was then set midway between the two recorded levels and the system was again evacuated and refilled. Photographs of the oscilloscope traces were taken during the next run to evaluate the effect of the forcing. If the traces were satisfactory, the resulting sound level was measured by procedures described in section 3.4 and used for the subsequent experiments.

The procedure was accomplished for the three flow situations discussed in the following sections. In each case, the resulting sound level was close to 75 db.

Freymuth (Ref.1) showed that the instability characteristics were independent of the sound pressure level between 70 and 100 db.

4.6 Homogeneous Flow

Preliminary experiments were conducted using Freon 22 as both the jet and reservoir gas. Since accurate experimental measurements for homogeneous flows had been made previously by Sato, Browand, Freymuth and others, it was felt that sufficient comparative information existed to verify the validity of the experimental and data processing procedures.

The natural oscillation frequency was first measured and used to determine the appropriate sound forcing amplitude.

Calibration voltages were recorded on the channels used for hot wire signals. The hot wires were then calibrated at six flow rates.

Hot wire readings were taken at four downstream stations which covered the region where the disturbance oscillations grew exponentially. Between 12 and 15 runs were made at each station to obtain 36 to 45 measurements from the three hot wires. After each run, the excess gas was pumped out to bring the tank pressure back to 7 psia.

The operation of the jet facility was phased with the recorder as described in section 2.5. The timing

circuits were set for the intervals to be used in later heterogeneous experiments.

4.7 Density Profiles

The density sensitive aspirating probe was calibrated in the tank using mixtures of the two Freons. The mixtures were prepared by first evacuating the tank and then refilling it with the desired partial pressures of the gases to a total pressure of 7 psia. The mixture was then blended with the small fan and the hot wire voltage was noted. After computing the densities from the partial pressures, a calibration curve was immediately determined (Fig. 7).

Density profiles were evaluated with Freon 114 flowing into Freon 22 at five downstream stations. About 20 measurements were taken at each station.

Prior to the first run, the facility was evacuated and the sections were refilled with the appropriate gases. The system was recharged after every third run since no contamination could be detected by the probe until four or five successive runs had been made. The heavy Freon 114 apparently settled to the bottom of the tank and mixed very little with the reservoir gas. The tank pressure was pumped back down to 7 psia after each run, however.

Six profiles were evaluated with Freon 22 flowing into Freon 114. For these runs, the jet facility was inverted to prevent excessive reservoir contamination. Otherwise,

the experimental procedures were unchanged.

The hot wire signals from the aspirating probe were recorded on magnetic tape using the same techniques discussed previously.

4.8 Mass Flow Rate Measurements in Heterogeneous Flows

The natural oscillation frequencies and required sound forcing amplitudes were determined using procedures discussed in sections 4.4 and 4.5.

Known voltages were recorded to calibrate the channels used for hot wire signals. The hot wires were then calibrated in both gases using four flow rates with each gas (cf. Sec. 3.1). Prior to the calibration runs, the entire facility was evacuated and both the settling chamber and the tank were filled with the calibration gas. Calibrations were assumed valid for only one hour, after which a new calibration was accomplished.

Prior to each run, the system was evacuated and refilled with the two Freons. Although the density measurements indicated that little reservoir contamination resulted from a single run, it was felt that the settling chamber might be contaminated during the stopping process. The consequent increase in starting time for a subsequent run, caused by the need to purge the contaminated gas, would have been unacceptable for the mass flow measurements since the planned half second of data was just adequate for later

data processing.

The jet facility and recorder were operated using the same techniques described previously. A summary of the procedures is given in table 4.

Measurements were taken at 12 stations with Freon 114 flowing into Freon 22 and at 15 stations with the gases reversed. The facility was inverted for runs with Freon 22 flowing, as discussed previously.

Usually, 36 measurements, spaced .1 mm apart, were made across the shear layer at each station. A few overlapping readings were taken to check the accuracy and repeatability. At the most downstream stations, 45 readings were needed to cover the wider mixing region.

V. DATA PROCESSING

5.1 Mean Density Measurements

Recorded signals from the density sensitive aspirating probe were played back at 60 inches per second (i.e., half the recording speed) into a Hewlett Packard 3450A Multi-function Meter. The meter was adjusted to provide ten voltage readings per second, accurate to .0001 volts. The BCD output of the meter was connected to a Hewlett Packard 5050B Digital Recorder which printed the voltage readings on a paper strip.

The "data-ready" signal (i.e., the recorded step signal from the time delay circuit set to indicate the beginning of usable data) was played back into an oscilloscope. The printer was started manually when the step signal changed value.

Ten readings, representing half a second of data, were averaged to give the final value. Variations over the interval rarely exceeded $\pm$ .001 volts which was within the accuracy of the recorder and the hot wire equipment used with the aspirating probe.

The averaged values from readings taken in the pure tank gas and in the core of the jet were used to determine the maximum voltage variation. Other readings were then converted to a percentage of the maximum. This permitted the use of a single calibration curve when the voltages

were converted to densities. Several calibrations showed that, although the absolute value of the voltages and the maximum variation changed slightly over a period of time, the scaled values would always yield the same density measurement, within the accuracy of the probe.

5.2 Analysis of Mass Flow Rate Fluctuations

Digital data processing techniques were used to obtain a detailed analysis of the shear layer oscillations from the limited amount of available data. To adequately represent the higher harmonics of the oscillations, a relatively high sampling rate was required with the consequent need for sophisticated data handling equipment.

The recorded hot wire and audio oscillator signals were played back at 60 inches per second into a data acquisition system. Amplifiers scaled the four inputs to fill the range of an analog-to-digital converter. The inputs were sampled simultaneously, 5000 times a second, to yield a real-time digitizing rate of 10,000 samples per second on each channel. The samples were then multiplexed, converted into an eleven bit binary number and transmitted, along with a binary channel identifier, into the core of an IBM 360-44 computer.

The "data-ready" signal was used to trigger the digitizing equipment. Sampling was stopped automatically by the computer after 5,120 samples had been taken from

each of the four channels. The samples represented just over half a second of data. The computer formatted the information into five records of 4096 samples each (1024 per channel) and wrote it on a disk pack. The process was repeated for each experimental run. About half of a set of profiles could be digitized at a time, covering roughly 300 runs and generating over six million numbers.

Because the 360-44 was not available for processing, a link was made to a 360-75 computer and the information was transmitted to the core of the 75 and then written out on digital magnetic tape. The tape was then used as the data source for the rest of the processing.

The digitized voltages were averaged, record by record, and checked for obvious errors. The averaged values corresponding to the recorded calibration voltages were used to calibrate the entire data acquisition process including the biasing circuits, record and play-back amplifiers, scaling amplifiers for the digitizing, and the analog-to-digital converter, and thus convert the digitized values directly back into the source voltages.

Hot wire calibration voltages were plotted against the appropriate mass flow rates. For the homogeneous runs, a calibration line was obtained immediately from a least-squares fit. However, calibration points for the heterogeneous experiments yielded only a "calibration band" lying between the Freon 22 and Freon 114 calibration lines.

A particular calibration line within the band was chosen to make the segments of the mean mass flow rate profiles measured by the different hot wires fit together smoothly. Readings made in the jet core were assumed to lie on the pure jet gas line and readings falling in the lowest speed portion of the shear layer were placed near the reservoir gas line. Overlapping readings (i.e., readings taken by two wires at the same point) were made to correspond to the same mass flow rates. Although the process made the mass flow rate profiles smooth, it did not necessarily improve the accuracy since nothing was known about the location of calibration lines for gas mixtures. Therefore, the accuracies discussed in section 3.1 are still applicable.

The hot wire calibration lines were used to compute mass flow rates from each of the digitized voltages, producing 5,120 measurements for each data point.

The oscillation parameters to be evaluated included the amplitude and phase of the forcing frequency and its sub- and first ultra-harmonic. Ordinarily, a spectral analysis would have been used but the processing cost for the number of points involved would have been excessive. Therefore, a discrete Fourier transform was used. The program used requires an input of 2^m values representing equally spaced measurements of a varying quantity. The output consists of the amplitudes of the sine and cosine

components of $2^{m-1}-1$ harmonics. The sum of the harmonics provides an approximation to the input signal:

$$f(t) \simeq \frac{a_o}{2} + \sum_{k=1}^{N-1} \left(a_k \cos \frac{k\pi t}{\tau} + b_k \sin \frac{k\pi t}{\tau} \right) + \frac{a_N}{2}$$

$$N = 2^{m-1}$$

The period of the transform fundamental is given by:

$$\tau = 2^m \times 10^{-4} \text{ sec}$$

for a real-time digitizing rate of 10,000 samples per second.

As a compromise between economy and accuracy, "m" was chosen to be ten, giving an input of 1024 samples. The output then provided 511 harmonics of the transform fundamental frequency, 9.76 Hz. Ordinarily, this "bandwidth" would not have provided a sufficiently accurate evaluation of the oscillation characteristics. Therefore, the sound forcing frequency was set at some multiple of 19.52 Hz to make the frequency of the desired outputs, including the sub-harmonic, coincide with the frequencies of harmonics generated by the Fourier transform. Harmonic amplitudes were computed from the sine and cosine components:

$$h_k = \sqrt{a_k^2 + b_k^2}$$

The phase angle was computed for the transform harmonic corresponding to the forcing frequency. Since the audio oscillator and hot wire signals had been sampled simultaneously during the digitizing, the samples had the same phase relationship as the original signals. Therefore, the oscillator samples were analyzed using the same Fourier transform to generate a reference phase angle, $\hat{\phi}$, where:

$$\hat{\phi} = \tan^{-1} \frac{\hat{b}_k}{\hat{a}_k}$$

$\hat{a}_k$, $\hat{b}_k$ = cosine, sine components of forcing frequency harmonic

The hot wire phase angle was then computed from:

$$\phi = \tan^{-1} \frac{b_k}{a_k} - \hat{\phi}$$

Each of the five records comprising one data point was analyzed and the resulting amplitudes and phase angles were averaged to give the final values.

In all, over thirty million digitized samples were analyzed. The results are presented in the next section.

VI. RESULTS

6.1 Homogeneous Flow

During the past decade, the theoretical analysis of free shear layer instability has been greatly refined and the results have been brought into close agreement with experimental observations. The progress has been due to the use of more realistic flow models and the calculation of more significant instability parameters. Specifically, flow models have been generalized to include the effects of viscosity, finite amplitude disturbances and non-parallel flow, and spatially rather than temporally amplifying waves. The calculations have provided growth rates as a function of disturbance frequency, wave speeds, eigen-function shapes and other physically measurable quantities.

The results presented by Michalke (Ref. 15) are a particularly good example of the sophisticated analysis now possible. Michalke integrated the Rayleigh equation:

$$(\bar{u} - \frac{\omega}{\alpha})(\phi'' - \alpha^2\phi) - \bar{u}''\phi = 0$$

with the stream function defined as:

$$\psi(x, y, t) = \phi(y)\, e^{i(\alpha x - \omega t)}$$

and with the boundary conditions:

$$\phi(-\infty) = \phi(\infty) = 0$$

A hyperbolic tangent velocity profile was used:

$$\bar{u}(y) = \frac{1 + \tanh y}{2}$$

and spatially amplifying waves were assumed (i.e., α complex). Freymuth (Ref. 1) used the results as a basis for comparison with his experimental values and, in the process, justified most of the assumptions inherent in the model. The measured mean velocity profiles were close to the hyperbolic tangent model and the instability parameters were found to be independent of the Reynolds number for $Re_\theta > 61$, thus justifying the use of the Rayleigh equation. The small differences between experimental and theoretically predicted eigenvalues and eigenfunctions were due to the finite amplitude of the actual flow oscillations and the changes in the velocity profile between the nozzle exit and stations further downstream. Additional theoretical work by Michalke (Ref. 16) clarified even these minor disagreements and the shear layer instability problem can now be considered largely solved for the case of homogeneous flow.

With this firm basis for comparison, experiments were conducted using Freon 22 as both the jet and reservoir gas to validate the experimental and data processing procedures. Since short-duration, quasi-steady experiments and digital data acquisition and processing were not the techniques usually employed for hydrodynamic stability experiments,

some type of comparative analysis was needed to verify their applicability.

The experiments were conducted using procedures identical to those employed in the later heterogeneous tests. Of particular importance was the use of the same small segment of data occurring between .8 and 1.4 seconds after the flow was started. The same digital data processing procedures were used and the flow conditions (i.e., Reynolds number, tank pressure) were set equal to those used in the heterogeneous tests. A summary of the flow conditions is given in table 5.

The sound forcing amplitude and frequency were determined using procedures described in section 4.5.

Hot wire velocity measurements were made across the shear layer at four downstream locations, all within the region of exponential disturbance oscillation growth. Mean velocity profiles were prepared and momentum thicknesses were computed. Figure 15 compares the non-dimensionalized profiles with the hyperbolic tangent profile used for theoretical analyses. The profiles have been scaled to coincide in slope and position at the point where $\bar{u}/U = .5$. The relaxation from a wall-type boundary layer at the nozzle exit to the shear layer profile downstream is evident. At the most downstream station, the profile has a second inflection point in the low speed region. This was noted by Browand (Ref. 12) who associated with it the

appearance of high frequency flow fluctuations and the development of small scale turbulence.

A reference length was needed to scale the oscillation parameters for comparison with theoretical values. Although the momentum thickness can be computed readily for any profile, the selection of a particular value to represent the entire flow is somewhat arbitrary. The theoretical model assumes that the flow is parallel and that the momentum thickness is constant. This is not true in the experimental situation. A significant downstream increase in momentum thickness has been observed by Sato (Ref. 17), Browand, and in the present experiments. An increase takes place just downstream from the nozzle exit as the wall boundary layer relaxes into the shear layer profile. The developed profile then grows according to the laminar similarity law (i.e., $\theta \sim x^{\frac{1}{2}}$) until the transition to turbulence begins. The growth rate then increases as secondary inflection points broaden the low speed portion of the profile. Eventually the growth becomes linear, as predicted by the turbulent similarity rules. Selecting a particular reference thickness is equivalent to identifying the downstream station that determines the stability characteristics of the flow. It seems evident that the reference must lie in the region of the developed laminar shear layer, downstream of the transition from the nozzle wall profile but before the development of

secondary inflection points. Browand chose such a reference, lying about two-thirds of the distance between the separation point and the start of the transition to turbulence. Freymuth, rather surprisingly, found that the momentum thickness remained nearly constant after an initial twenty percent increase just downstream from the nozzle exit. He selected a reference profile at $x = 10\ \theta_o$, where θ_o is the momentum thickness at the separation point. Since the thickness increased only another three percent between the reference point and $x = 40\ \theta_o$, his reference selection was not at all critical.

The present velocity profiles indicated that a reference station should be chosen between $x = 4$ mm and $x = 7$ mm with a corresponding thickness between .235 mm and .283 mm. A value of .25 mm was chosen to match Browand's reference as closely as possible. Some comparative values are given in table 6.

The natural oscillation frequency was determined to be about 192 Hz, giving a Strouhal number of .09. This compares closely with values reported by Sato (.10) and Browand (.092). Although Freymuth does not mention a natural frequency, he shows that a nearly constant maximum amplification rate is attained at Strouhal numbers lying between .068 and .136. One would expect the naturally occurring frequency to lie in this range. Michalke (Ref. 2) reports a natural frequency non-dimensionalized in terms of

δ_o^*, the displacement thickness at the separation point. The present results give $f\delta_o^*/U = .0235$, very close to Michalke's value, .023.

The sound forcing frequency was set at 195.2 Hz, corresponding to the twentieth harmonic of the discrete Fourier transform used for processing. The forcing amplitude was set at 73 db (cf. Sec. 4.5).

A Fourier analysis of the velocity fluctuations was made at each point of the four profiles. Plots of the amplitude of the forcing frequency harmonic are shown in figure 16. The expected bimodal distribution across the shear layer and the increase in the amplitude downstream are evident. The plot of the amplitudes at the lower and upper peaks, $\hat{c}_1$ and $\hat{c}_2$ respectively, shows that the amplification was exponential in the region surveyed. The growth rate was calculated from the slope of the peak amplitude lines using the formula:

$$-\alpha_i = \frac{\theta_{ref}}{x^2 - x^1} \ln \frac{\hat{c}^2}{\hat{c}^1}$$

where the superscripts refer to the two stations used. The resulting values were .12 for $\hat{c}_1$ and .081 for $\hat{c}_2$. These compare reasonably well with Freymuth's value of about .09 for $\hat{c}_1$ growth and values of .088, .09 and .11 for $\hat{c}_2$ growth reported by Freymuth, Sato and Browand respectively. Theoretically, of course, the two peaks should grow at

the same rate since the eigenfunction shape does not change with downstream position. The experimental flow is not strictly parallel, however, and some downstream change can be expected. With only four profiles, it is impossible to determine whether the different growth rates for $\hat{c}_1$ and $\hat{c}_2$ are due to experimental scatter or an actual downstream development of the amplitude distribution profile.

A comparison of the fluctuation amplitude distribution to experimental and theoretical results reported by Freymuth is given in figure 17. The experimental values were scaled to make the peak amplitudes match. The agreement is quite satisfactory and gratifying in light of the great differences in the experimental procedures used by Freymuth and the author.

Phase angles for the forcing frequency harmonic were calculated for the readings taken at x = 4, 7, and 10 mm and are shown in figure 18. The phase distribution across the shear layer is seen to agree qualitatively with an unscaled plot given by Freymuth. In particular, a large change in phase is seen to occur in the low speed portion of the profile. This phase shift corresponds to the minimum in the fluctuation amplitude, as seen in figure 19.

The wavelength of the oscillation was computed from the downstream increase in phase angle. The phase angle profiles were scaled with the momentum thickness and adjusted to make the large phase change occur at the same

y/θ value. The phase change between the profiles was then measured at several points and the readings were averaged to give a final value, $\lambda = .9$ mm. The corresponding wave number was calculated as:

$$\alpha_r = \frac{2 \pi \theta_{ref}}{\lambda} = .174$$

Freymuth reported a value of .162 at the corresponding Strouhal number and Browand gave a value of .18.

A summary of the eigenvalues computed from the present results and comparative values from previous work is presented in table 7. The agreement was considered entirely satisfactory and adequate to justify the use of the experimental procedures in heterogeneous experiments.

6.2 Heterogeneous Flow

6.2.1 Theoretical Analysis

The hydrodynamic stability equation for a two-dimensional, incompressible, boundary layer flow in a non-uniform medium is derived in the appendix. The development follows one given by Baker, Rozenman and Weinstein (Ref. 18) and includes the effects of viscosity and buoyancy but neglects molecular diffusion. The resulting non-dimensionalized equation is:

$$\left(\bar{u} - \frac{\omega}{\alpha}\right)\left(\phi'' - \alpha^2\phi\right) - \bar{u}''\,\phi + \frac{\bar{\rho}'}{\bar{\rho}}\,\frac{\delta}{\epsilon}\left[\left(\bar{u} - \frac{\omega}{\alpha}\right)\phi' - \bar{u}'\phi\right]$$

$$= \frac{1}{Re_\delta}\,\frac{1}{i\alpha}\left(\phi^{iv} - 2\,\alpha^2\phi'' + \alpha^4\,\phi\right)$$

$$+ \frac{1}{Fr_x}\left\{\frac{\delta}{\epsilon}\,\frac{\bar{\rho}'}{\bar{\rho}}\,\frac{1}{i\alpha}\left[\frac{\phi'}{\bar{u} - \frac{\omega}{\alpha}} + \frac{\bar{u}'\phi}{\left(\bar{u} - \frac{\omega}{\alpha}\right)^2}\right] + \left(\frac{\delta}{\epsilon}\right)^2\,\frac{\bar{\rho}''}{\bar{\rho}}\,\frac{1}{i\alpha}\,\frac{\phi}{\bar{u} - \frac{\omega}{\alpha}}\right\}$$

$$- \frac{1}{Fr_y}\,\frac{\delta}{\epsilon}\,\frac{\bar{\rho}'}{\bar{\rho}}\,\frac{\phi}{\bar{u} - \frac{\omega}{\alpha}}$$

where:

$$Re_\delta = \frac{\bar{\rho}\,U\,\delta}{\mu}$$

$$Fr_x = \frac{U^2}{g_x\delta} \quad ; \quad Fr_y = \frac{U^2}{g_y\delta}$$

and g_x and g_y refer to the x and y components of the gravity vector.

Since the Reynolds number in the present experiments was greater than one hundred, the terms representing viscous forces are small enough to be neglected.

The scale lengths for the velocity and density profiles, δ and ϵ respectively, are approximately equal. Thus, the term representing the inertial forces produced by the density gradient is of first order and must be retained. However, the buoyancy forces produced by the density heterogeneity can be neglected because the Froude number in the experiments was large. Note that both the x and y components of the buoyancy force are scaled with the Froude number and the flow direction is, therefore, not significant in determining the relative magnitude of the forces. In the present experiments, the flow was vertical, corresponding to forces in the x-direction.

With the above simplifications, the stability equation reduces to:

$$\left(\bar{u} - \frac{w}{\alpha}\right)\left(\phi'' - \alpha^2\phi\right) - \bar{u}''\,\phi$$

$$+ \frac{\bar{\rho}'}{\bar{\rho}}\frac{\delta}{\epsilon}\left[\left(\bar{u} - \frac{w}{\alpha}\right)\phi' - \bar{u}'\,\phi\right] = 0$$

with

$$\phi(-\infty) = \phi(\infty) = 0 \ .$$

Maslowe (Ref. 7) integrated this equation using the Holmboe flow model for the mean velocity and density variations:

$$\bar{u} = \frac{1 + \tanh y}{2}$$

$$\bar{\rho} = \rho_o \exp(-\beta \tanh y)$$

Although Maslowe calculated the stability characteristics of both temporally and spatially amplifying waves, only the latter are relevant to the experimental situation. Thus, the appropriate form for the stream function is:

$$\psi(x, y, t) = \phi(y)\, e^{i(\alpha x - \omega t)}$$

where α is complex and ω is real.

The calculated eigenvalues are shown graphically in figure 20. As β increases (i.e., the flowing gas becomes lighter), the maximum disturbance amplification rate is seen to increase until it reaches an absolute maximum at $\beta = 1.7$, corresponding to a density ratio of about 30. The wave number along the maximum amplification contour decreases until $\beta \simeq .8$, after which it increases. Opposite trends are predicted when a heavy gas flows into a lighter one (i.e., $\beta < 0$). These predictions agree qualitatively with the flow characteristics observed in the spark shadowgraphs, as discussed in section 4.1.

The density ratio of the Freons used in the present experiments was 1.98, corresponding to $\beta = \pm .34$ for the two flow cases. Programs prepared by Maslowe were used to compute the eigenvalues and eigenfunctions at the points of

maximum disturbance amplification. Experimental results will be compared with these computed values in the later parts of this section.

6.2.2 Mean Profiles

Average mass flow rates were computed from the digitized hot wire signals. Profiles were then plotted for each downstream station. The profiles showed that the flow region covered by the experiments could be divided into three parts. First, a transformation from the nozzle wall boundary layer to the shear layer profile takes place in the first few millimeters downstream from the nozzle exit. Profiles taken near the nozzle exit with Freon 22 flowing into Freon 114 are shown in figure 21. The transformation is evident as the sharp corner in the low speed region relaxes into the more usual shear layer profile shape.

Downstream from the transformation region, the profile shapes remained similar for some distance. The stability characteristics of this laminar similarity region were the primary concern of the present investigation. Figures 22 and 23 compare the profiles with the mass flow rate profile given by the Holmboe model:

$$\frac{\overline{\rho u}}{\rho_\infty U} = \frac{\exp(-\beta \tanh y/\tilde{\theta})}{e^{-\beta}} \frac{1 + \tanh y/\tilde{\theta}}{2}$$

The profile width used for scaling both the experimental and theoretical results was computed using only the mass

flow rate values:

$$\tilde{\theta} = \int_{-\infty}^{\infty} \frac{\overline{\rho u}}{\rho_\infty U} \left(1 - \frac{\overline{\rho u}}{\rho_\infty U}\right) dy$$

This length was used in place of the more common momentum thickness because velocity values could not be determined with sufficient accuracy from the mass flow rate and density measurements. The scaled profiles were made to coincide at $\overline{\rho u}/\rho_\infty U = .5e^{\beta}$.

Mean density profiles were plotted for stations lying within the laminar similarity region. The mass flow rate thickness parameter and the adjusted origin used to scale and compare the mass flow rate profiles were used to scale the density profiles for comparison with the Holmboe model. The results for the two flow cases are shown in figures 24 and 25. In each case, the scaled density profile was considerably thinner than the model. Further, the mass flow rate scaling did not generate similar density profiles. Both the thickness and position of the scaled density profiles varied with downstream location. Thus, the region was not one of true similarity since the ratios of the scale lengths needed to collapse profiles of the several flow parameters (i.e., velocity, density, mass flow rate) to a single curve were not the same at each station. This is not of great importance to the hydrodynamic stability analysis as long as the gradients in the streamwise direction are small

enough to make the parallel flow assumption reasonable.

Disagreement with the Holmboe model was not too surprising since the model does not represent a theoretical solution to the steady laminar flow problem. However, the model does seem reasonable. The profile shapes have the desired asymptotic approach to free stream and reservoir values and the widths of the velocity and density profiles are about equal. Since the Schmidt number is about one for most gases, with $Sc = \nu/\mathcal{D}$, the spreading rate for equivalent velocity and density gradients should be roughly the same. Thus, one would expect experimental velocity and density profiles to have about the same thickness. The disagreement in the present circumstances arises from the conditions at the nozzle exit. The velocity profile just downstream from the nozzle exit has a relatively large thickness, somewhat greater than the thickness of the wall boundary layer inside the nozzle. However, the density profile at the separation point has essentially zero thickness and its maximum gradient lies near $y = 0$, in the low speed portion of the velocity profile. Although the density profile spreads more rapidly than the velocity profile because of the higher relative gradient, its thickness does not reach that called for by the Holmboe model within the region of mass flow rate similarity. The problem is most acute when Freon 22 flows into Freon 114 because the similarity region is shorter. In the opposite flow case, the Holmboe model is

approached at the most downstream portion of the region. The transformation from the nozzle exit profiles to the profiles at or near the end of the similarity region is shown in figure 26. Since the shear layer at some point in this region determines the instability characteristics, one would expect closer agreement with theoretical predictions for the case where Freon 114 flows into Freon 22. In either case, the higher gradients resulting from the thin density profiles should exaggerate the effects of the heterogeneity. Later results will show this to be true.

Downstream from the similarity region, the profiles show the beginning of the transition to turbulence. Secondary inflection points in the low speed part of the shear layer, similar to those observed in the homogeneous flow results, can be seen in figures 27 and 28. An increase in the spreading rate is also evident. Hot wire measurements were not continued downstream beyond this early transition region.

The growth of the shear layer thickness is shown in figure 29. As in the homogeneous flow results, an increase in the growth rate occurs at some downstream location, marking the beginning of the transition to turbulence. The increase is more noticeable when the thickness is plotted against $x/\tilde{\theta}$. A reference thickness was selected at a point about two thirds of the distance from the nozzle exit to the beginning of transition, corresponding to the reference

used in the homogeneous flow analysis. This reference mass flow rate thickness was used to scale the eigenvalues for comparison with the theoretical predictions. The theoretical values were scaled using the mass flow rate thickness for the appropriate Holmboe flow model. A summary of the flow conditions, reference lengths, and non-dimensional flow parameters is given in table 8.

6.2.3 Analysis of Flow Fluctuations

The frequency of the naturally occurring flow oscillations was measured for the two flow cases. With Freon 22 flowing into Freon 114, the natural frequency was about 151 Hz, giving a Strouhal number of .0697, where $S = \omega = 2\pi f \tilde{\theta}_{ref}/U$. The theoretically predicted frequency at the maximum amplification point was .0761. With Freon 114 flowing into Freon 22, the natural frequency varied between 90 Hz and 117 Hz, giving Strouhal numbers from .112 to .147. The theoretically predicted value was .129, about midway between the measurements. The agreement between the experimental and theoretical results compares favorably with that obtained in the homogeneous flow case.

Profiles showing the amplitude distribution of the flow oscillation at the frequency of the sound forcing were prepared for each downstream station. The anticipated bimodal distribution was attained a short distance

downstream from the nozzle exit, as shown in figure 30.* Figures 31, 32, and 33 show the distribution in the similarity region. Here, the shape of the distribution remains relatively unchanged but the amplitude increases at each station. The amplitude of the peaks, evaluated as the average of the three largest point values, is plotted in figure 34 and the growth is seen to be exponential in the similarity region. As in the homogeneous flow discussion, the growth rate was calculated using the relationship:

$$-\alpha_i = \frac{\theta_{ref}}{x^2 - x^1} \ln \frac{\hat{c}^2}{\hat{c}^1}$$

With Freon 22 flowing into Freon 114, the resulting value was .148 compared to .076 in the opposite flow case. The significantly greater amplification rate attained with the light gas flowing into a heavier one verifies the qualitative conclusions reached from the analysis of the spark shadowgraphs and agrees with the trend predicted by Maslowe. Eigenvalues computed with his programs give a maximum amplification rate of .130 and .0904 for the two flow cases. In each case, the experimental results exaggerate the predicted effects of the density heterogeneity. However,

* Lines connecting data points in amplitude and phase plots are drawn solely to clarify the presentation. The detailed shape of the curve is not significant.

all homogeneous flow results have indicated that the experimental amplification rates are lower than the theoretical predictions. In the present homogeneous flow experiments, the theoretical value was .10 and the theoretical result was .114. This indicates that the slightly lower than theoretical amplification rate measured with Freon 114 flowing into Freon 22 is an expected result. However, the excessive amplification rate observed in the opposite flow situation is most unusual and demonstrates the effect of the thin density profiles and the consequent high density gradients.

The shape of the amplitude distribution profiles is markedly different in the two flow cases. With Freon 22 flowing into Freon 114, the amplitude at the peaks is nearly equal ($\hat{c}_1/\hat{c}_2 = .88$) whereas in the opposite flow situation the upper peak is far larger ($\hat{c}_1/\hat{c}_2 = .148$). Theoretical distribution shapes were prepared from the eigenfunctions calculated with Maslowe's programs. The evaluations were made using eigenvalues corresponding to the point of maximum amplification rate. The relationship for the mass flow rate fluctuation amplitude was derived from:

$$\rho u = \overline{\rho u} + (\rho u)' = (\bar{\rho} + \rho')(\bar{u} + u') \doteq \bar{\rho}\bar{u} + \bar{\rho}u' + \bar{u}\rho'$$

or:

$$(\rho u)' = \bar{\rho}\bar{u} - \overline{\rho u} + \bar{\rho}u' + \bar{u}\rho' \quad .$$

By observing that:

$$\overline{\rho u} = \overline{\bar{\rho}\bar{u}} + \overline{\bar{\rho}u'} + \overline{\bar{u}\rho'} + \overline{\rho'u'}$$

$$= \bar{\rho}\bar{u} + \overline{\rho'u'} \doteq \bar{\rho}\bar{u}$$

we obtain:

$$(\rho u)' \doteq \bar{\rho}u' + \bar{u}\,\rho' \quad .$$

In terms of the eigenfunction, $\phi(y)$:

$$(\rho u)' = \left\{\bar{\rho}\,\phi' + \bar{u}\,\phi\,\frac{\alpha}{\alpha\bar{u} - \omega}\,\frac{d\bar{\rho}}{dy}\right\} e^{i(\alpha x - \omega t)}$$

and:

$$|(\rho u)'| = \text{Mod}\left\{\bar{\rho}\,\phi' + \bar{u}\,\phi\,\frac{\alpha}{\alpha\bar{u} - \omega}\,\frac{d\bar{\rho}}{dy}\right\} e^{\alpha_i x}$$

where the mean values are determined from the Holmboe model and the absolute value is computed as the modulus of the complex eigenfunction representation. Theoretical and experimental profiles are compared in figures 35, 36, and 37. Although the experimental values are too irregular to allow a detailed comparison, the relative amplitude of the peaks and their spacing in the scaled coordinates seem to follow the theoretically predicted trends. The homogeneous flow distribution is included for comparison in figure 37. In both the theoretical and experimental results, its shape appears to lie between the two heterogeneous cases. In particular, the amplitude of the lower peak increases

steadily as β goes from negative to positive.

A third peak was observed in the high speed portion of the shear layer at the more downstream stations. A similar peak was observed by Freymuth (Ref. 1) in homogeneous flow. He found that its amplitude increased with the Strouhal number and concluded that the deviations from the theoretical distribution shape were due to the nonlinear effects of the finite fluctuation amplitudes.

The phase of the forcing frequency flow oscillation was evaluated at each data point and the distribution across the shear layer was plotted for the various downstream stations. Figures 38 and 39 show the phase distributions for the two flow cases at stations within the similarity region. Phase measurements were unreliable at the most upstream stations because the fluctuation amplitudes were too low. The problem was more severe with Freon 114 flowing into Freon 22.

With Freon 22 flowing into Freon 114, a large phase shift was observed at each station near the point where the oscillation amplitude was a minimum. The wavelength was calculated by scaling the profiles with the mass flow rate thickness and then measuring the phase change between the profiles. The resulting value was .82 cm, giving a wave number of .190 where:

$$\alpha_r = \frac{2\pi\,\tilde{\theta}_{ref}}{\lambda}$$

This is close to the theoretical value, .183.

In the opposite flow case, the wavelength was .864 cm, giving a wave number of .218, very close to the theoretical value, .214.

A comparison of all theoretical and experimental eigenvalues is given in table 9.

At stations downstream from the similarity region, the amplitude of flow oscillations at frequencies other than the forcing frequency becomes significant and changes in the distribution of the forcing frequency amplitude and phase are apparent. The growth of the harmonic frequency oscillations indicates the beginning of the transition to turbulence and occurs concurrently with changes in the shape of the mean mass flow rate profiles and the rate of increase of the profile thickness.

The character of the increase in harmonic fluctuations is markedly different in the two flow cases. With Freon 22 flowing into Freon 114, the first harmonic (i.e., twice the forcing frequency) is most significant. Figures 40 through 45 show the increasing amplitude of these fluctuations and the consequent changes in the forcing frequency oscillations. A decrease in the amplitude of the forcing frequency component occurs in the portion of the shear layer where the first harmonic oscillations reach a maximum. This change in the relative amplitudes of the components continues downstream to the extent of the measurements.

The phase of the forcing frequency oscillations becomes rather indefinite in this region and the abrupt phase shift disappears, as does the sharp minimum in the amplitude distribution associated with it. Within the region covered by the measurements, the amplitudes of oscillations at frequencies other than the forcing frequency and the first harmonic did not increase to a significant extent.

With Freon 114 flowing into Freon 22, the sub-harmonic oscillations (i.e., at half the forcing frequency) are the dominant effect. Figures 46 through 48 show the increase in this component relative to the forcing frequency fluctuations. Other components have significantly lower amplitudes until the most downstream station is reached. Here, the amplitude of the first harmonic becomes nearly equal to the sub-harmonic. Unlike the previous flow case, all fluctuations reach a peak near the center of the shear layer. The bimodal character of the forcing frequency amplitude distribution is lost and the abrupt phase shift completely disappears. Further downstream, the phase distribution becomes very irregular.

The increase in the amplitude of harmonic components occurs in a region where the magnitude of the fluctuations is too large to be described by the linearized hydrodynamic stability theory. The very great differences between the two flow cases in this region are,therefore, due to non-linear effects which are not well understood. Although

Browand was able to provide some physical explanations for the appearance of harmonic oscillations, it is not at all clear why the density heterogeneity should cause so marked an alteration in their development.

VII. CONCLUSION

7.1 Analysis of Eigenvalues

The instability of the free shear layer is related to the instability of a vortex sheet, discussed by Helmholtz nearly a century ago. Any perturbations in the vortex sheet are unstable since they generate forces which tend to move the perturbation further from the initial vorticity plane. The mechanism can be readily understood if one thinks of the pressures induced on a wavy wall. If the disturbed vortex sheet is translated so that the flow velocity is equal and opposite on either side, the interface will appear as a wavy wall in a uniform flow:

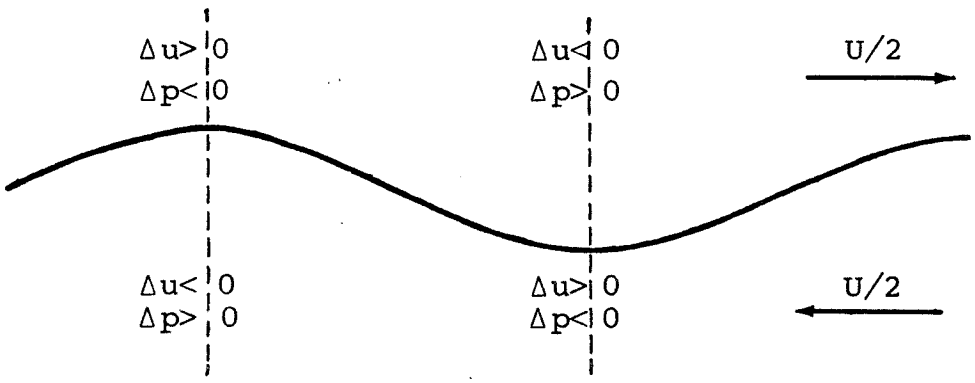

The resulting perturbations in velocity produce a pressure gradient which tends to amplify the disturbance.

When a shear layer of finite thickness is analyzed, the magnitude of the destabilizing forces depends upon the wavelength of the perturbation. For some particular wavelength, the pressure forces tending to amplify the

disturbance reach a maximum in relation to the inertial forces tending to retard the motion. This wavelength scales with the thickness of the shear layer and varies slightly with changes in the shape of the velocity profile. With a hyperbolic tangent profile and a homogeneous flow, the most unstable wavelength is about thirty times the momentum thickness.

If a shear layer is perturbed by noise having a uniform intensity over the range of unstable wavelengths, one would expect the most amplified wave eventually to dominate the shear layer oscillations. However, the amplification rate is fairly uniform around the most unstable point and the wavelength of the naturally occurring oscillations varies over a moderate range. The specific value measured will depend upon the content of the background noise at the time of measurement.

A density gradient across the shear layer produces only a moderate change in the most unstable wavelength. The density ratio of about two used in the present experiments reduced the wavelength to 28.8 times the reference thickness when the density gradient was positive (i.e., heavy gas flowing into light) and increased it to 33.0 times the reference thickness with the gradient negative. The theoretically predicted values were 29.3 and 34.3 times the reference thickness for the respective cases.

In a homogeneous flow, the most unstable wave

propagates in space at just over half the free stream velocity. The positive density gradient increased the wave speed to .56U while the negative gradient reduced it to about .38U. The corresponding theoretical values were .603U and .416U.

The most significant effect of the density gradient was a change in the rate of amplification. A cursory analysis of the problem might lead one to believe that any density gradient would lead to increased inertial forces from the additional transverse momentum transfer and, hence, to a reduced amplification rate. Such a conclusion can be reached if a vortex sheet with a density discontinuity across it is analyzed. Landau and Lifshitz (Ref. 19) performed such an analysis and found the temporal amplification rate to be:

$$-\omega_i = k\,U\,\frac{\sqrt{\rho_1/\rho_2}}{\rho_1/\rho_2 + 1} = k\,U\,\frac{\sqrt{\rho_2/\rho_1}}{\rho_2/\rho_1 + 1} \leq k\,U$$

where ρ_1 is the density of the moving gas and ρ_2 is the density of the reservoir gas. The amplification rate is ostensibly reduced by any density gradient and the magnitude of the reduction for a given density ratio is the same with either the heavy or light gas moving.

Maslowe's more sophisticated analysis of spatially amplifying oscillations, as well as the present experimental results, shows that these conclusions are not correct. With

the density gradient negative, a significant increase in the rate of amplification was observed in both the theoretical analysis and the experimental measurements. A decrease in the amplification rate was observed when the density gradient was positive. The qualitative disagreement with the elementary description demonstrates the complexity of the mechanical system. The pressure gradients responsible for the instability are somehow increased when the density gradient is negative. Since they follow from variations in dynamic pressure, one could conclude that the density fluctuations play a part in the changing amplification rates. For instance, if the density and velocity fluctuations are in phase with the density gradient negative and out of phase with the gradient positive, the appropriate changes in the pressure gradients will be produced. Obviously, this is a gross oversimplification, but it indicates that the relationship between the velocity and density fluctuations is as significant as their magnitudes.

In a homogeneous flow, the disturbance amplitude doubles in about a fifth of a wavelength. With the two-to-one density ratio, the amplitude doubled in only .142λ with the gradient negative and took .317λ with the gradient positive. Maslowe's theoretical analysis predicted doubling in .155λ and .262λ for the respective cases.

The reasonably close agreement between the measured and theoretical eigenvalues, despite differences in the mean profiles, indicates that the hydrodynamic stability analysis performed by Maslowe adequately describes the mechanics of the flow. Measurements of the density and velocity fluctuations, rather than the mass flow rate measurements used here, would provide a more discriminating comparison with the theoretical work and perhaps lead to a better physical understanding of the instability.

7.2 Analysis of the Eigenfunction Shapes

The density gradient produced a significant change in the fluctuation amplitude distribution, particularly in the relative magnitudes of the upper and lower peaks. This effect apparently follows from the use of mass flow rate measurements.

The theoretical distribution of velocity fluctuation amplitudes does not show a significant variation in the relative size of the peaks, and the changes that are predicted are opposite to those observed in the mass flow rate distributions (i.e., Maslowe gives $\hat{c}_1/\hat{c}_2 = .462$ with the gradient positive and .418 with the gradient negative). The observed peak amplitude relations are easily explained if we assume that the significant term in the mass flow rate fluctuation is $\bar{\rho}u'$. With the density gradient positive, $\bar{\rho}$ is greater in the upper portion of the shear

layer, producing a relative increase in the amplitude of the upper peak. With the gradient reversed, the upper peak is reduced. The second part of the mass flow rate fluctuation, $\bar{u}\rho'$, would differ in the two cases only as the density fluctuation distribution differed. Although no experimental measurements were made, the theoretical distributions are unimodal in both cases with the peak near the center of the shear layer. Thus, this term would not affect the shape of the mass flow rate fluctuation distribution.

7.3 Fluctuations in the Non-Linear Region

One of the most interesting observations of the experiments was the difference in the development of harmonic oscillations in the two flow cases.

As the fundamental frequency oscillations grow in amplitude, they produce strong concentrations of vorticity, spaced half a wavelength apart and moving at the wave speed. Eventually, these dominate the flow and a reasonable approximation to the flow can be made by considering a trail of alternating vortices. Browand (Ref. 12) showed that the interaction of the vortices could move them out of the center plane and thereby produce sub-harmonic oscillations. With the density gradient positive, such sub-harmonic oscillations developed in the center of the shear layer and increased in amplitude relative to the

fundamental at successive downstream locations. This pattern was observed by Sato (Ref. 11) and Browand in homogeneous flows and was the anticipated result.

A very different pattern was observed when the density gradient was negative. The first ultra-harmonic increased in amplitude near the center of the shear layer while the amplitude of the fundamental frequency oscillations decreased. Eventually, the first harmonic was the dominant fluctuation in the center of the layer and the distribution of the fundamental became bimodal with peaks on either side of the first harmonic peak. Such a pattern is observed in a Karman vortex street behind a bluff body. It is not clear how the initial row of vortices could divide and form two separate rows, displaced in the typical Karman trail configuration. It is also not known if this effect is another consequence of using mass flow rate measurements. Certainly, measurements of the velocity fluctuations would be helpful in clarifying the phenomenon.

7.4 Suggestions for Further Work

Although the mass flow rate measurements were helpful in establishing a relationship between theoretical and experimental results in the region of exponential growth, measurements of the fluctuating velocity and of the fluctuating density would be more satisfying. Such measurements could be made with a multi-sensor heat flux

probe if the size of the experiment were increased. An initial boundary layer thickness of at least a quarter inch would be necessary. Alternatively, velocity measurements could be made using some type of laser doppler system. Although some difficulties are being experienced in applying these systems to turbulent flows, the laminar unsteady flow of interest here might prove tractable.

Further theoretical work should be done to lend some insight into the vortex dynamics in the non-linear region. Additionally, the hydrodynamic stability analysis should be generalized to allow for differences in velocity and density scale lengths.

APPENDIX

DERIVATION OF THE HYDRODYNAMIC STABILITY EQUATION FOR HETEROGENEOUS FLOW

The equations of motion for an incompressible, two-dimensional flow in a non-uniform medium can be written as:

$$\rho\left(\frac{\partial u}{\partial t} + u\frac{\partial u}{\partial x} + v\frac{\partial u}{\partial y}\right) = -\frac{\partial p}{\partial x} + \frac{\partial}{\partial x}\left(\mu\frac{\partial u}{\partial x}\right) + \frac{\partial}{\partial y}\left(\mu\frac{\partial u}{\partial y}\right) + \rho g_x$$

$$\rho\left(\frac{\partial v}{\partial t} + u\frac{\partial v}{\partial x} + v\frac{\partial v}{\partial y}\right) = -\frac{\partial p}{\partial y} + \frac{\partial}{\partial x}\left(\mu\frac{\partial v}{\partial x}\right) + \frac{\partial}{\partial y}\left(\mu\frac{\partial v}{\partial y}\right) + \rho g_y$$

$$\frac{\partial \rho}{\partial t} + \frac{\partial(\rho u)}{\partial x} + \frac{\partial(\rho v)}{\partial y} = 0$$

where g_x and g_y refer to the gravity vector components in the x and y directions.

If molecular diffusion is neglected, the diffusion equation is simply:

$$\frac{\partial \rho}{\partial t} + u\frac{\partial \rho}{\partial x} + v\frac{\partial \rho}{\partial y} = 0$$

and the continuity equation can be reduced to:

$$\frac{\partial u}{\partial x} + \frac{\partial v}{\partial y} = 0$$

The stability analysis is conducted by analyzing the effect of small perturbations on a mean flow. For a boundary layer flow, we set:

$$u = \bar{u}(y) + u'$$

$$v = v'$$

$$p = \bar{p}(y) + p'$$

$$\rho = \bar{\rho}(y) + \rho'$$

Perturbations in viscosity will be considered negligible. The gases used in the present experiments had nearly equal viscosities, and, since all viscous effects will be shown to be small, neglecting effects due to viscosity fluctuations seems entirely reasonable.

The perturbation quantities are substituted and quadratic perturbation terms are dropped. The mean flow is assumed to satisfy the equations of motion:

$$0 = -\frac{\partial \bar{p}}{\partial x} + \bar{\rho}\, g_x + \mu \frac{d^2\bar{u}}{dy^2}$$

$$0 = -\frac{\partial \bar{p}}{\partial x} + \bar{\rho}\, g_y$$

These are subtracted from the linearized equations to yield:

$$\bar{\rho}\left(\frac{\partial u'}{\partial t} + \bar{u}\frac{\partial u'}{\partial x} + v'\frac{\partial \bar{u}}{\partial y}\right) = -\frac{\partial p'}{\partial x} + \mu\left(\frac{\partial^2 u'}{\partial x^2} + \frac{\partial^2 u'}{\partial y^2}\right) + \rho' g_x$$

$$\rho\left(\frac{\partial v'}{\partial t} + \bar{u}\frac{\partial v'}{\partial x}\right) = -\frac{\partial p'}{\partial y} + \mu\left(\frac{\partial^2 v'}{\partial x^2} + \frac{\partial^2 v'}{\partial y^2}\right) + \rho' g_y$$

$$\frac{\partial \rho'}{\partial t} + \bar{u}\frac{\partial \rho'}{\partial x} + v'\frac{\partial \bar{\rho}}{\partial y} = 0$$

$$\frac{\partial u'}{\partial x} + \frac{\partial v'}{\partial y} = 0$$

The pressure is then eliminated by differentiating the x and y momentum equations with respect to y and x and then subtracting one from the other. The equation of motion then becomes:

$$\frac{d\bar{\rho}}{dy}\left(\frac{\partial u'}{\partial t} + \bar{u}\,\frac{\partial u'}{\partial x} + v'\,\frac{d\bar{u}}{dy}\right) + \bar{\rho}\left[\frac{\partial^2 u'}{\partial t \partial y} - \frac{\partial^2 v'}{\partial t \partial x} + \bar{u}\,\frac{\partial^2 u'}{\partial x \partial y}\right.$$

$$\left. + \frac{d\bar{u}}{dy}\left(\frac{\partial u'}{\partial x} + \frac{\partial v'}{\partial y}\right) + \frac{d^2\bar{u}}{dy^2}\,v' - \bar{u}\,\frac{\partial^2 v'}{\partial x^2}\right]$$

$$= \mu\left(\frac{\partial^3 u'}{\partial x^2 \partial y} + \frac{\partial^3 u'}{\partial y^3} - \frac{\partial^3 v'}{\partial x^3} - \frac{\partial^3 v'}{\partial x \partial y^2}\right) + \frac{\partial \rho'}{\partial y}\,g_x - \frac{\partial \rho'}{\partial x}\,g_y$$

A stream function is used to satisfy the continuity equation and a Fourier decomposition is assumed in the x and t dimensions:

$$u' = \frac{\partial \psi}{\partial y} \quad ; \quad v' = -\frac{\partial \psi}{\partial x}$$

$$\psi(x, y, t) = \phi(y)\, e^{i(\alpha x - \omega t)}$$

Substitution yields:

$$\frac{d\bar{\rho}}{dy}\left(-i\,\omega\,\frac{d\phi}{dy} + i\,\alpha\,\bar{u}\,\frac{d\phi}{dy} - i\,\alpha\,\frac{d\bar{u}}{dy}\,\phi\right)$$

$$+ \bar{\rho}\left(-i\,\omega\,\frac{d^2\phi}{dy^2} + i\,\alpha\,\bar{u}\,\frac{d^2\phi}{dy^2} - i\,\alpha\,\frac{d^2\bar{u}}{dy^2}\,\phi + i\,\omega\,\alpha^2\phi - i\,\alpha^3\bar{u}\,\phi\right)$$

$$= \mu\left(\frac{d^4\phi}{dy^4} - 2\,\alpha^2\,\frac{d^2\phi}{dy^2} + \alpha^4\phi\right) + \frac{1}{e^{i(\alpha x - \omega t)}}\left(\frac{\partial \rho'}{\partial y}\,g_x - \frac{\partial \rho'}{\partial x}\,g_y\right)$$

The diffusion equation is used to eliminate the

density perturbation. A similar Fourier decomposition is assumed:

$$\rho' = R(y)\ e^{i(\alpha x - \omega t)}$$

and the diffusion equation then gives:

$$R(y) = \phi(y)\ \frac{\alpha}{\alpha\bar{u} - \omega}\ \frac{d\bar{\rho}}{dy}$$

Substituting for ρ' in the equation of motion then yields:

$$\left(\bar{u} - \frac{\omega}{\alpha}\right)\left(\phi'' - \alpha^2\phi\right) - \bar{u}''\,\phi + \frac{\bar{\rho}'}{\bar{\rho}}\left[\left(\bar{u} - \frac{\omega}{\alpha}\right)\phi' - \bar{u}'\,\phi\right]$$

$$= \frac{\mu}{i\alpha\bar{\rho}}\left(\phi^{iv} - 2\alpha^2\,\phi'' + \alpha^4\,\phi\right)$$

$$+ \frac{g_x}{i\alpha\bar{\rho}\left(\bar{u} - \frac{\omega}{\alpha}\right)}\left(\bar{\rho}'\phi' + \bar{\rho}'\bar{u}'\,\frac{\phi}{u - \frac{\omega}{\alpha}} + \bar{\rho}''\phi\right) - \frac{g_y}{\bar{\rho}\left(\bar{u} - \frac{\omega}{\alpha}\right)}\,\bar{\rho}'\,\phi$$

where the primes now indicate differentiation with respect to y.

The equation is now non-dimensionalized with reference lengths for the velocity and density gradients, δ and ϵ respectively, and with a characteristic velocity, U. The final equation is then:

$$\left(\bar{u} - \frac{\omega}{\alpha}\right)\left(\phi'' - \alpha^2 \phi\right) - \bar{u}'' \phi + \frac{\bar{\rho}'}{\bar{\rho}} \frac{\delta}{\epsilon} \left[\left(\bar{u} - \frac{\omega}{\alpha}\right)\phi' - \bar{u}'\phi\right]$$

$$= \frac{1}{Re_\delta} \frac{1}{i\alpha} \left(\phi^{iv} - \alpha^2 \phi'' + \alpha^4 \phi\right)$$

$$+ \frac{1}{Fr_x} \left\{ \frac{\delta}{\epsilon} \frac{\bar{\rho}'}{\bar{\rho}} \frac{1}{i\alpha} \left[\frac{\phi'}{\bar{u} - \frac{\omega}{\alpha}} + \frac{\bar{u}'\phi}{\left(\bar{u} - \frac{\omega}{\alpha}\right)^2} \right] + \left(\frac{\delta}{\epsilon}\right)^2 \frac{\bar{\rho}''}{\bar{\rho}} \frac{1}{i\alpha} \frac{\phi}{\bar{u} - \frac{\omega}{\alpha}} \right\}$$

$$- \frac{1}{Fr_y} \frac{\delta}{\epsilon} \frac{\bar{\rho}'}{\bar{\rho}} \frac{\phi}{\bar{u} - \frac{\omega}{\alpha}}$$

where all parameters are now non-dimensional and:

$$Re_\delta = \frac{\bar{\rho}\, U\, \delta}{\mu}$$

$$Fr_x = \frac{U^2}{g_x \delta} \quad ; \quad Fr_y = \frac{U^2}{g_y \delta}$$

REFERENCES

1. Freymuth, P., "On Transition in a Separated Laminar Boundary Layer," J. Fluid Mech., 25, 683 (1966).

2. Michalke, A., "The Instability of Free Shear Layers: A Survey on the State of Art," Deutche Luft- und Raumfahrt, Mitt. 70-04 (1970).

3. Taylor, G. I., "Effect of Variation in Density on the Stability of Superposed Streams of Fluid," Proc. Roy. Soc. A, 132, 499 (1931).

4. Miles, J. W., "On the Stability of Heterogeneous Shear Flows," J. Fluid Mech., 10, 496 (1961).

5. Gropengiesser, H., "Beitrag zur Stabilität freier Grenzschichten in kompressiblen Medien," Deutche Luft- und Raumfahrt, Forsch.-Ber. 69-25 (1969).

6. Menkes, J., "On the Stability of a Shear Layer," J. Fluid Mech., 6, 518 (1959).

7. Maslowe, S. A., "A Theoretical Study of the Stability of Stratified Shear Layers," Ph.D. Thesis, University of California at Los Angeles (1970).

8. Tombach, I. H., "Velocity Measurements with a New Probe in Inhomogeneous Turbulent Jets," Ph.D. Thesis, California Institute of Technology (1969).

9. Way, J. and Libby, P., "Hot-Wire Probes for Measuring Velocity and Concentrations in Helium-Air Mixtures," AIAA J., 8, 976 (1970).

10. Brown, G. L. and Rebollo, M., "A Probe to Measure Density," to be published.

11. Sato, H., "Further Investigation on the Transition of Two-Dimensional Separated Layer at Subsonic Speeds," J. Physical Soc. of Japan, 14, 1797 (1959).

12. Browand, F. K., "An Experimental Investigation of the Instability of an Incompressible, Separated Shear Layer," J. Fluid Mech., 26, 281 (1966).

13. Corrsin, S., "Extended Applications of the Hot-Wire Anemometer," NACA TN 1864 (1949).

REFERENCES (cont.)

14. Collis, D. C. and Williams, M. J., "Two-Dimensional Convection from Heated Wires at Low Reynolds Numbers," J. Fluid Mech., 6, 357 (1959).

15. Michalke, A., "On Spatially Growing Disturbances in an Inviscid Shear Layer," J. Fluid Mech., 23, 521 (1965).

16. Michalke, A., "The Influence of the Vorticity Distribution on the Inviscid Instability of a Free Shear Layer," Fluid Dynamics Transactions, 4, 751 (1969).

17. Sato, H., "Experimental Investigation on the Transition of Laminar Separated Layer," J.Physical Soc. of Japan, 11, 702 (1956).

18. Baker, R. L., Rozenman, T. and Weinstein, H., "Stability of Shear Flow with Density Gradient and Viscosity," NASA CR-958 (1968).

19. Landau, L. D. and Lifshitz, E. M., Fluid Mechanics, Addison-Wesley Publishing Co. Inc., Reading, Mass., 116 (1959).

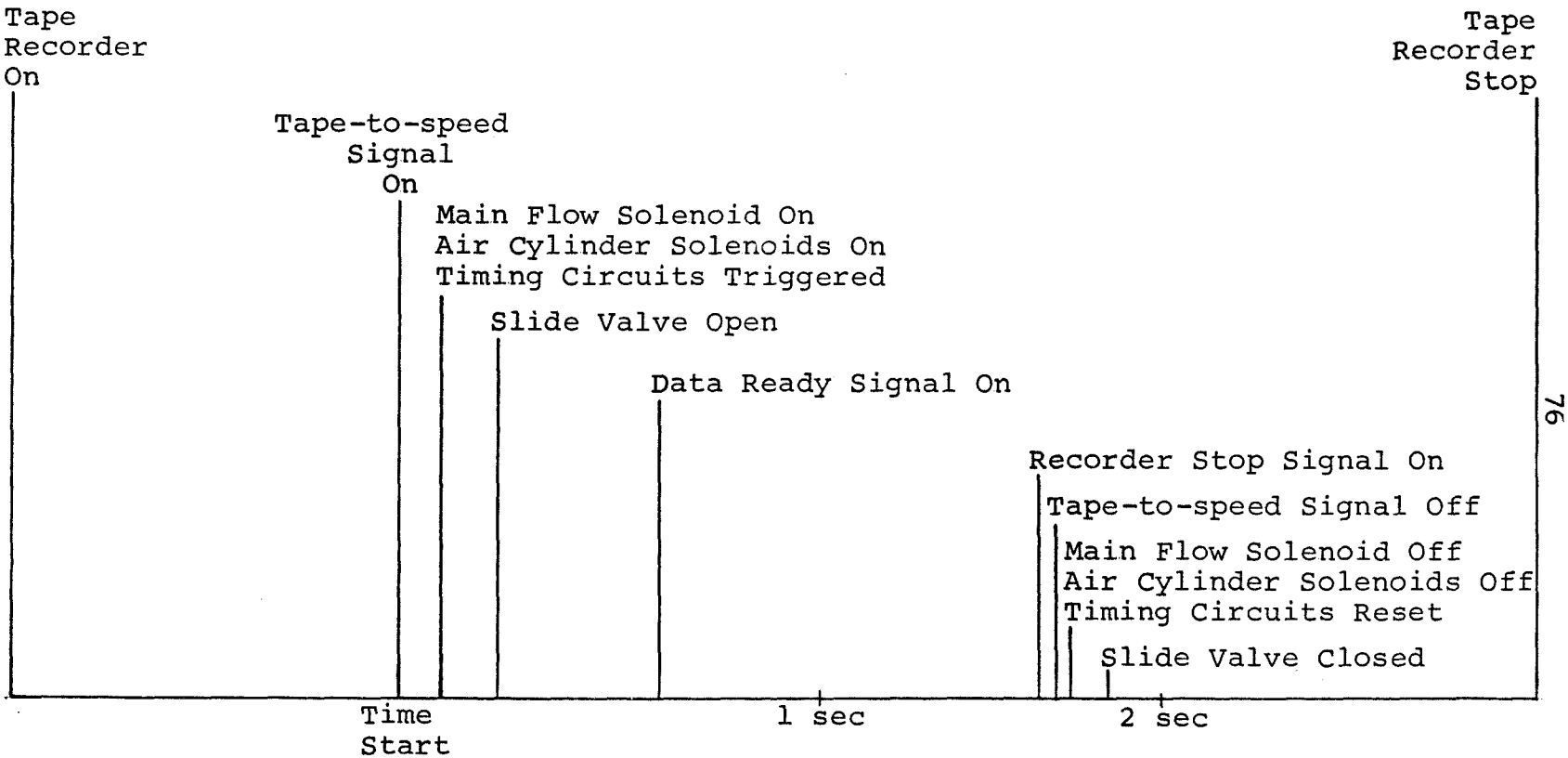

Table 1. Run sequence of events.

	Freon 22	Freon 114	Ratio: 114/22
Molecular Weight	86.48	170.93	1.976
k $\frac{BTU}{hr\ ft\ ^oF}$	.00678	.00646	.954
μ_f (poise)	1.59×10^{-4}	1.40×10^{-4}	.881
$k/\mu_f^{0.45}$			.991

Table 2. Properties of Freon 22 and Freon 114.

	Freon 22	Freon 114
Flow Rate	.577 gm/sec-cm^2	.515 gm/sec-cm^2
Velocity	330 cm/sec	150 cm/sec
Tank Pressure	7 psia	7 psia
Reynolds number = $\frac{\rho U \theta}{\mu}$	$\simeq$ 120	$\simeq$ 120
Froude Number = $\frac{U_o^2}{\delta g}$	$\simeq$ 300	$\simeq$ 100

Table 3. Selected flow conditions.

1. Record calibration voltages
2. Calibrate hot wires in both gases
3. Evacuate system
4. Refill tank and settling chamber
5. Turn on loudspeaker
6. Run; note flow pressure and probe position
7. Turn off loudspeaker
8. Repeat steps 3 - 7 as necessary
9. Recalibrate at least every hour

Table 4. Operating sequence.

Gas used:	Freon 22
Mass flow rate:	.573 gm/sec-cm^2
Jet velocity:	336 cm/sec
Jet Reynolds number:	4230
$Re_d = \frac{\rho U d}{\mu}$	
Momentum thickness Reynolds number:	111
$Re_\theta = \frac{\rho U \theta}{\mu}$	
Tank pressure:	7 psia
Forcing frequency:	195.2 Hz
Forcing amplitude:	73 db

Table 5. Flow conditions, homogeneous flow.

	Present	Browand	Freymuth
θ_{ref}	.25 mm	.89 mm	.9 mm
$\frac{\theta_{ref}}{\theta_o}$	1.52	1.41	1.2
$\frac{\theta_{ref}}{\lambda}$	.028	.028	.024*
$\frac{x_{ref}}{\theta_o}$	25	22	10

* comparable Strouhal number

Table 6. Comparison of reference lengths.

Quantity	Present Value	Previous Value	Source
Strouhal number for natural oscillations:			
$S = \frac{2\pi f \theta_{ref}}{U}$	.090	.092 .10	Browand Sato
$S = \frac{2\pi f \delta_o^*}{U}$	.0235	.023	Michalke
Growth rate:			
$-\alpha_i = \frac{\theta_{ref}}{x^2-x^1} \ln \frac{\hat{c}^2}{\hat{c}^1}$	$\hat{c}_1$: .12	.09	Freymuth
	$\hat{c}_2$: .081	.088 .09 .11	Freymuth Sato Browand
$\hat{c}_1/\hat{c}_2$	.34 - .42	.35	Freymuth
Wave number:			
$\alpha_r = \frac{2\pi \theta_{ref}}{\lambda}$	.174	.162 .18	Freymuth Browand

Table 7. Comparison of present and previous oscillation parameters: homogeneous flow.

Parameter	Freon 22 into Freon 114	Freon 114 into Freon 22
Mass flow rate	.580 gm/sec-cm^2	.510 gm/sec-cm^2
Velocity	335 cm/sec	150 cm/sec
$Re_{\tilde{\theta}} = \frac{\rho U \tilde{\theta}_{ref}}{\mu}$	112	134
$Re_d = \frac{\rho U d}{\mu}$	4310	4260
$Fr_{\tilde{\theta}} = \frac{U^2}{\tilde{\theta}_{ref} g}$	4610	765
$\tilde{\theta}_{ref}$	.248 mm	.300 mm
Forcing frequency	156.2 Hz	97.6 Hz
Forcing amplitude	72 db	75 db

Table 8. Flow conditions: heterogeneous flow.

Parameter	22 into 114		Homogeneous		114 into 22	
	Exp	Theory*	Exp	Theory*	Exp	Theory*
$S = \omega_{natural} = \frac{2\pi\ \tilde{\theta}_{ref}\ f_{nat}}{U}$	.0697	.0761	.090	.106	.112-.147	.129
$\omega_{forcing}$	.0726	---	.0915	---	.123	---
$\alpha_r = \frac{2\pi\ \tilde{\theta}_{ref}}{\lambda}$	.190	.183	.174	.210	.218	.214
$\alpha_i = \frac{\tilde{\theta}_{ref}}{x^2-x^1} \ln \frac{\hat{c}^2}{\hat{c}^1}$	-.148	-.130	-.10	-.114	-.076	-.0904
Wave speed $= \frac{\omega}{\alpha_r}$	.382	.416	.526	.506	.564	.603
$\hat{c}_1/\hat{c}_2$	.88	.626	.35	.453	.148	.272

* Theoretical eigenvalues and eigenfunctions evaluated at the point of maximum disturbance amplification rate and scaled with the mass flow rate profile thickness of the Holmboe flow model.

Table 9. Comparison of experimental and theoretical eigenvalues and eigenfunctions for various flow cases

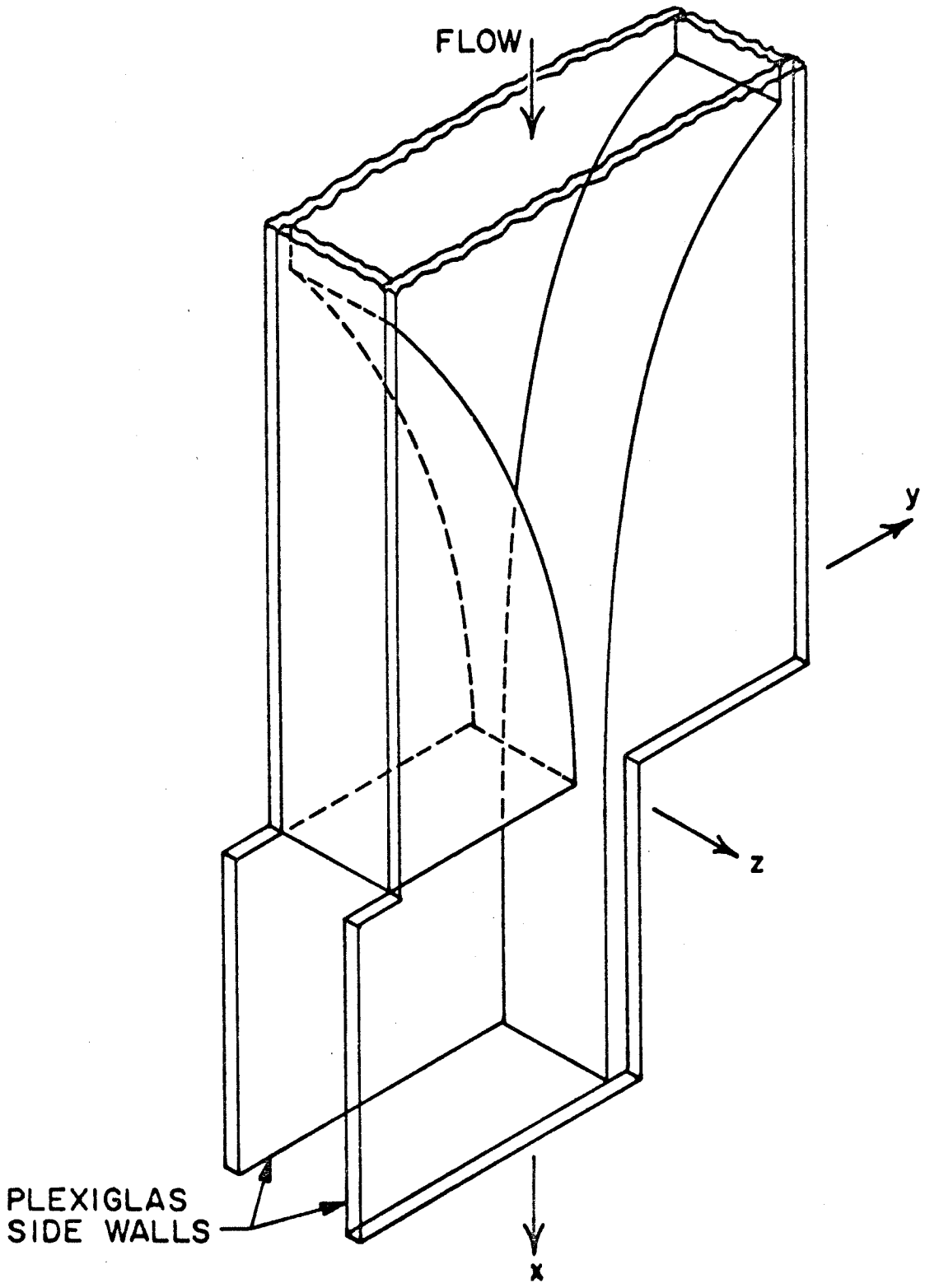

Figure 1. Flow geometry.

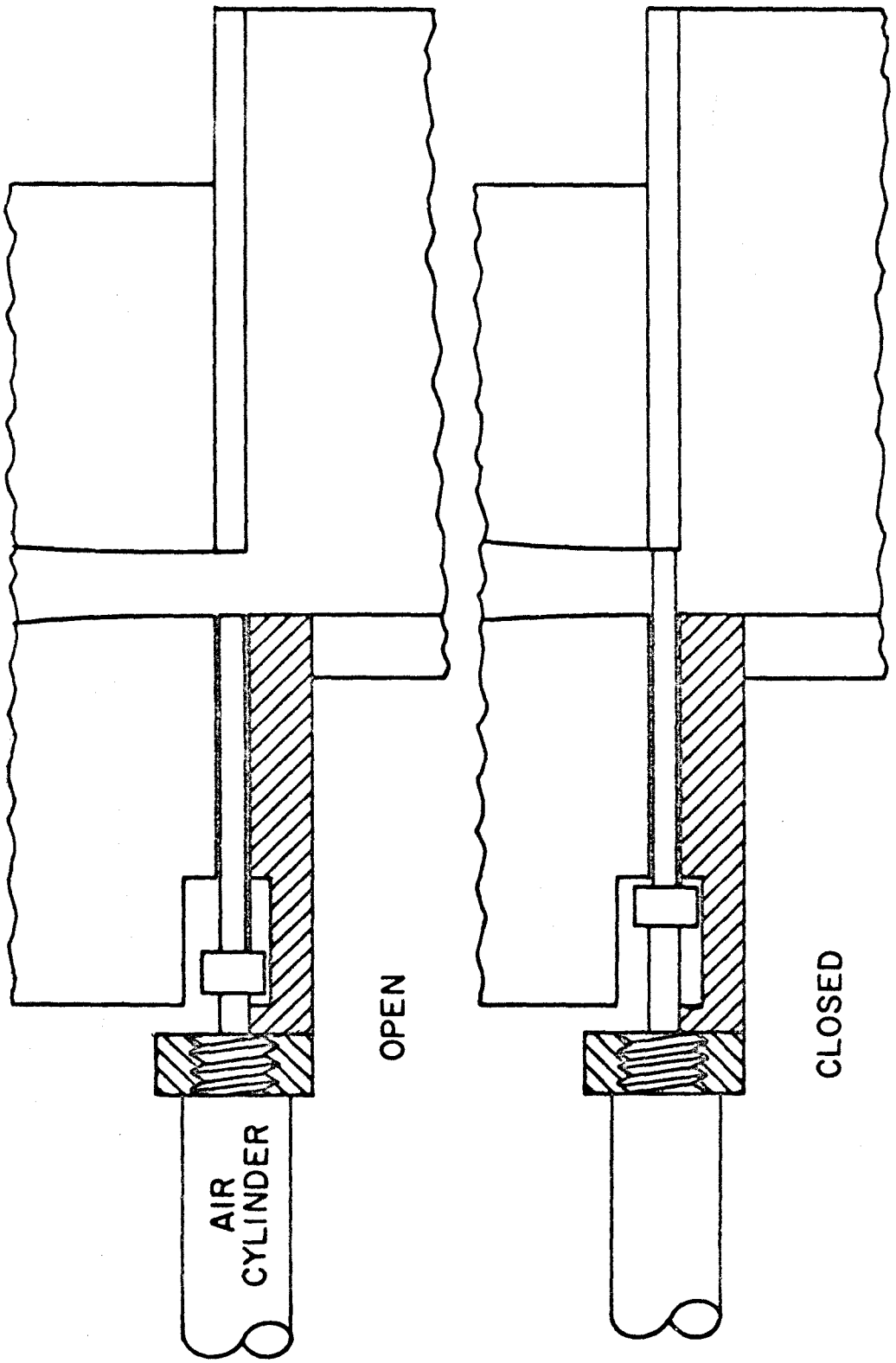

Figure 2. Slide valve.

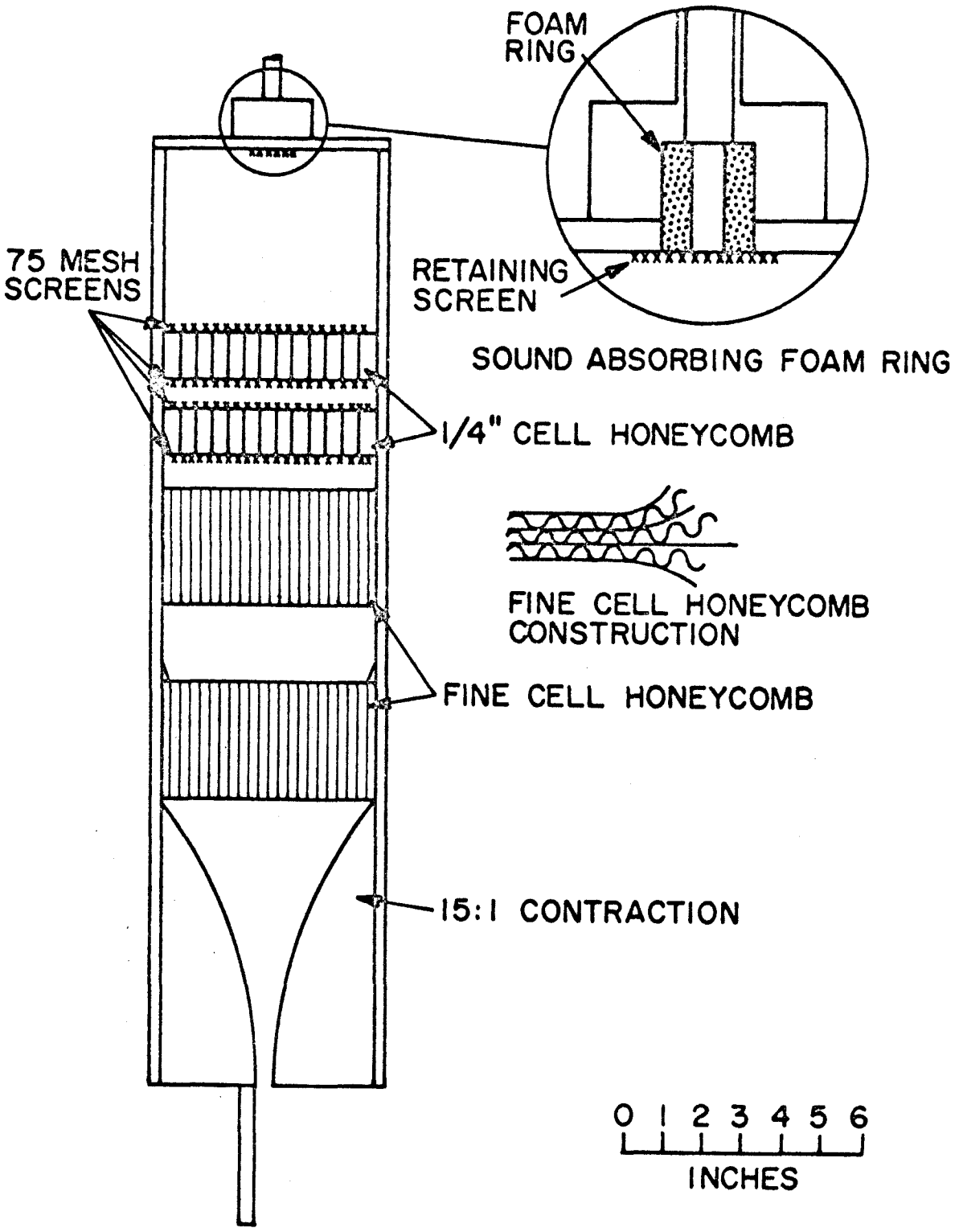

Figure 3. Turbulence reducing devices.

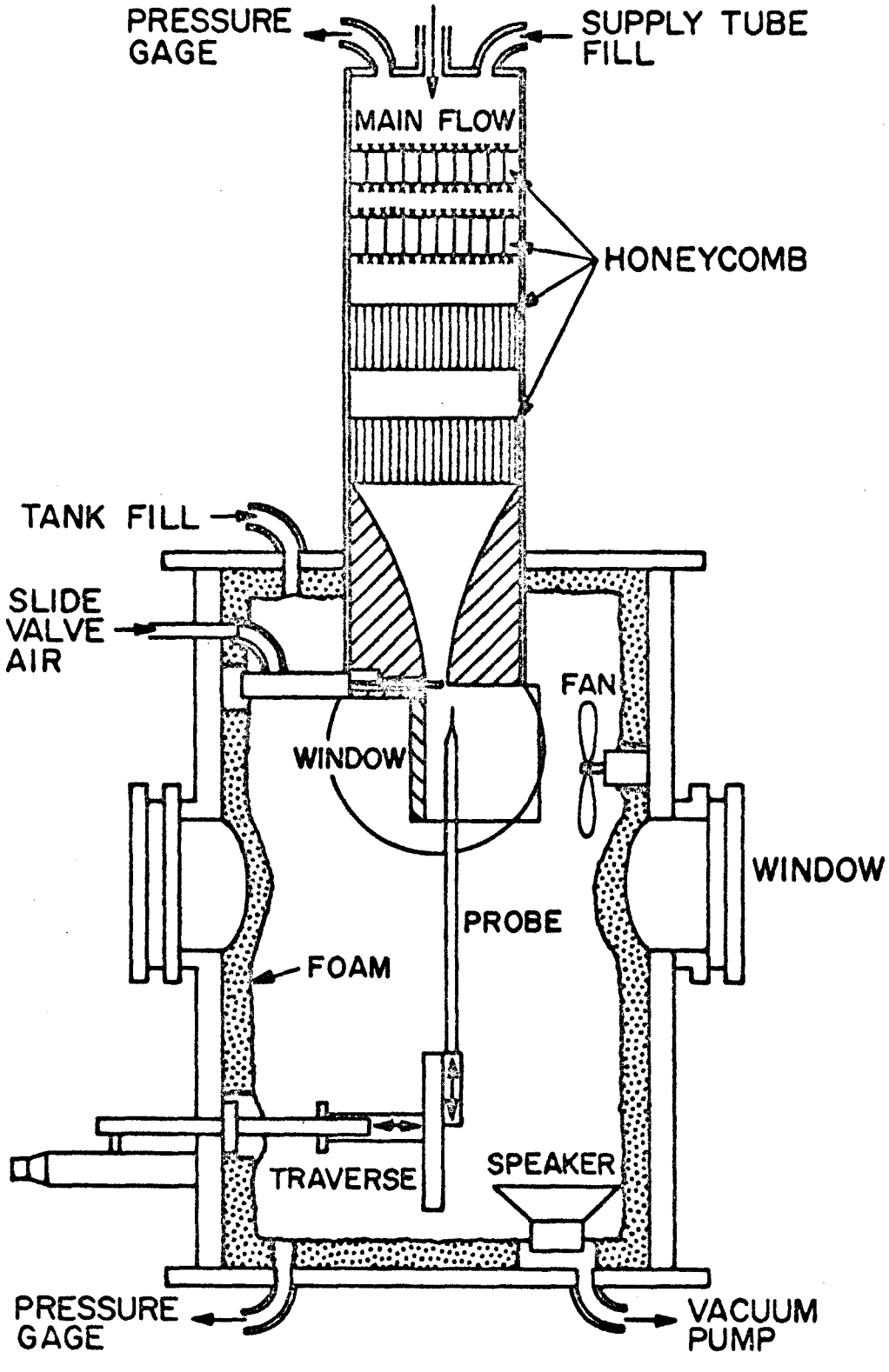

Figure 4. Jet Facility.

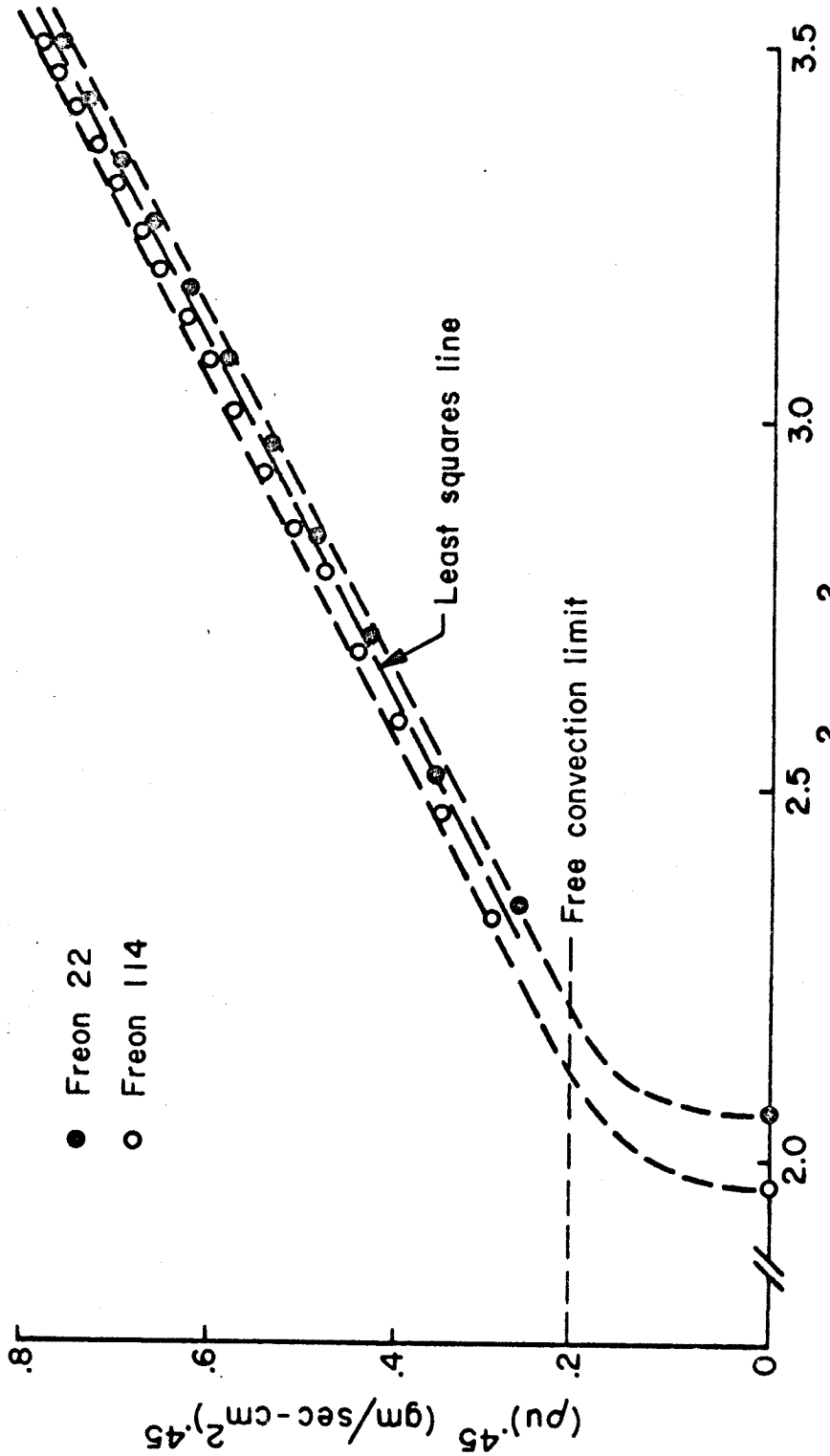

Figure 5. Hot wire calibration.

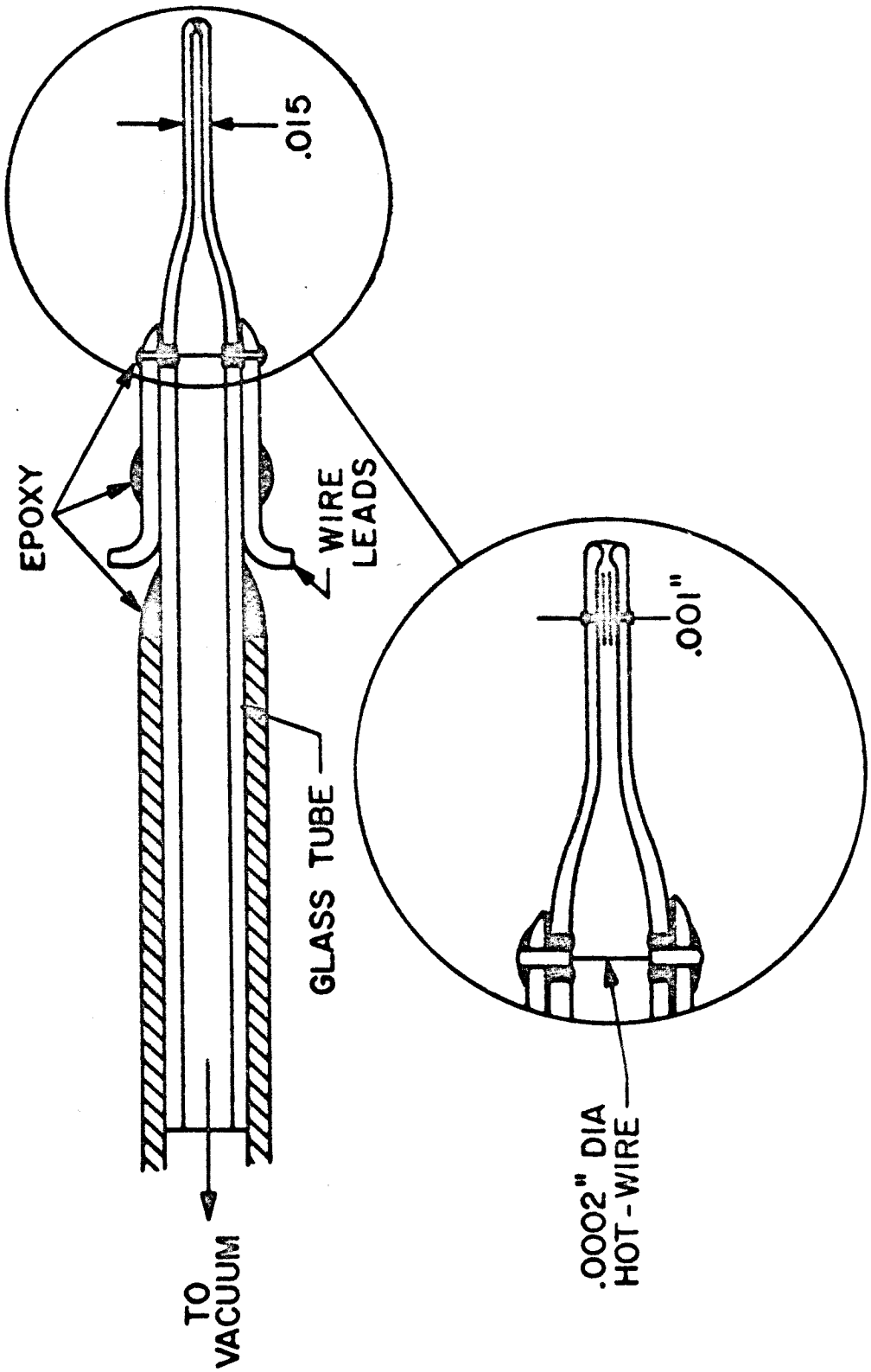

Figure 6. Aspirating probe construction.

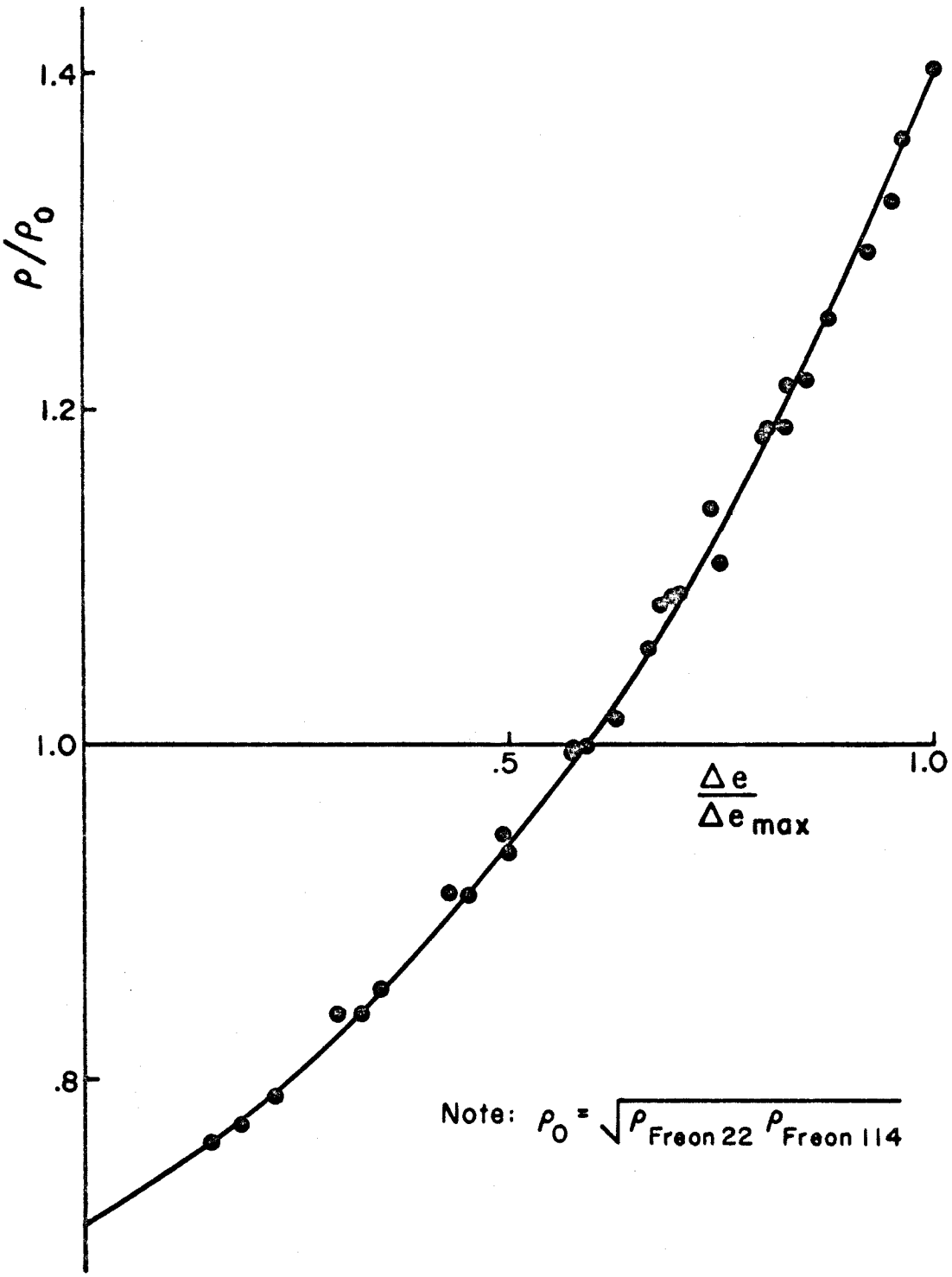

Figure 7. Aspirating probe calibration.

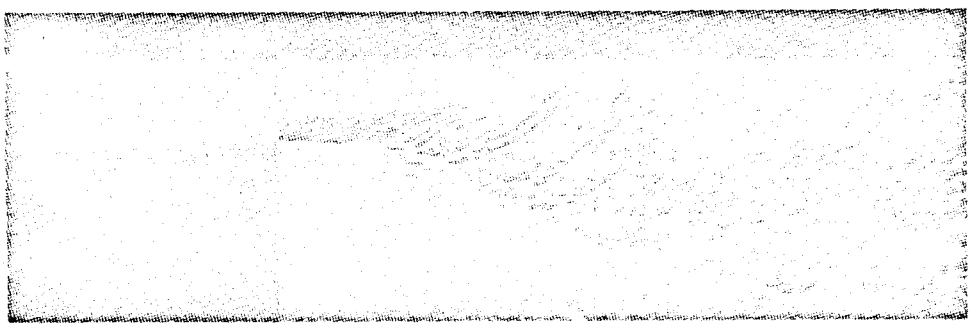

Helium into air: Re_d = 1600; d = jet width

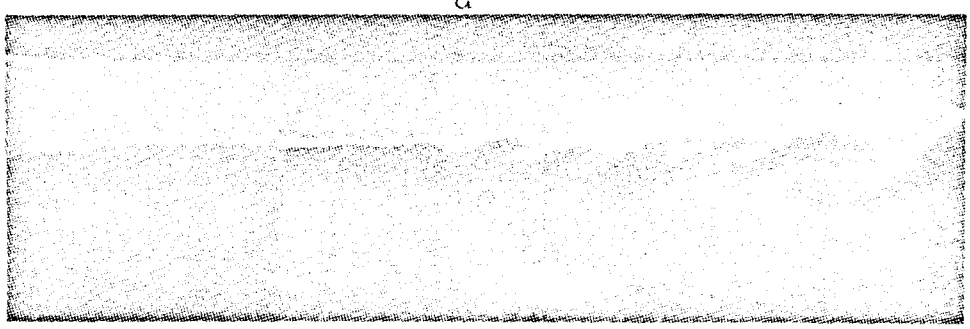

Air into helium: Re_d = 1800

Figure 8. Effect of density gradient on stability

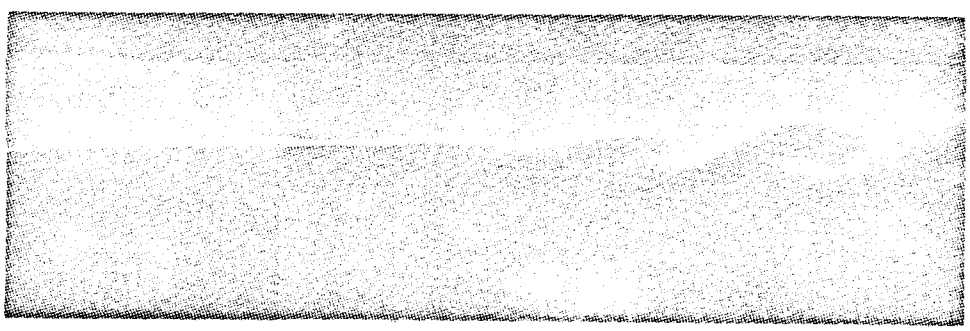

Air into helium: Re_d = 1500

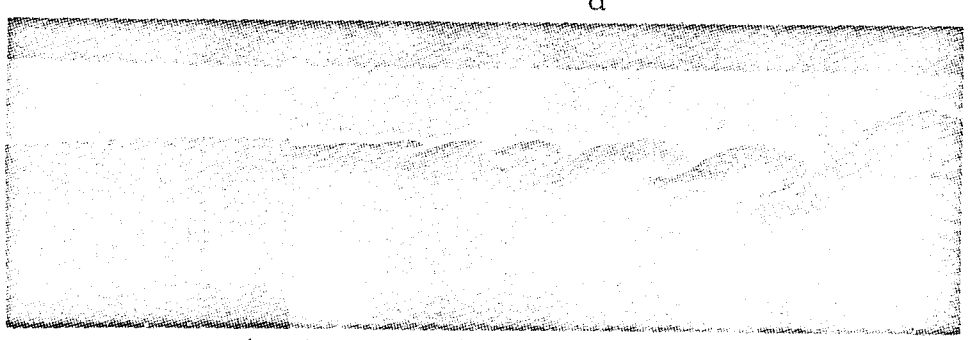

Air into helium: Re_d = 2800

Figure 9. Effect of Reynolds number on transition length

Freon 22 into Freon 114: Re_d = 6000

Figure 10. High Reynolds number with dense gas*

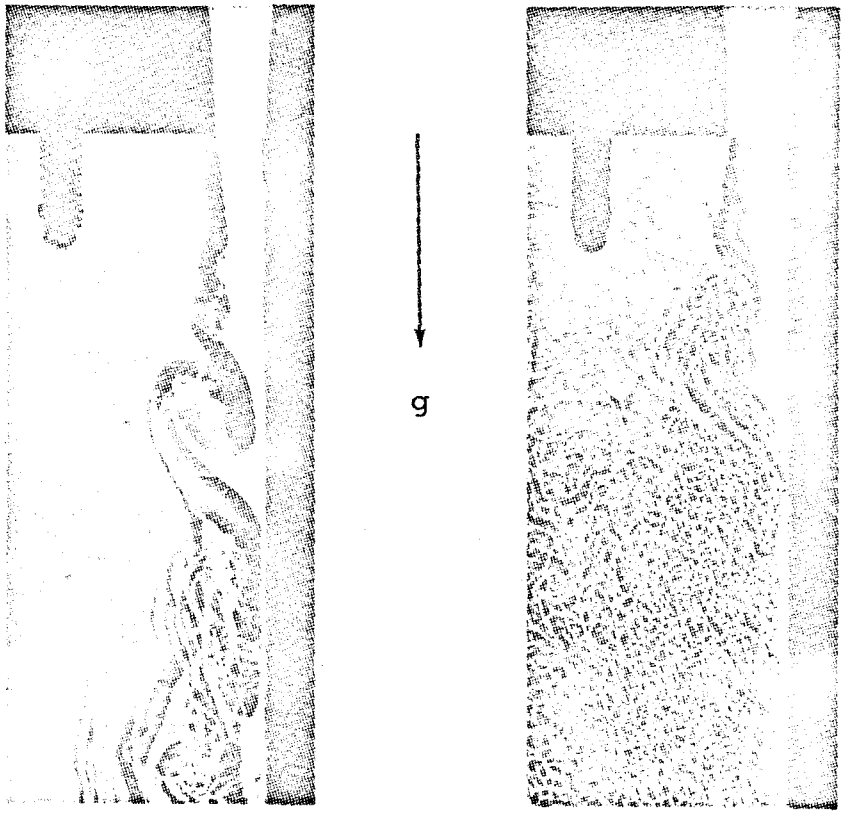

Freon 114 into Freon 22 Re_d = 5000

Freon 22 into Freon 114 Re_d = 5000

Figure 11. Effect of buoyancy forces: note curvature of shear layer at nozzle exit

---

* Object at left is a bolt holding the side wall.

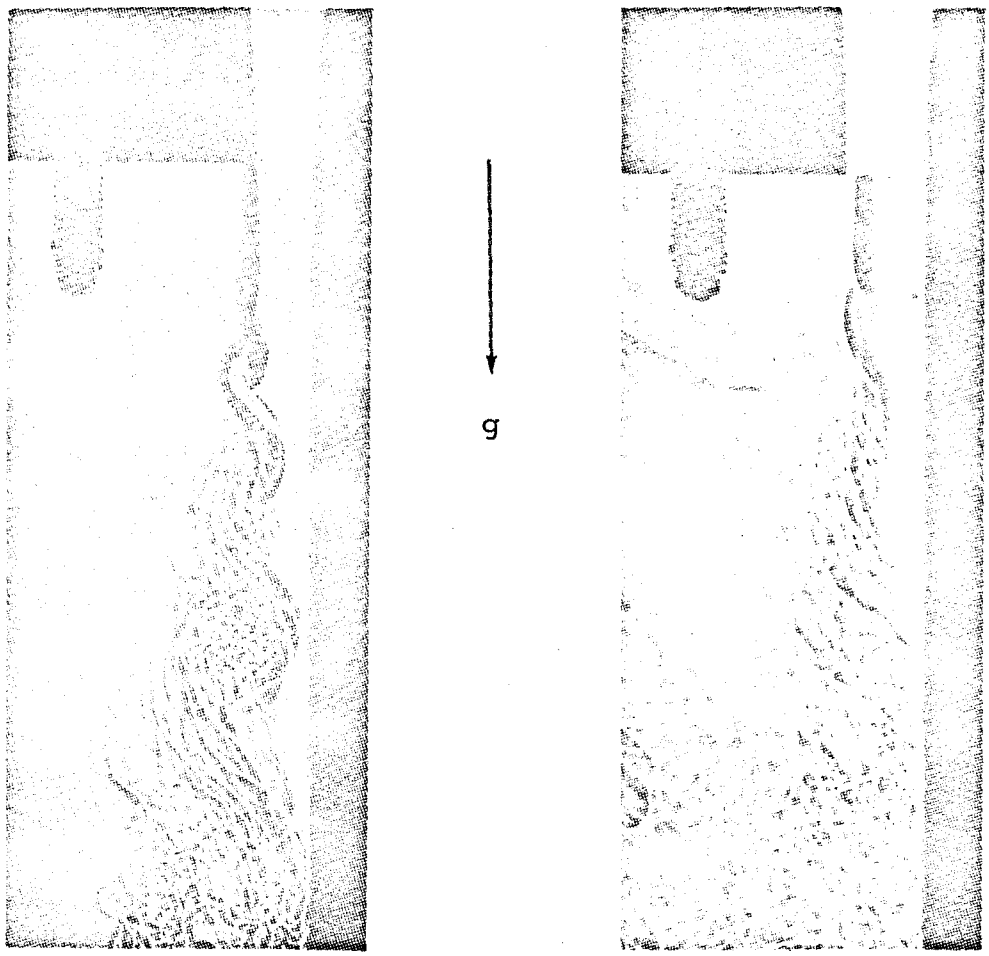

Freon 114 into Freon 22
Re_d = 5000

Freon 22 into Freon 114
Re_d = 3500

Figure 12. Reduction of buoyancy effect with tank pressure at 7 psia

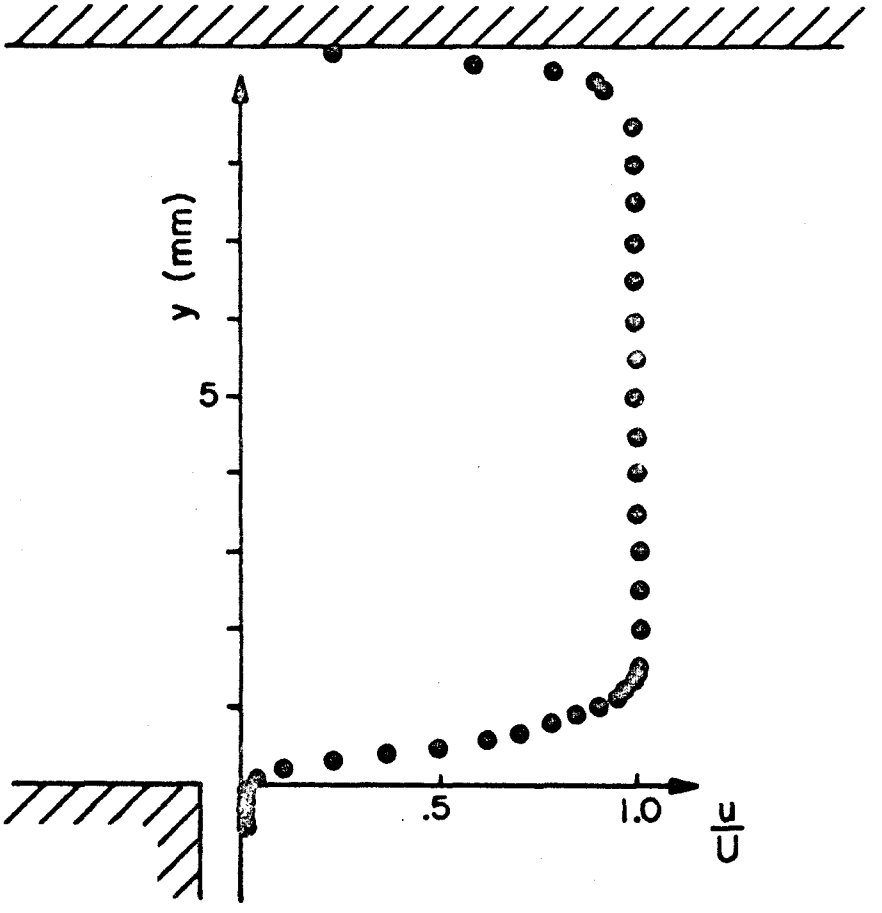

Figure 13. Jet velocity profile at x = .5 mm.

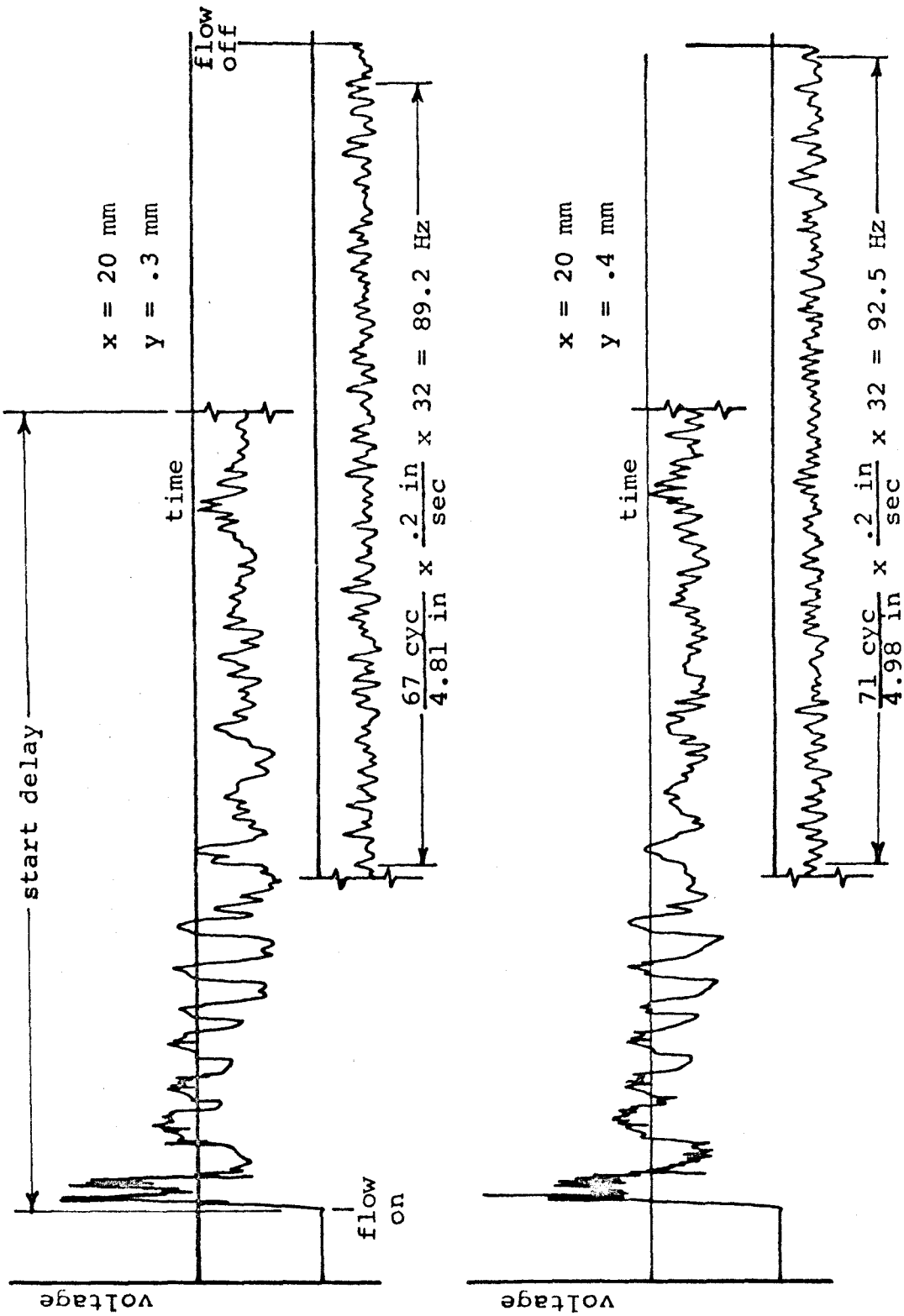

Figure 14. Natural oscillation frequency measurement: Freon 114 into Freon 22

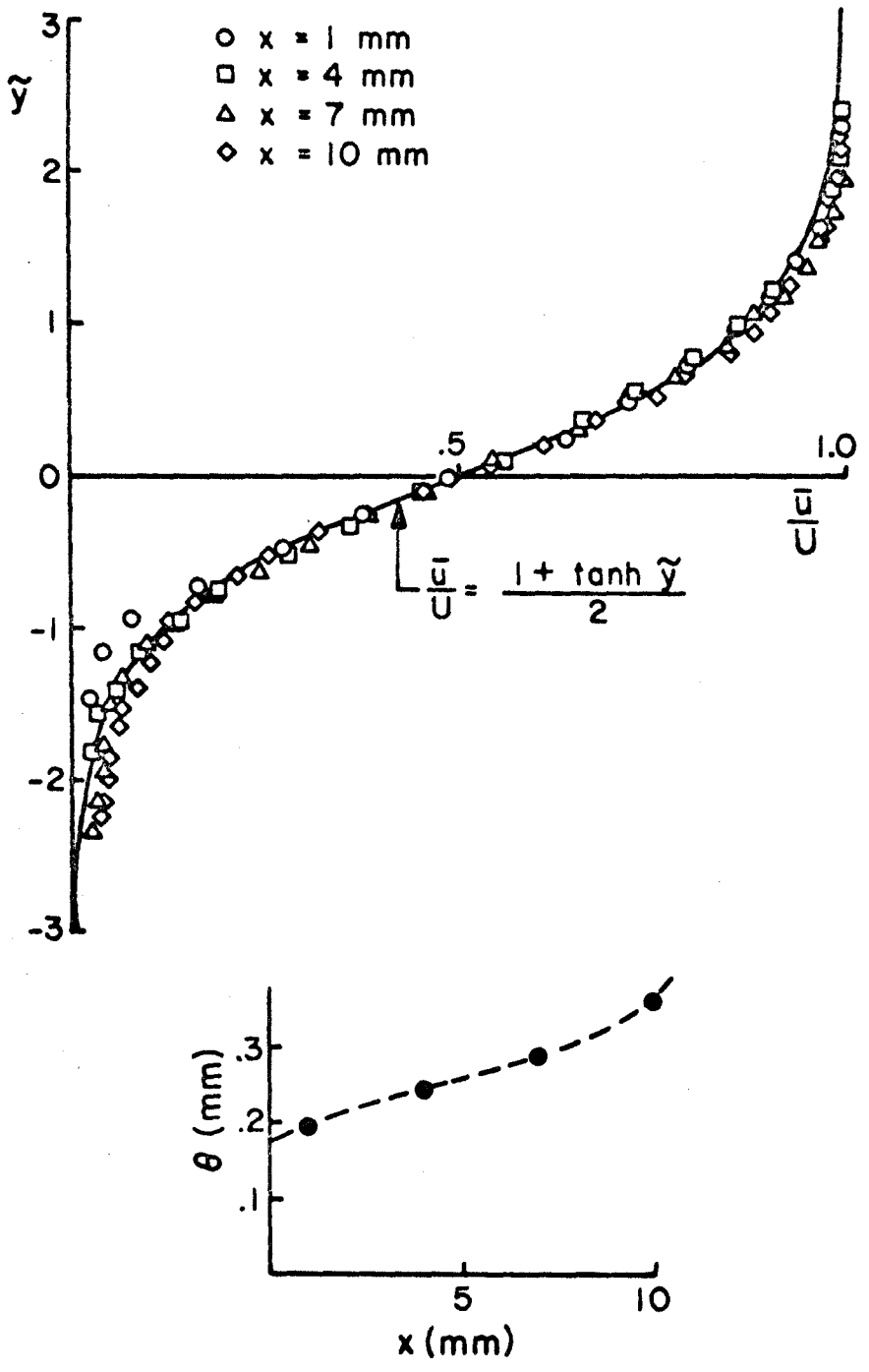

Figure 15. Mean velocity profiles: homogeneous flow.

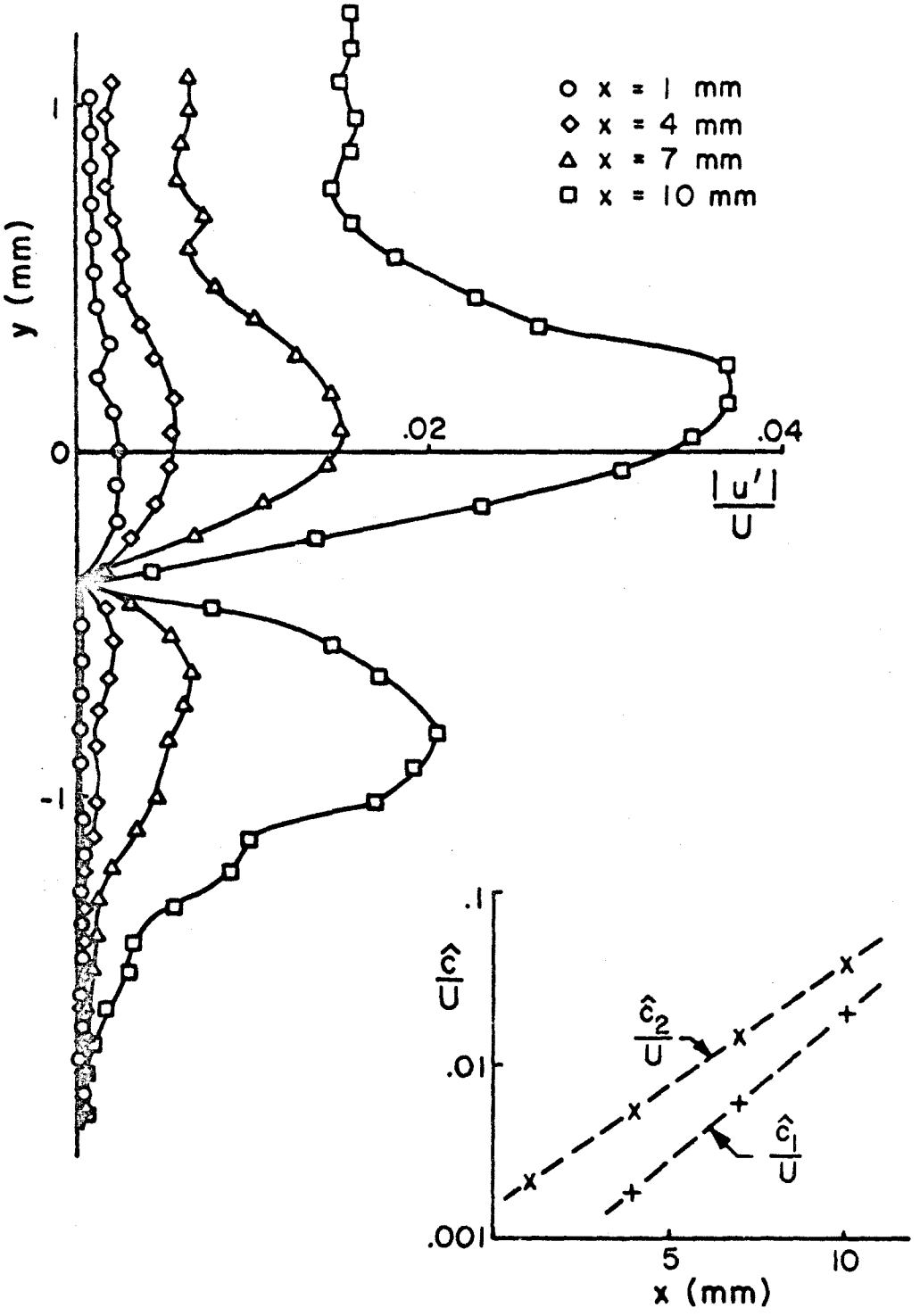

Figure 16. Amplitude of forcing frequency oscillations: homogeneous flow.

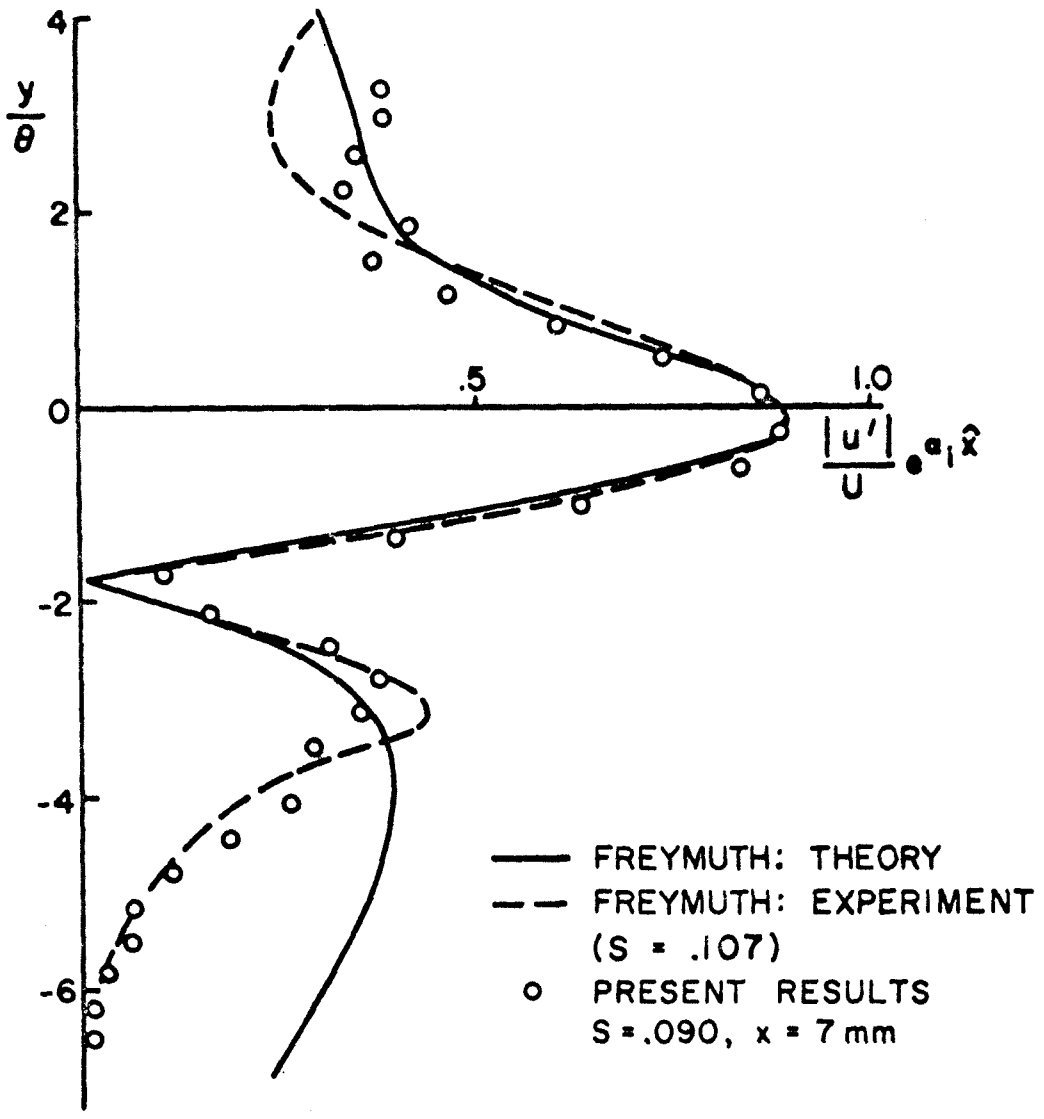

Figure 17. Comparison of forcing frequency oscillation amplitude measurements with results from Freymuth.

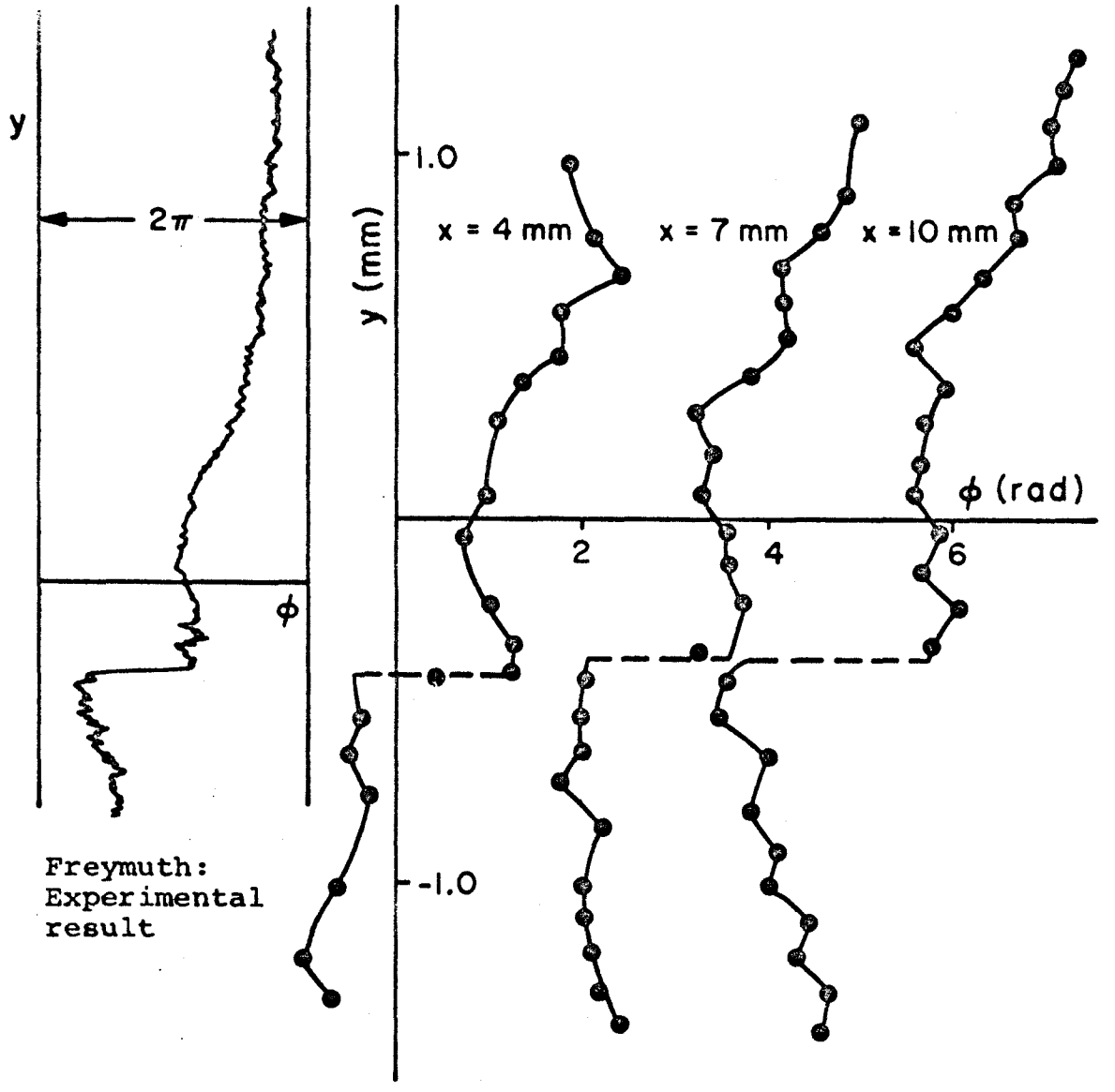

Figure 18. Phase of forcing frequency oscillations: homogeneous flow.

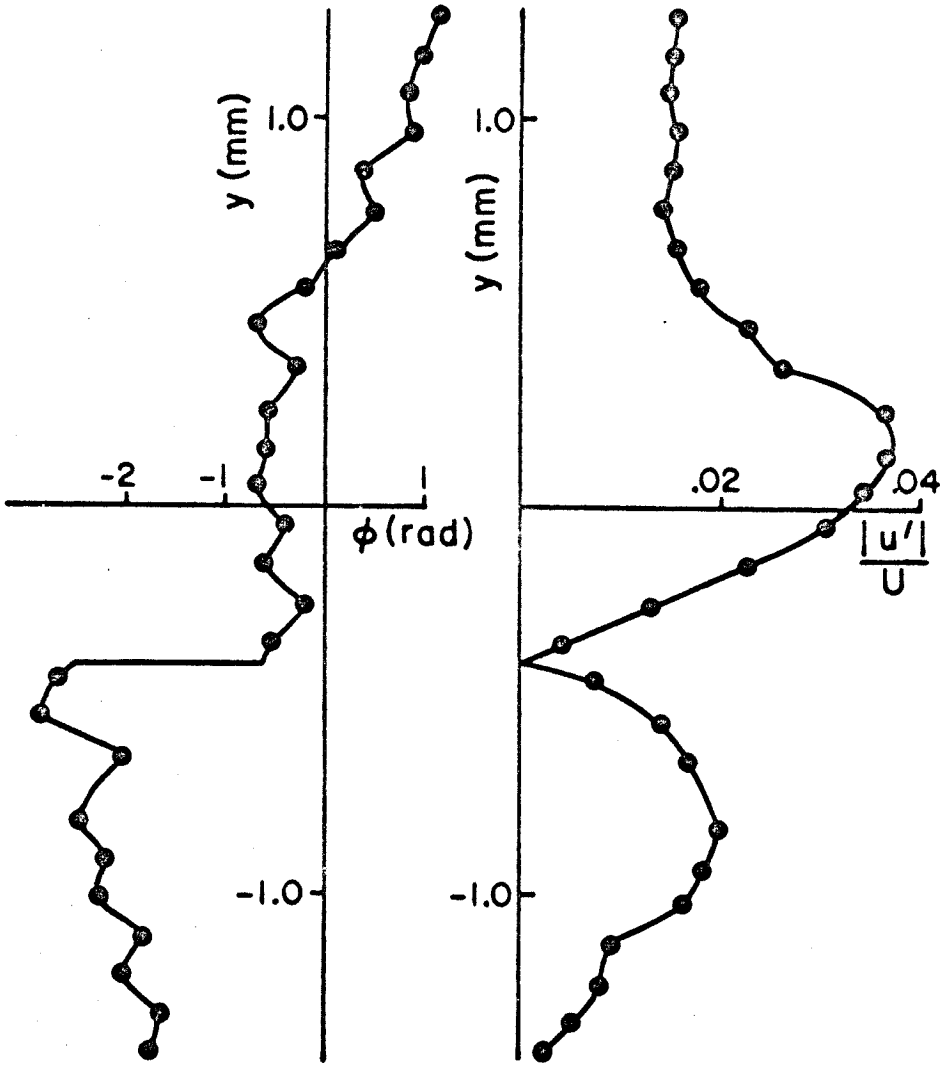

Figure 19. Amplitude and phase of forcing frequency oscillations: homogeneous flow, x = 10 mm.

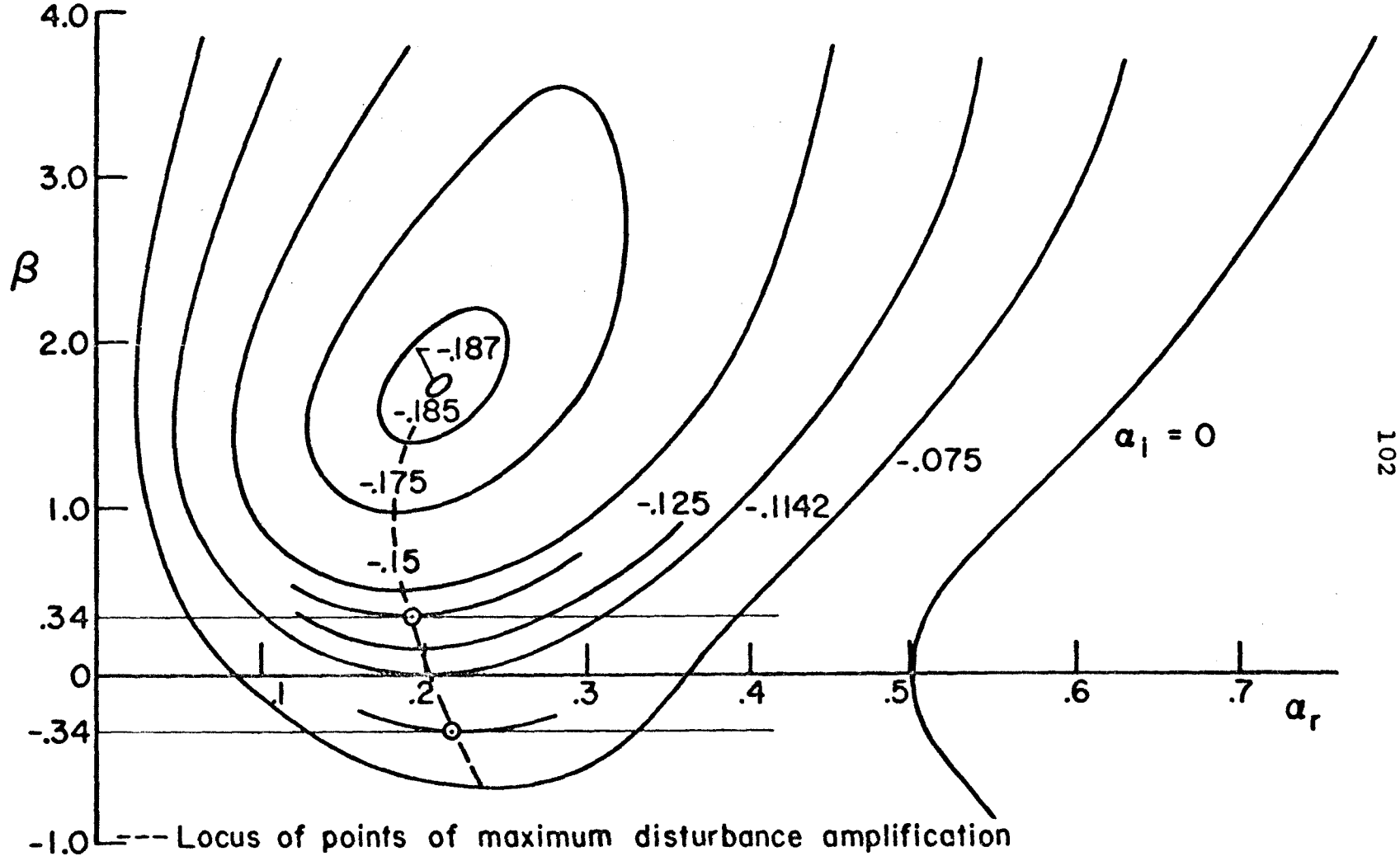

Figure 20. Effect of density gradient on eigenvalues as given by Maslowe.

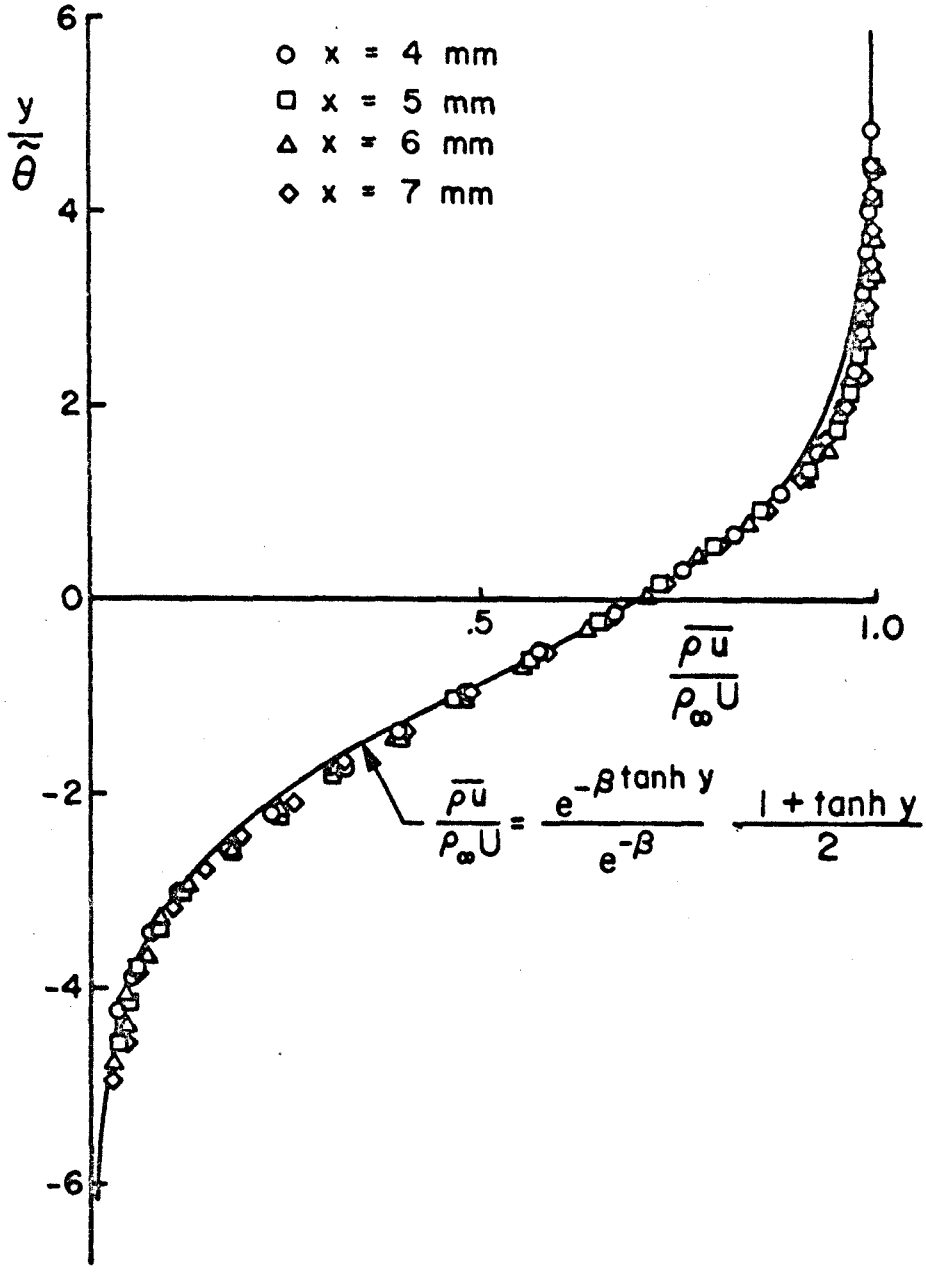

Figure 22. Mean mass flow rate profiles in developed laminar shear layer: Freon 22 into Freon 114.

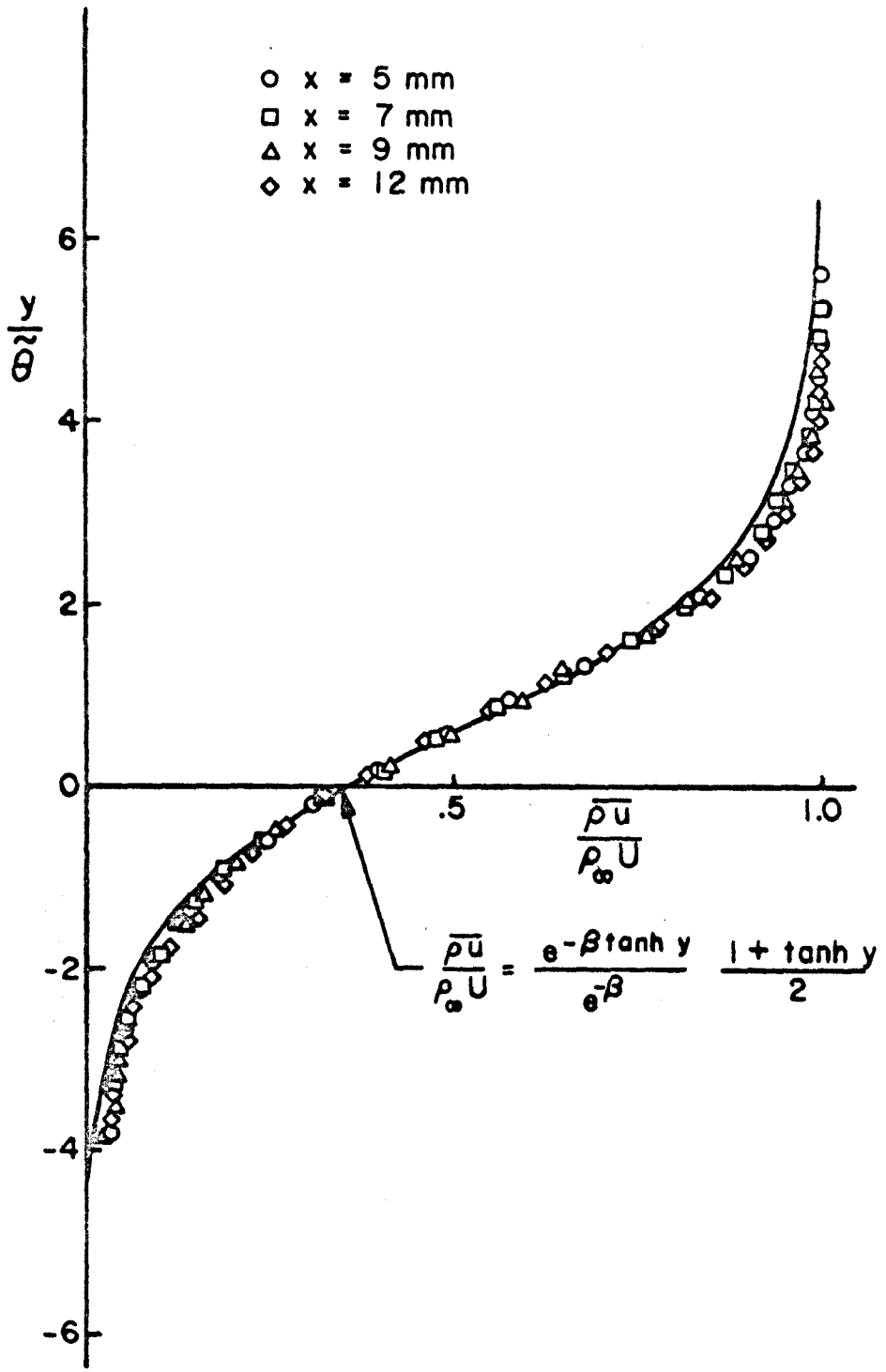

Figure 23. Mean mass flow rate profiles in developed laminar shear layer: Freon 114 into Freon 22.

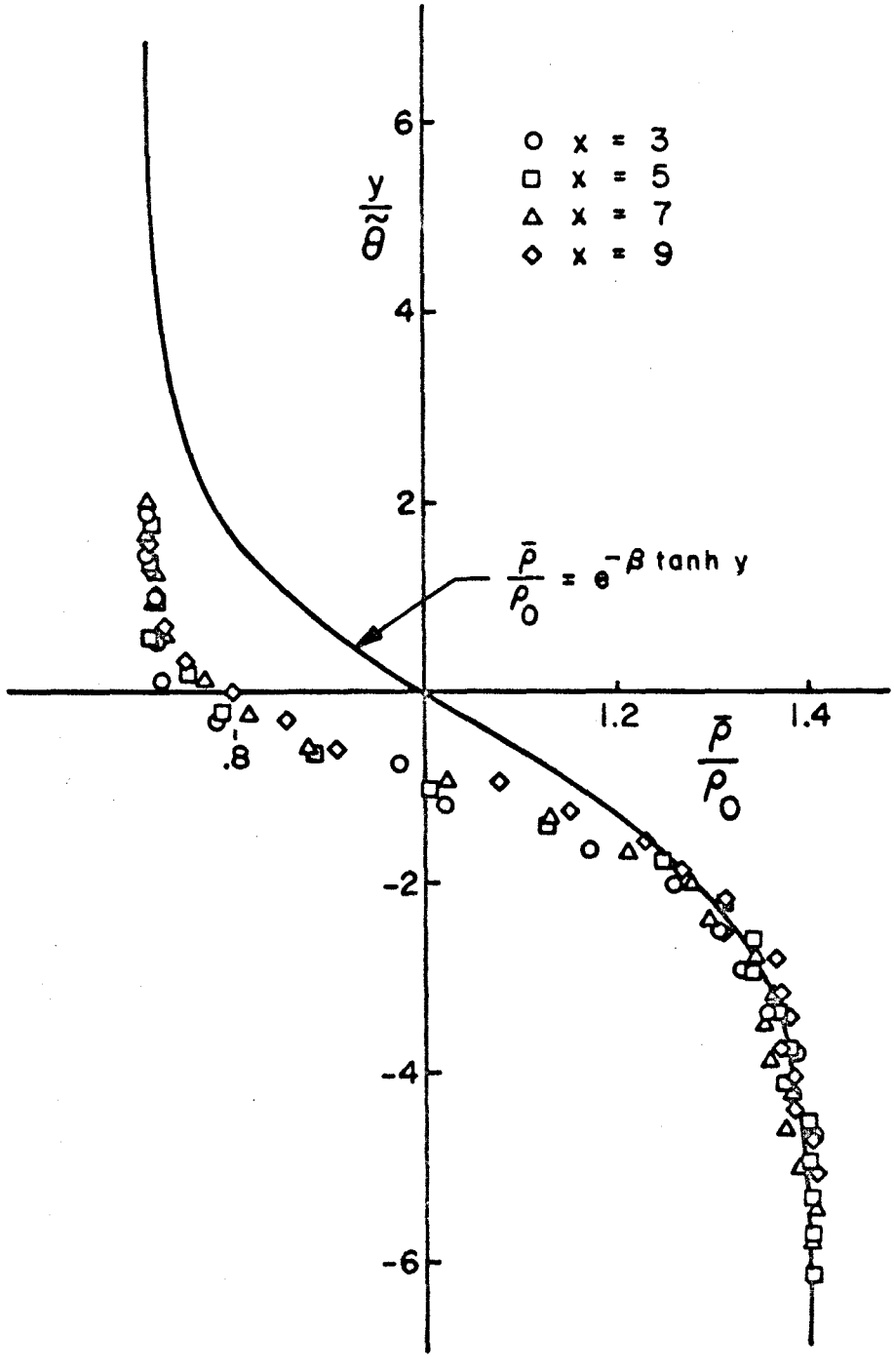

Figure 24. Mean density measurements: Freon 22 into Freon 114; $\beta = .34$.

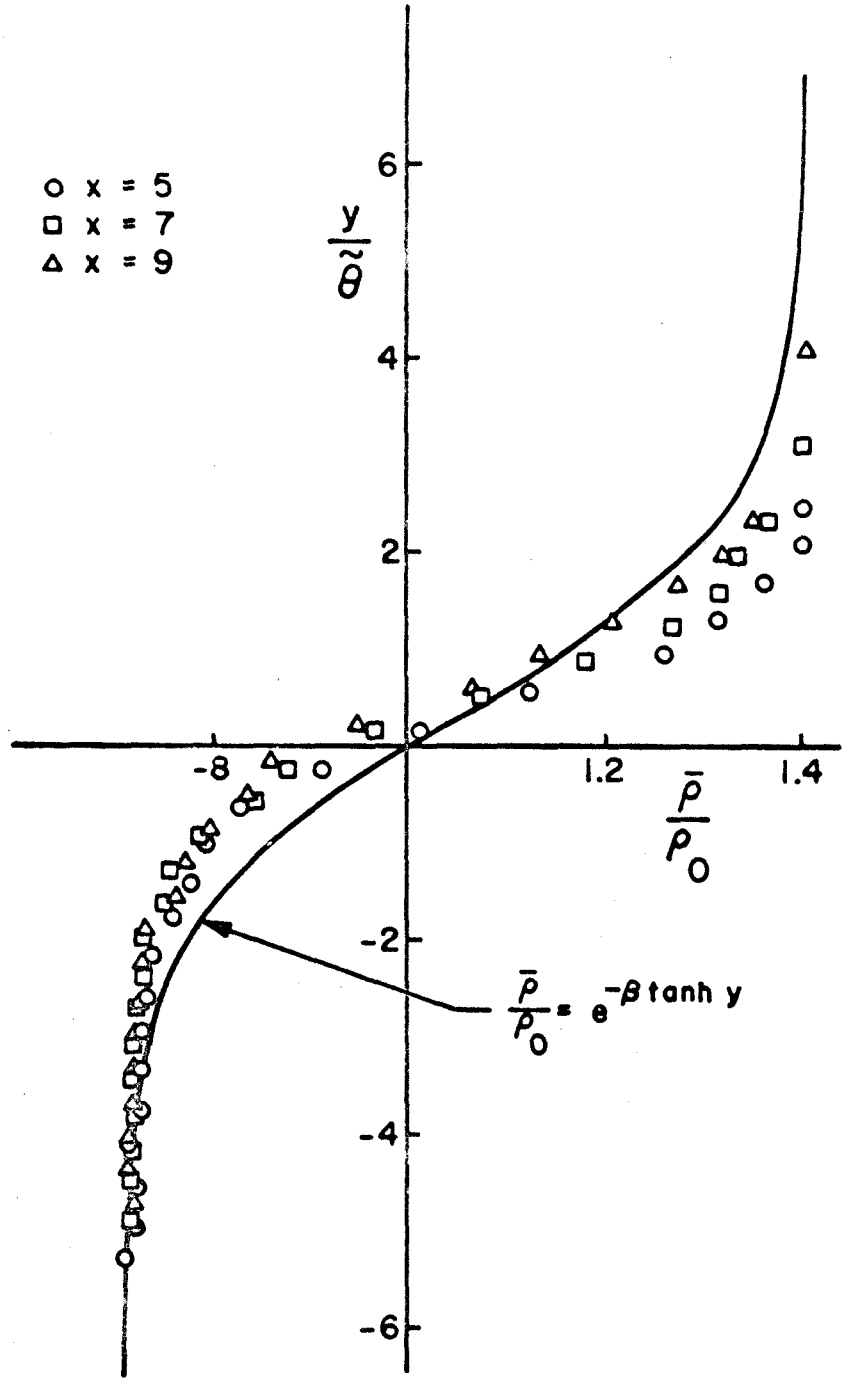

Figure 25. Mean density measurements: Freon 114 into Freon 22; $\beta = -.34$.

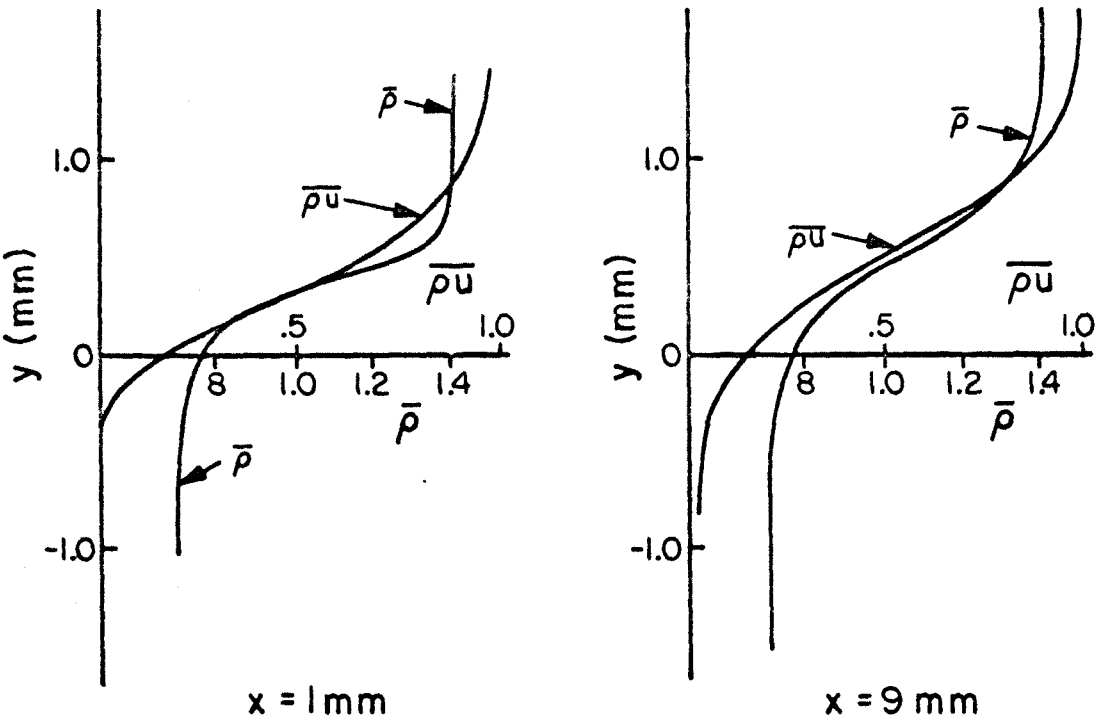

Freon 114 into Freon 22: $\beta = -.34$

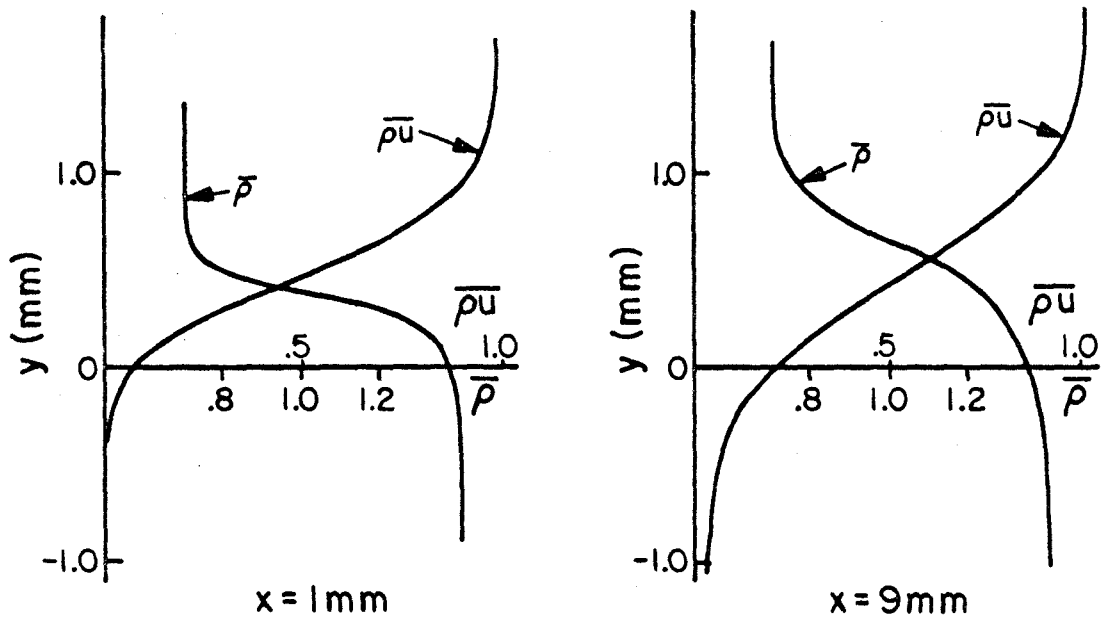

Freon 22 into Freon 114: $\beta = .34$

Figure 26. Comparison of density and mass flow rate profiles near the nozzle exit and in the similarity region.

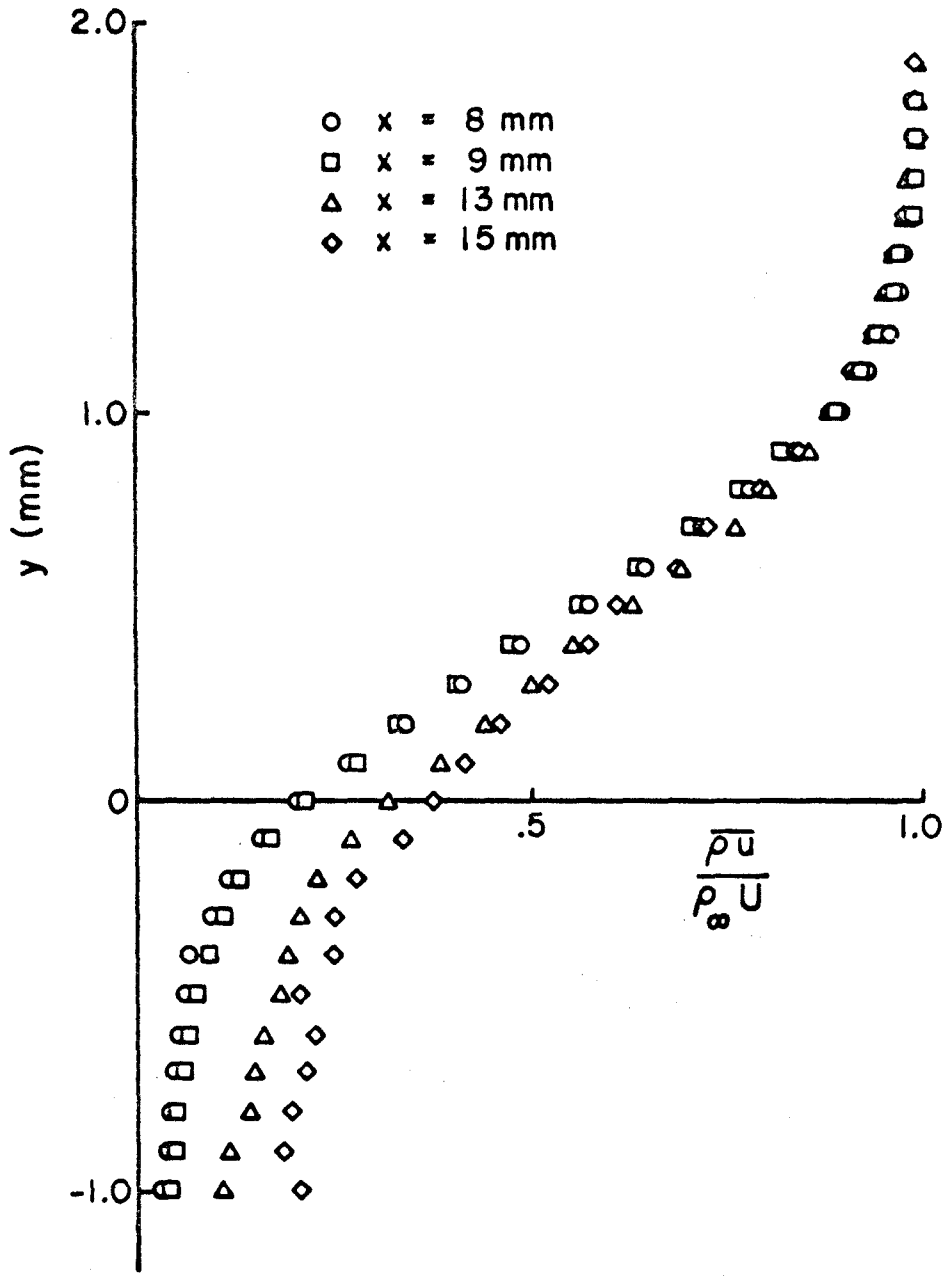

Figure 27. Mean mass flow rate profiles in region of transition to turbulence: Freon 22 into Freon 114.

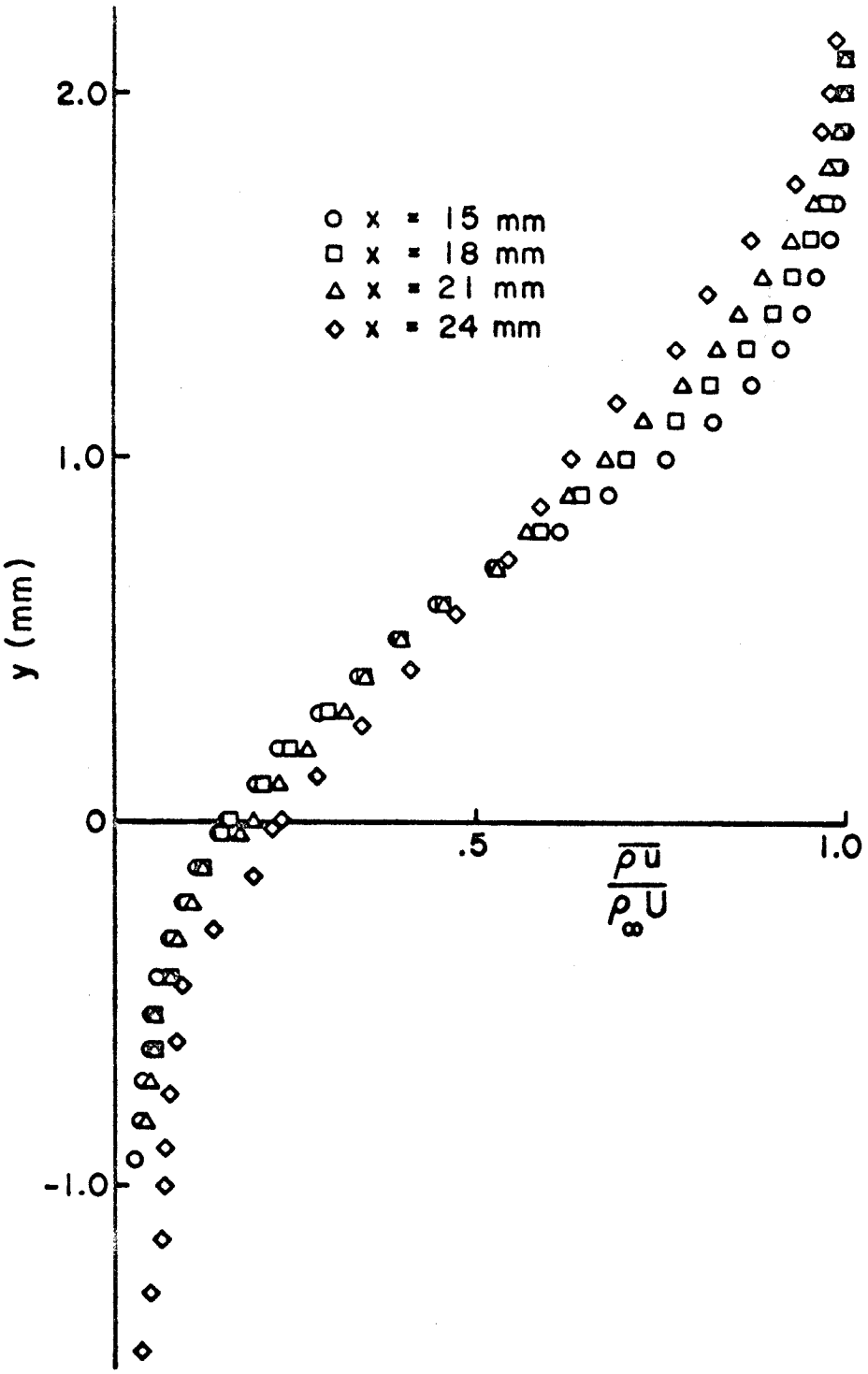

Figure 28. Mean mass flow rate profiles in region of transition to turbulence: Freon 114 into Freon 22.

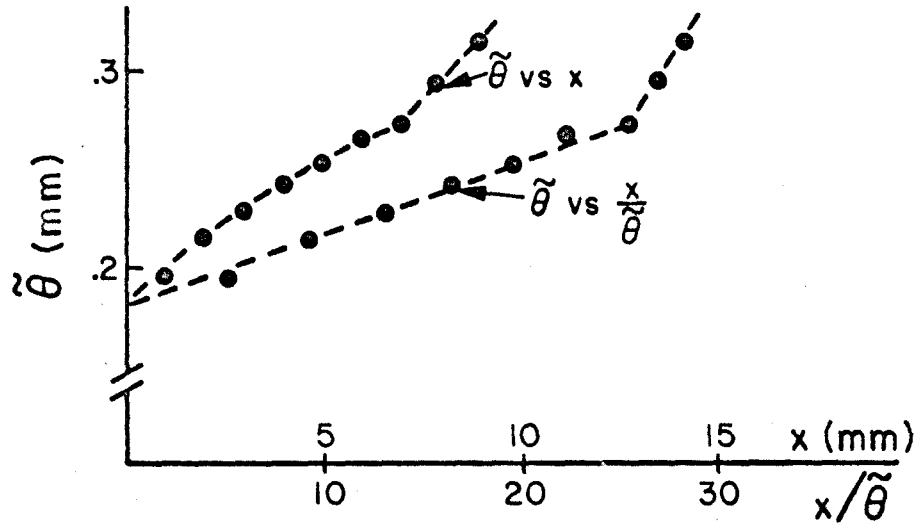

Freon 22 into Freon 114

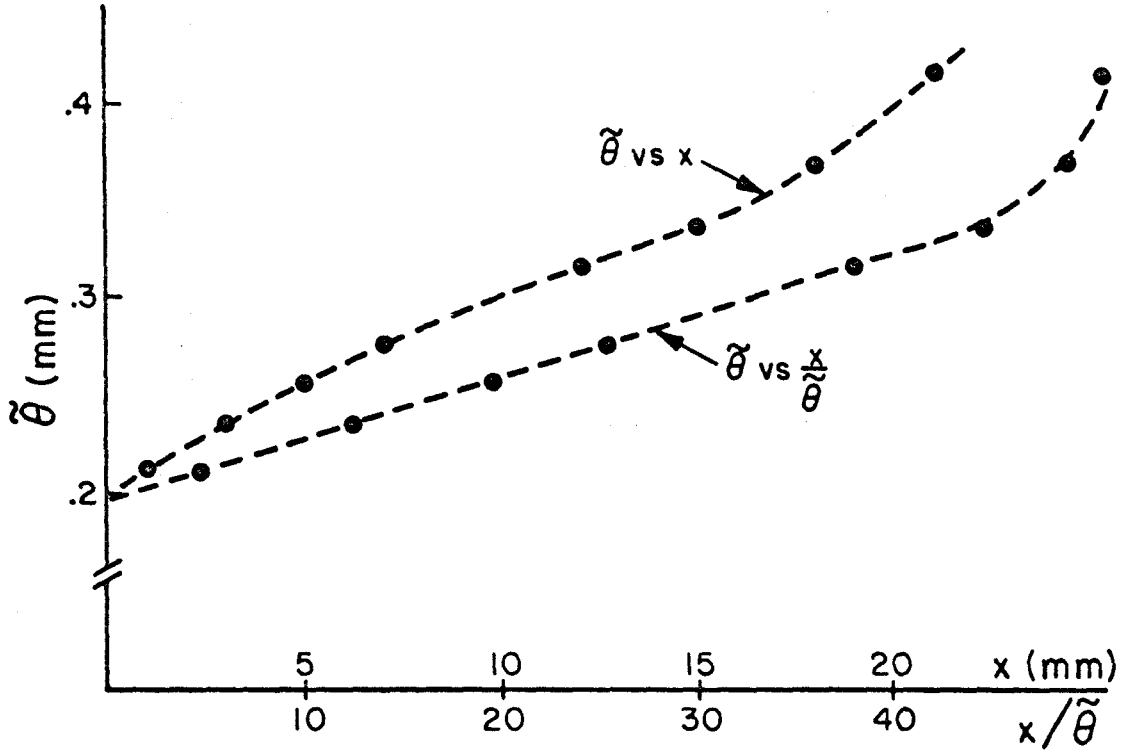

Freon 114 into Freon 22

Figure 29. Shear layer thickness as a function of downstream position.

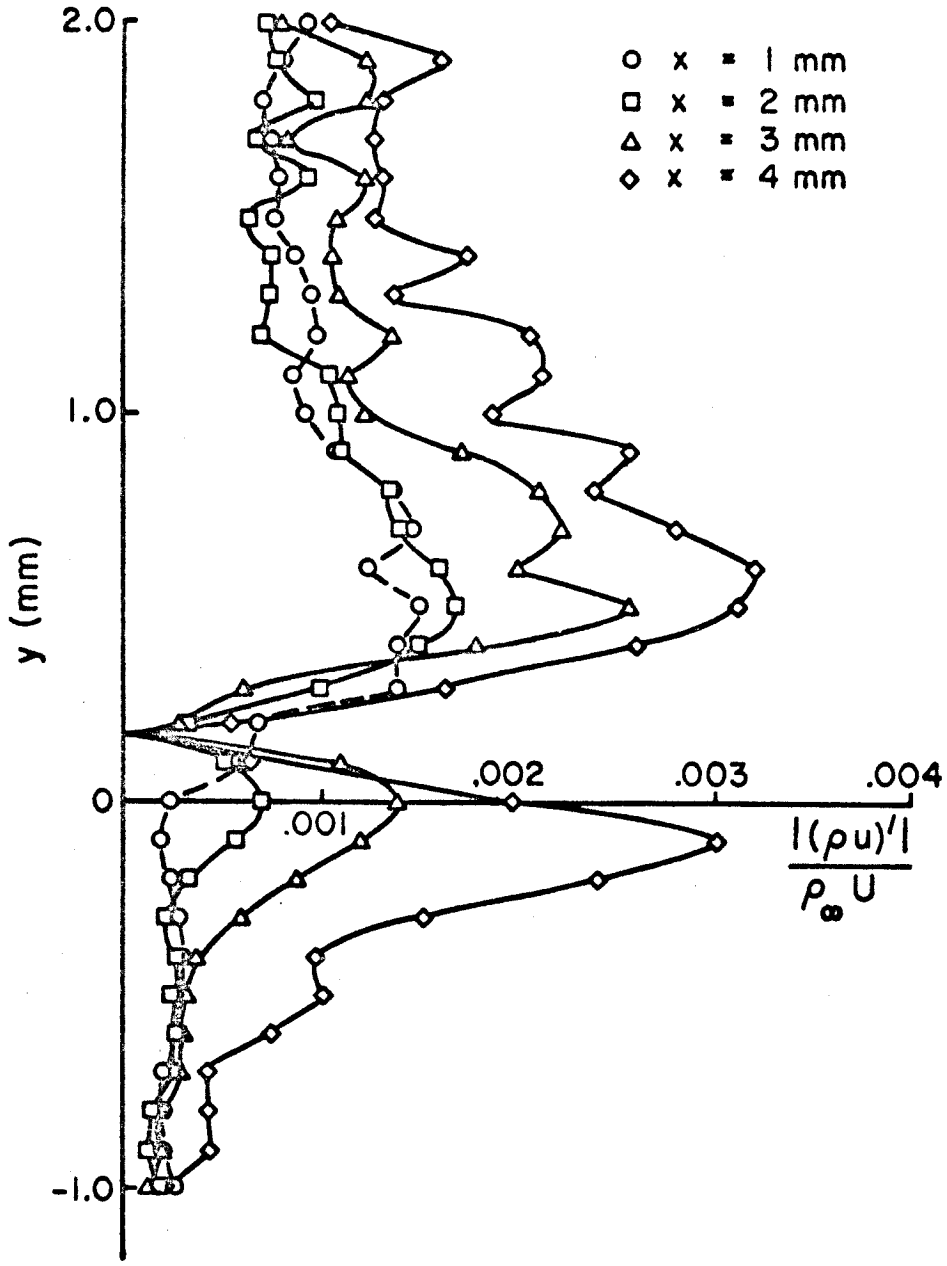

Figure 30. Amplitude of forcing frequency oscillations in the boundary layer transformation region: Freon 22 into Freon 114.

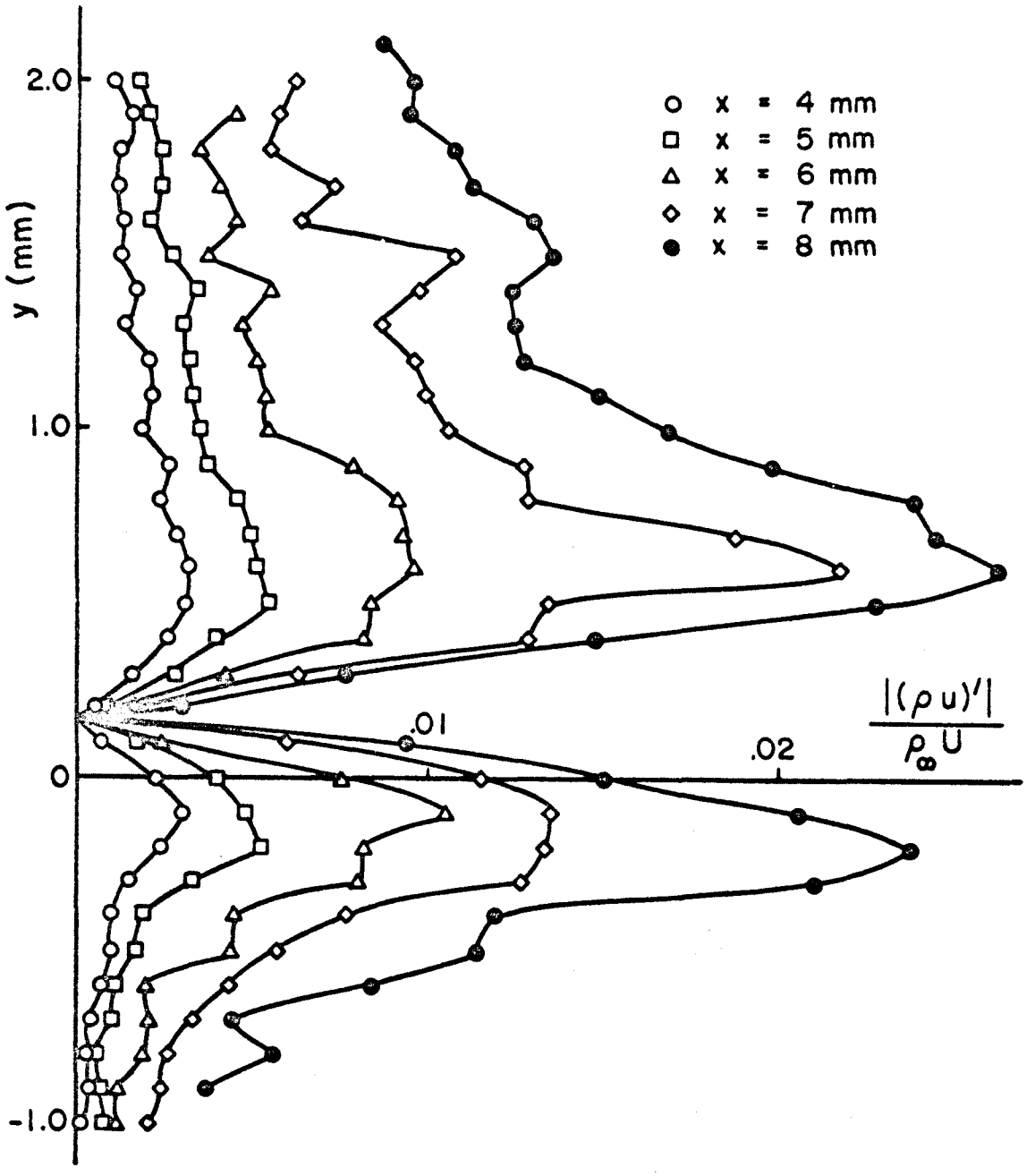

Figure 31. Amplitude of forcing frequency oscillations in the exponential growth region: Freon 22 into Freon 114.

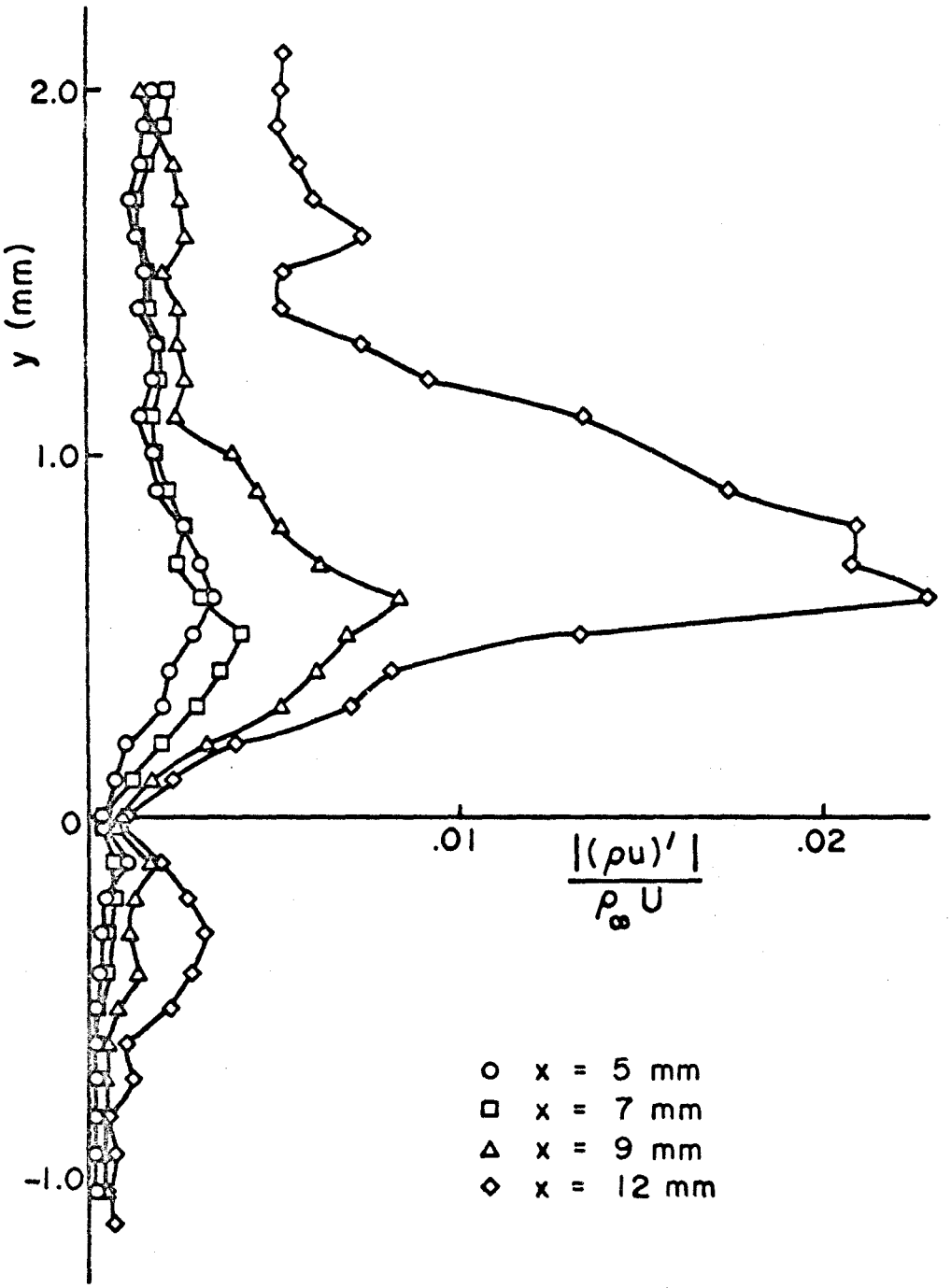

Figure 32. Amplitude of forcing frequency oscillations in the exponential growth region: Freon 114 into Freon 22.

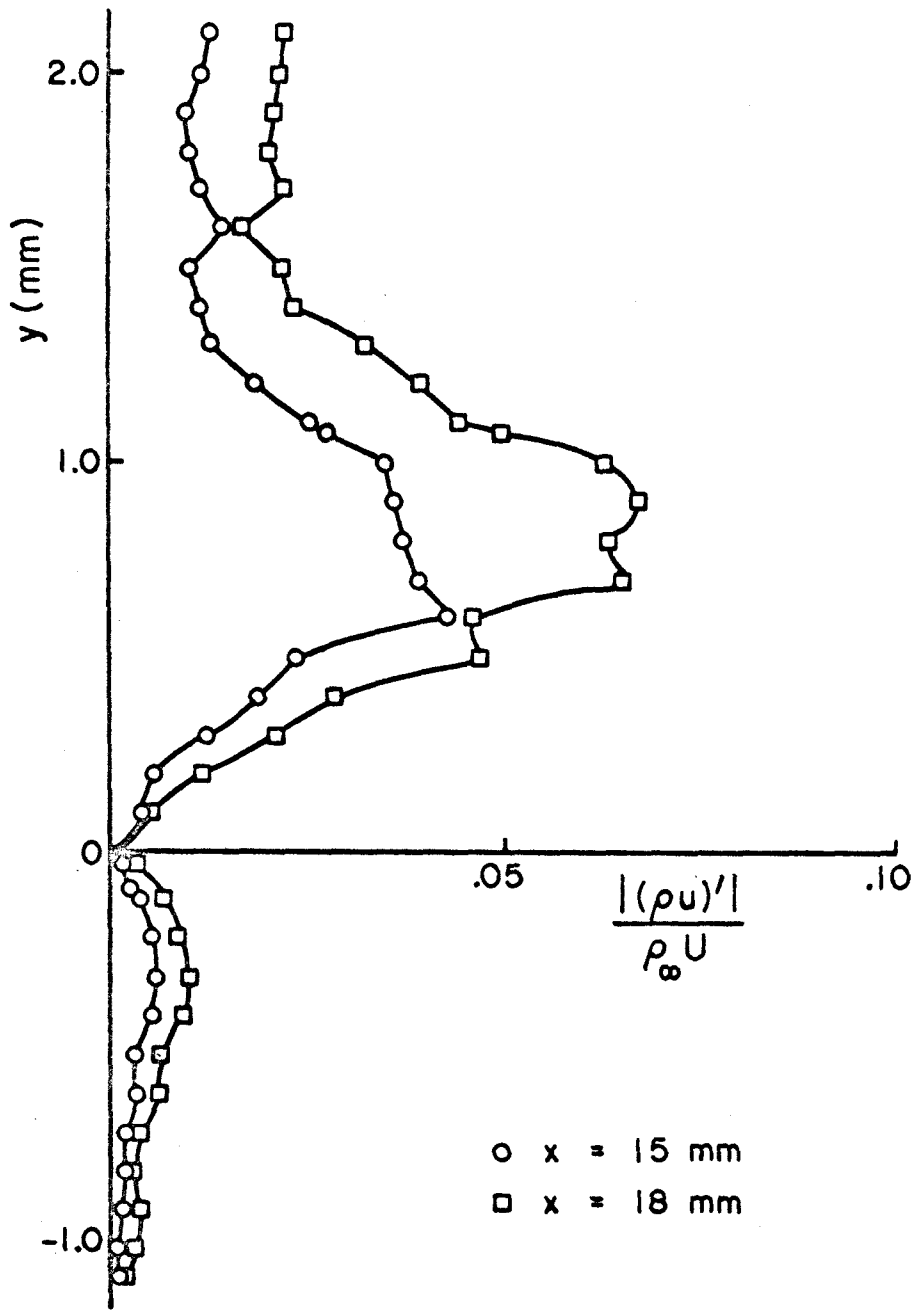

Figure 33. Amplitude of forcing frequency oscillations: Freon 114 into Freon 22.

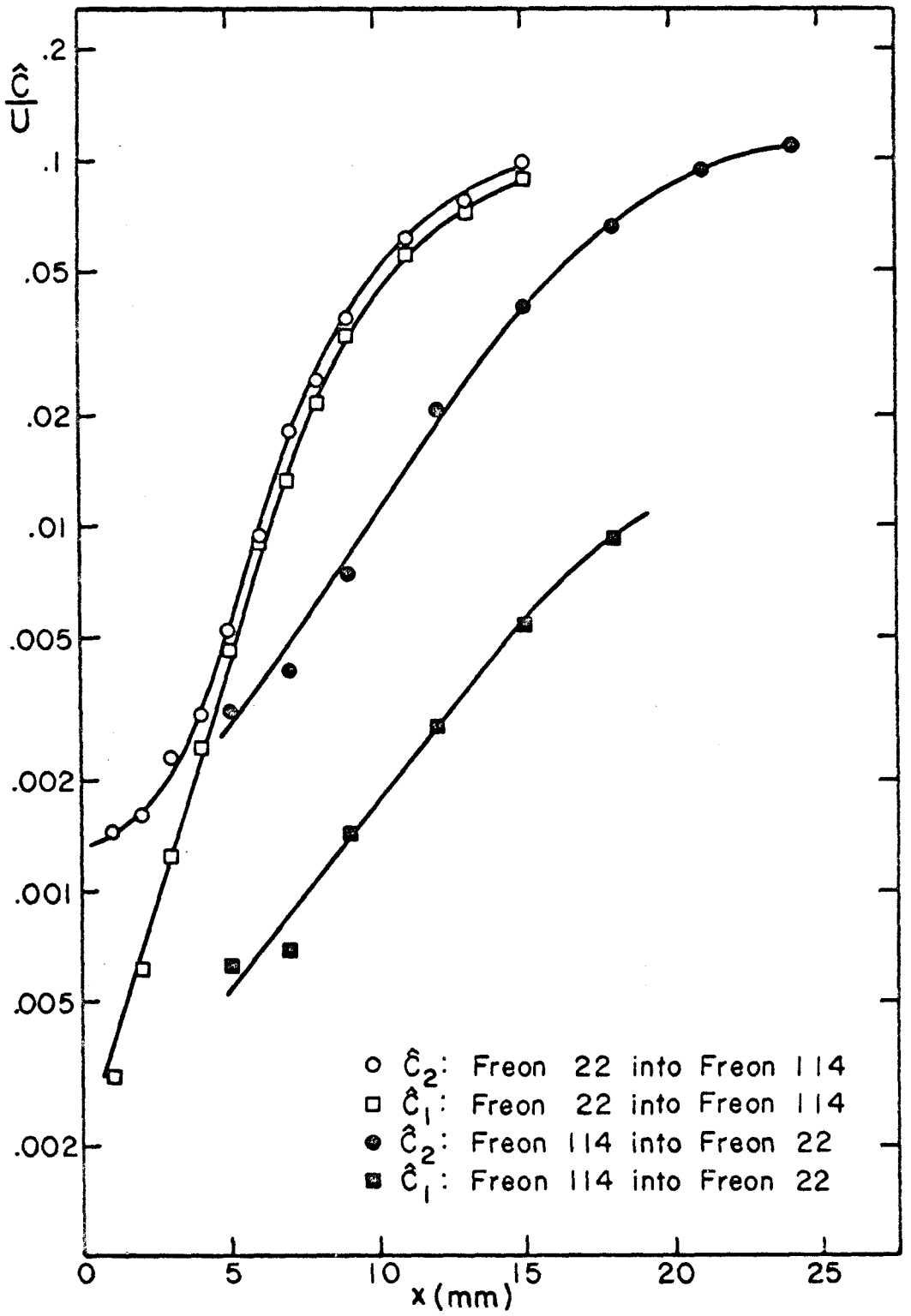

Figure 34. Downstream growth of peaks in the amplitude of forcing frequency oscillations.

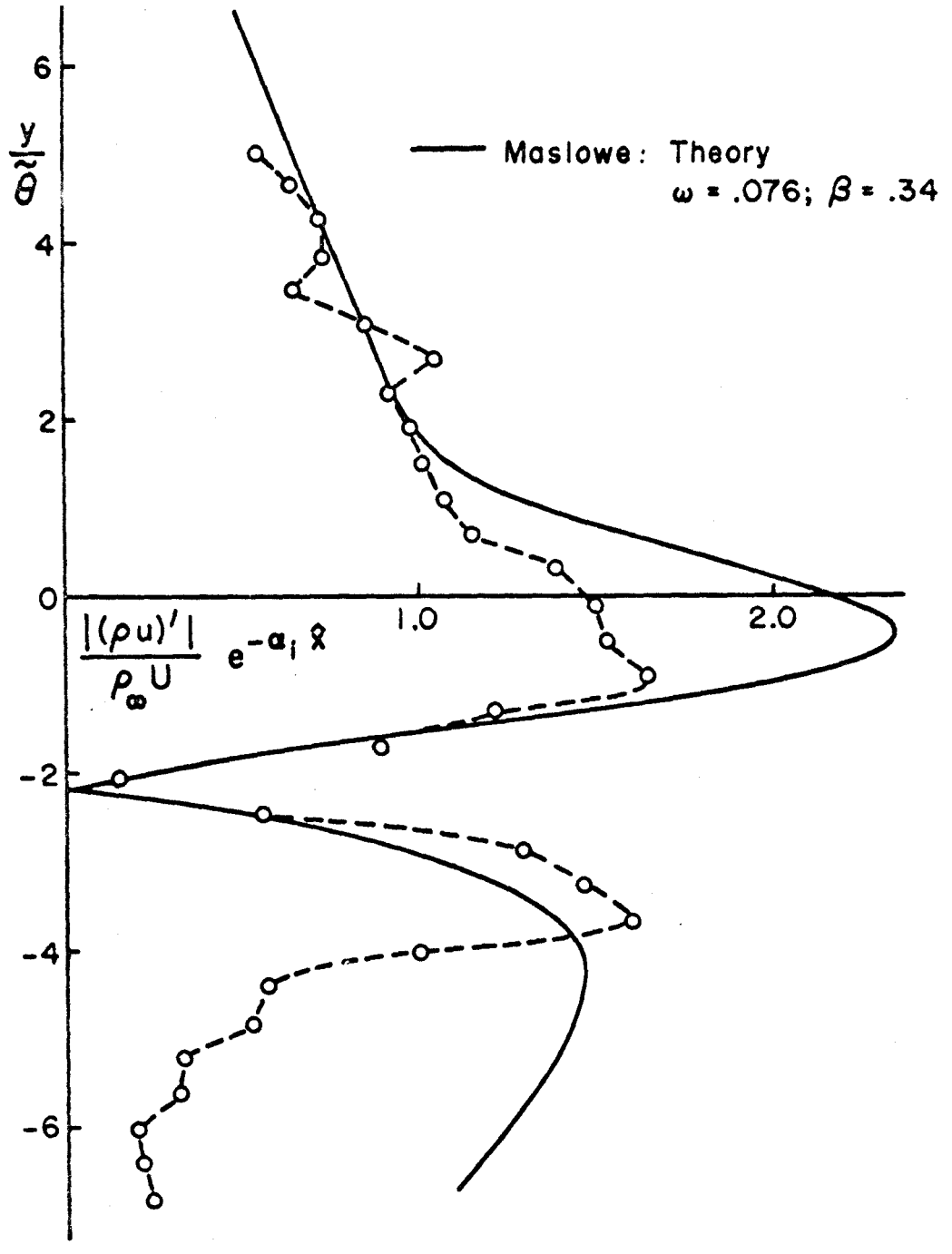

Figure 35. Comparison of experimental and theoretical amplitude distributions: Freon 22 into Freon 114, x = 5 mm.

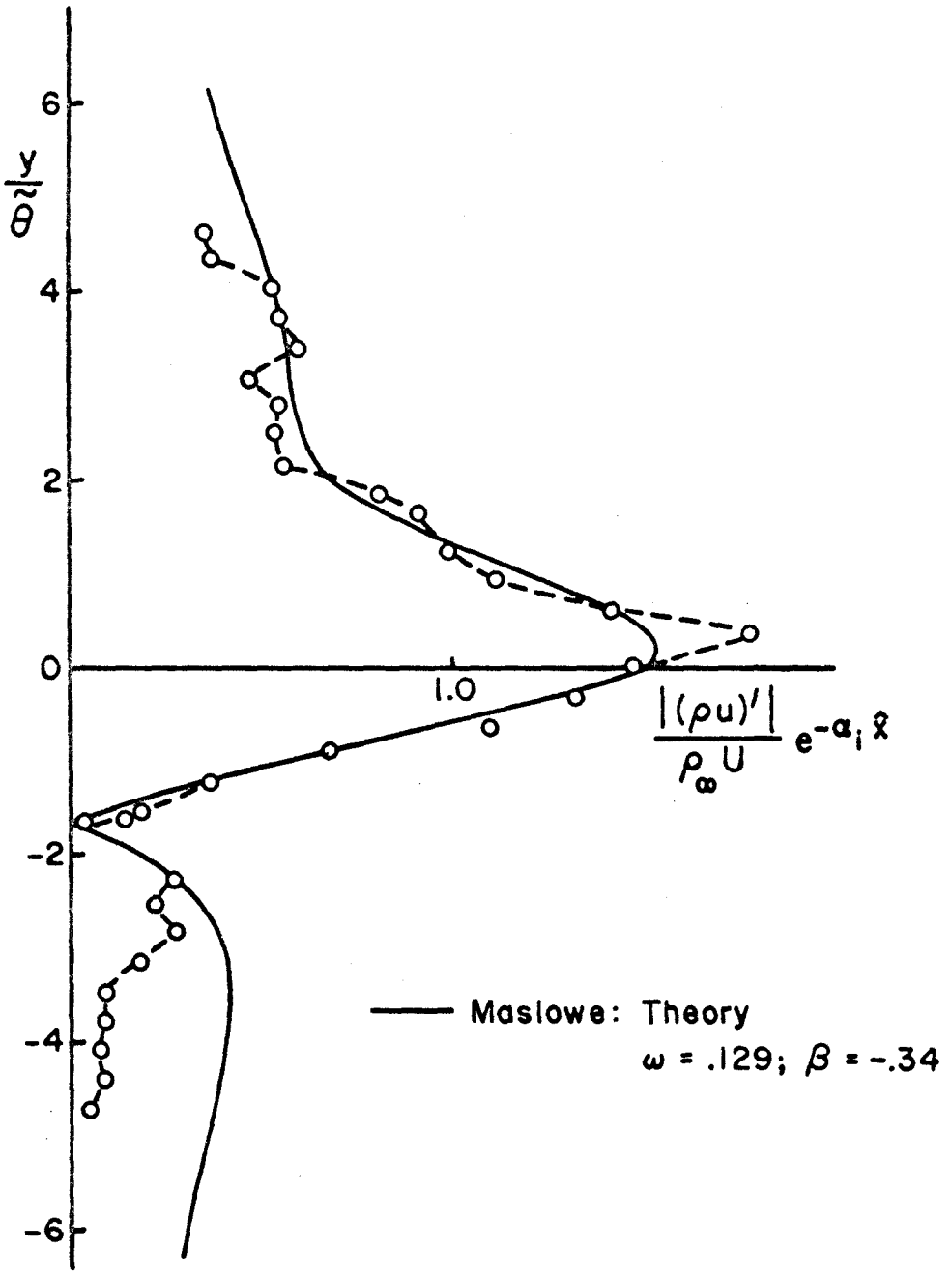

Figure 36. Comparison of experimental and theoretical amplitude distributions: Freon 114 into Freon 22, x = 9 mm.

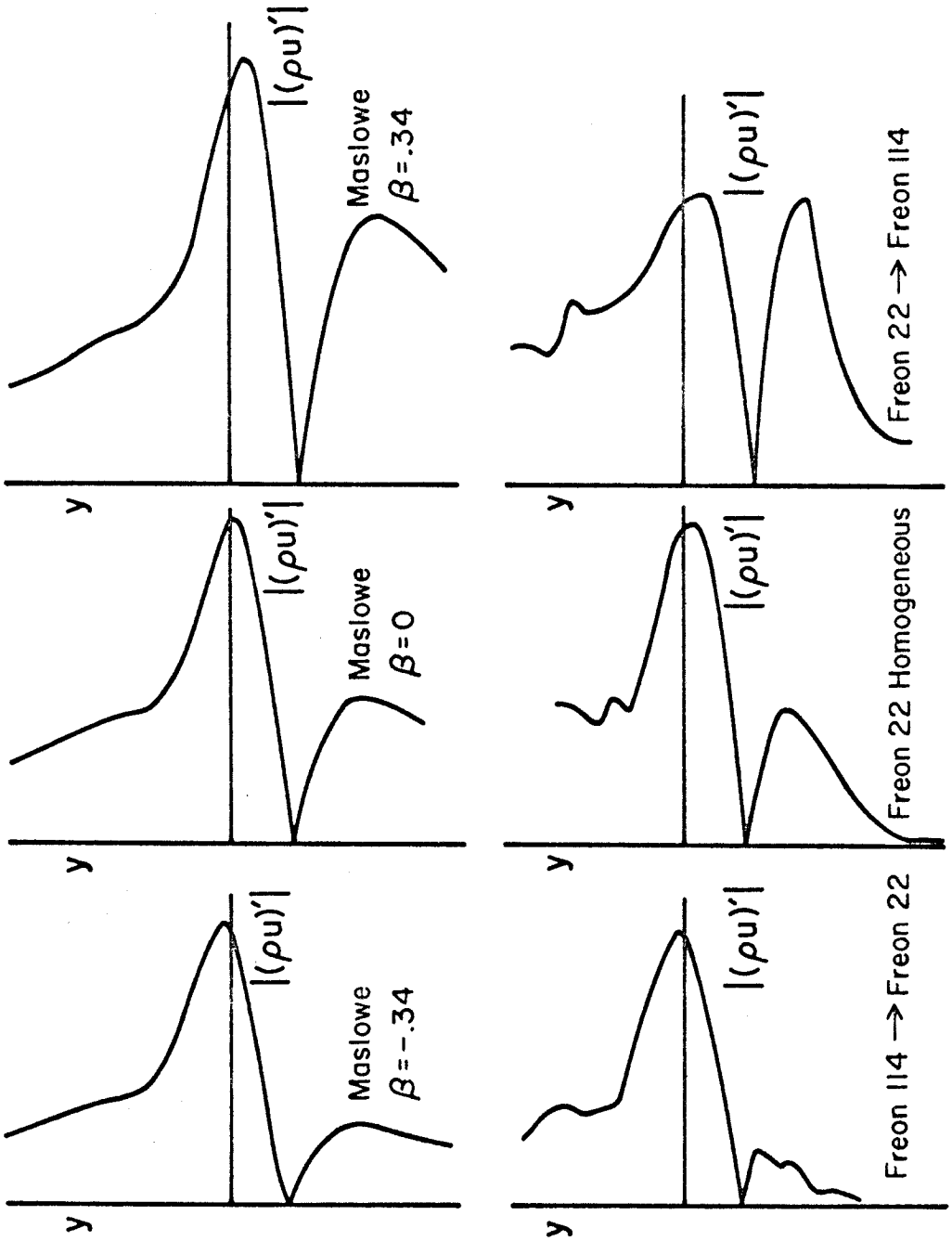

Figure 37. Effect of density gradient on theoretical and experimental amplitude distributions.

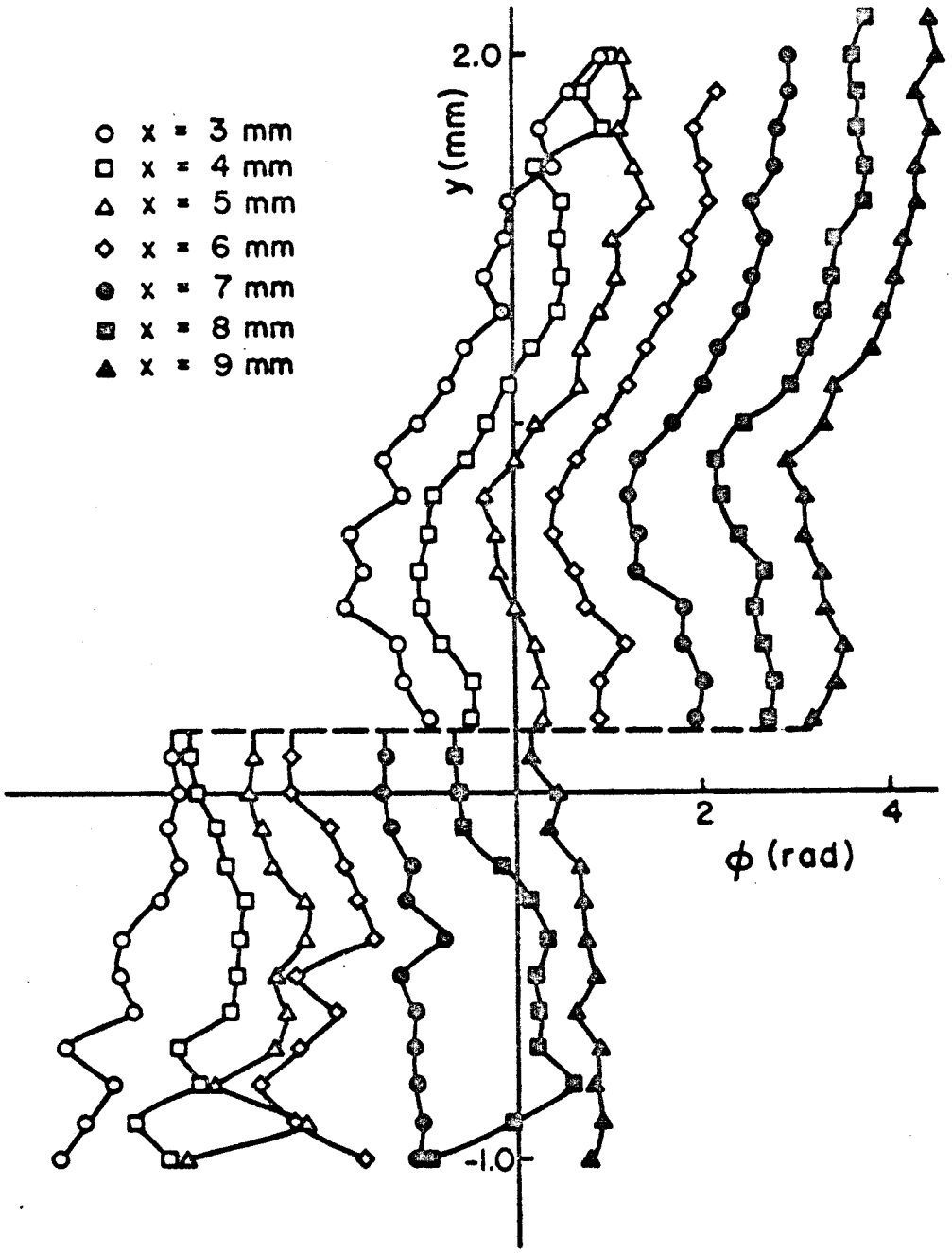

Figure 38. Phase of forcing frequency oscillations: Freon 22 into Freon 114.

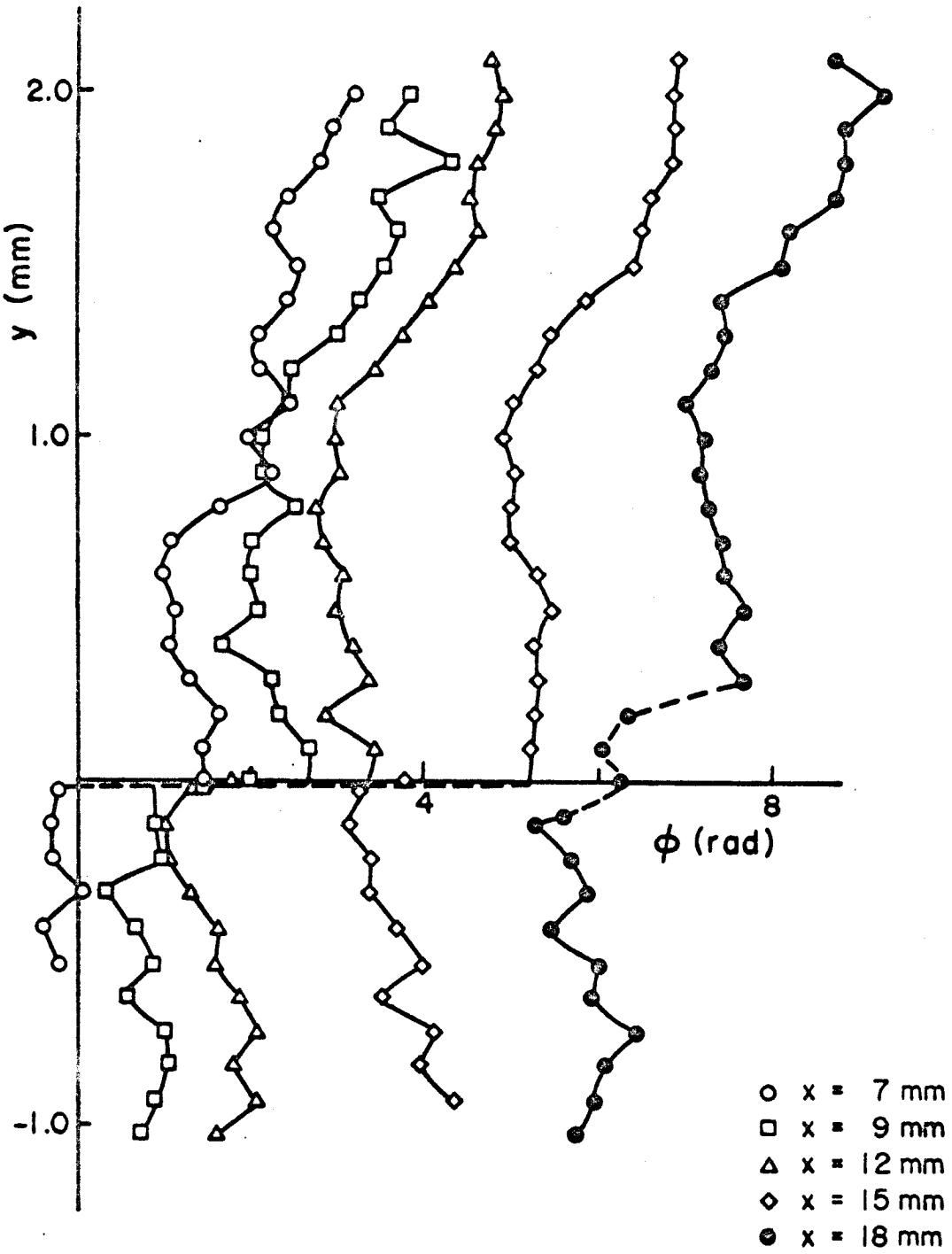

Figure 39. Phase of forcing frequency oscillations: Freon 114 into Freon 22.

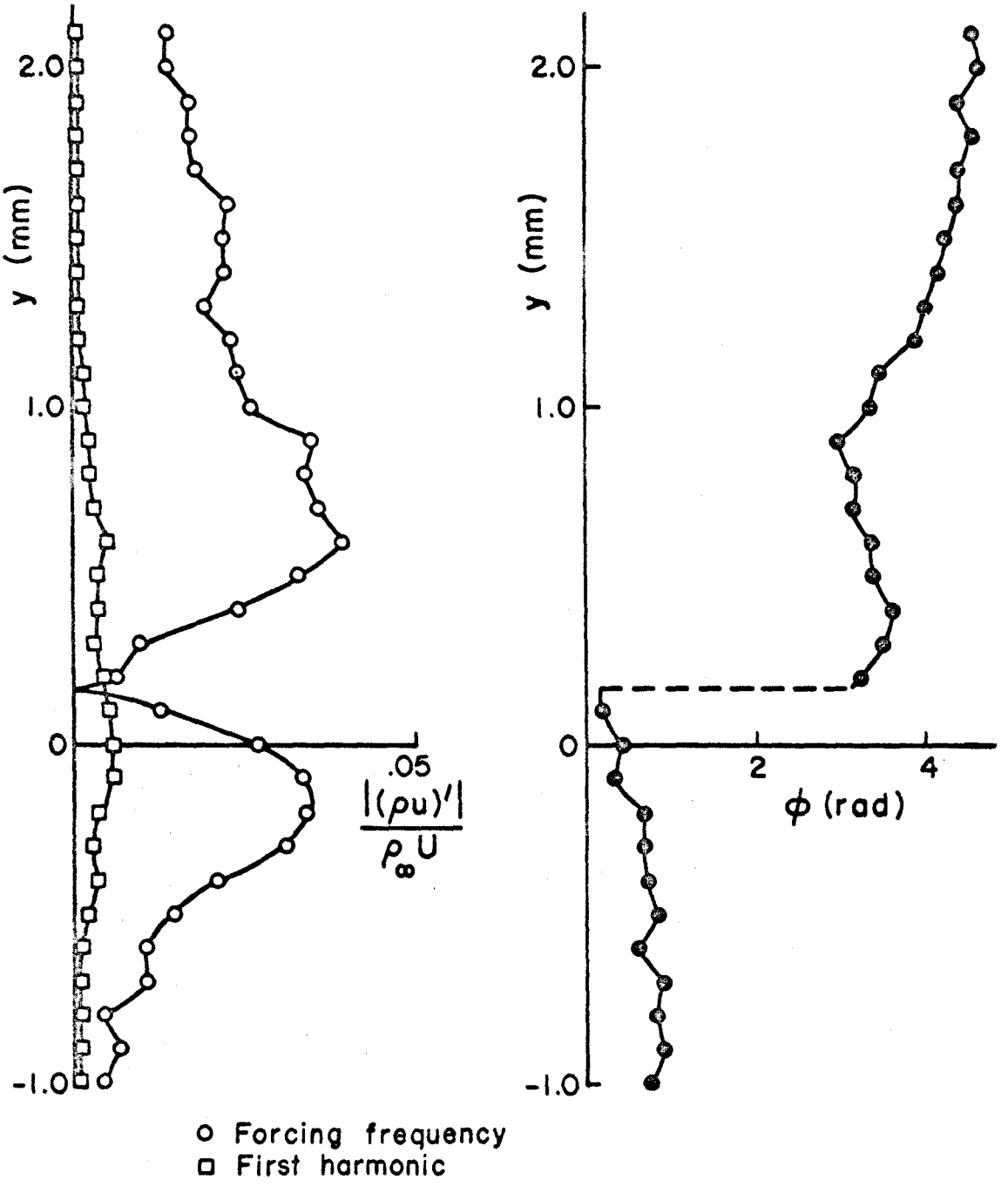

Figure 40. Forcing frequency and harmonic oscillations: Freon 22 into Freon 114, x = 9 mm.

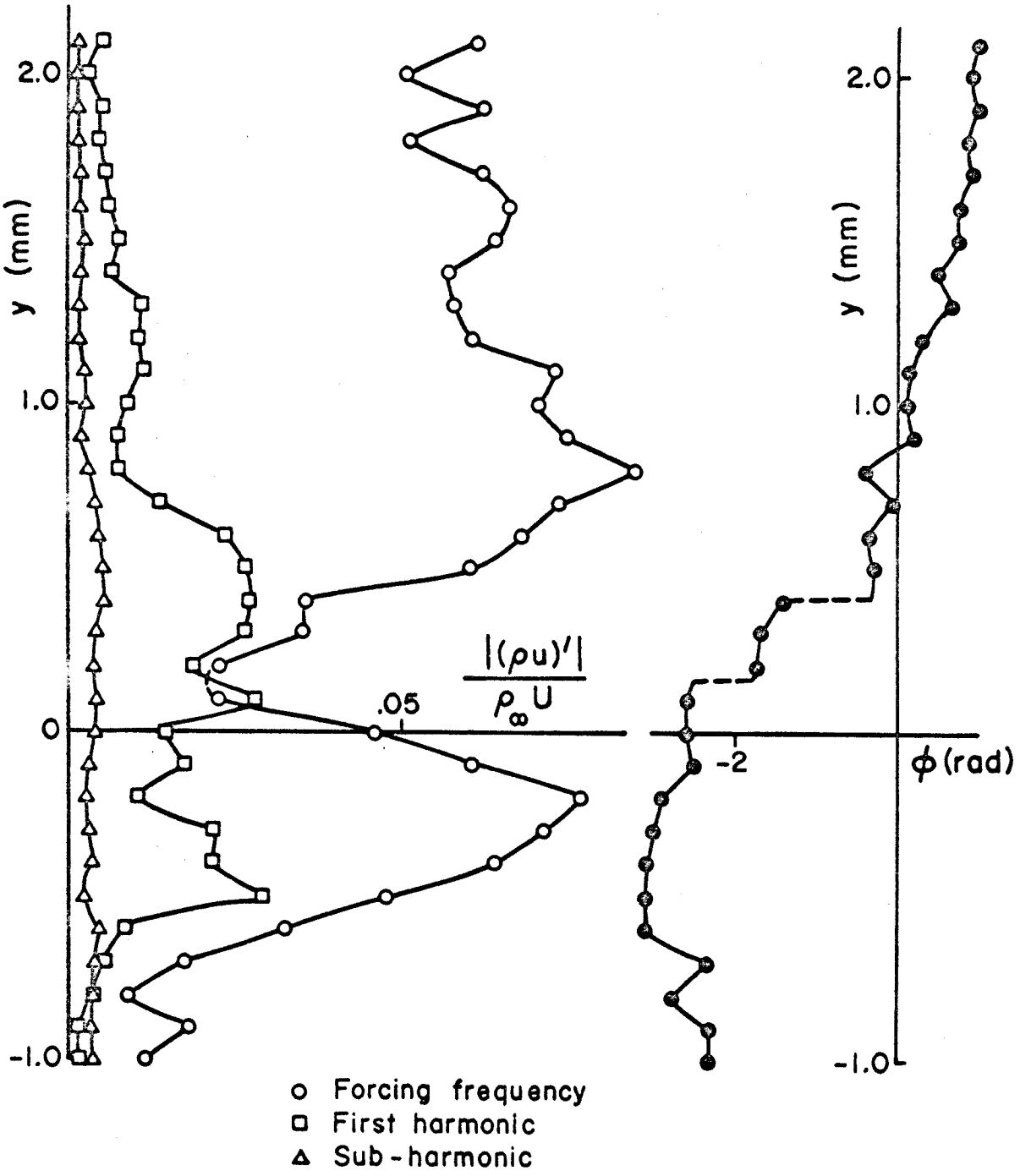

Figure 41. Forcing frequency and harmonic oscillations: Freon 22 into Freon 114, x = 13 mm.

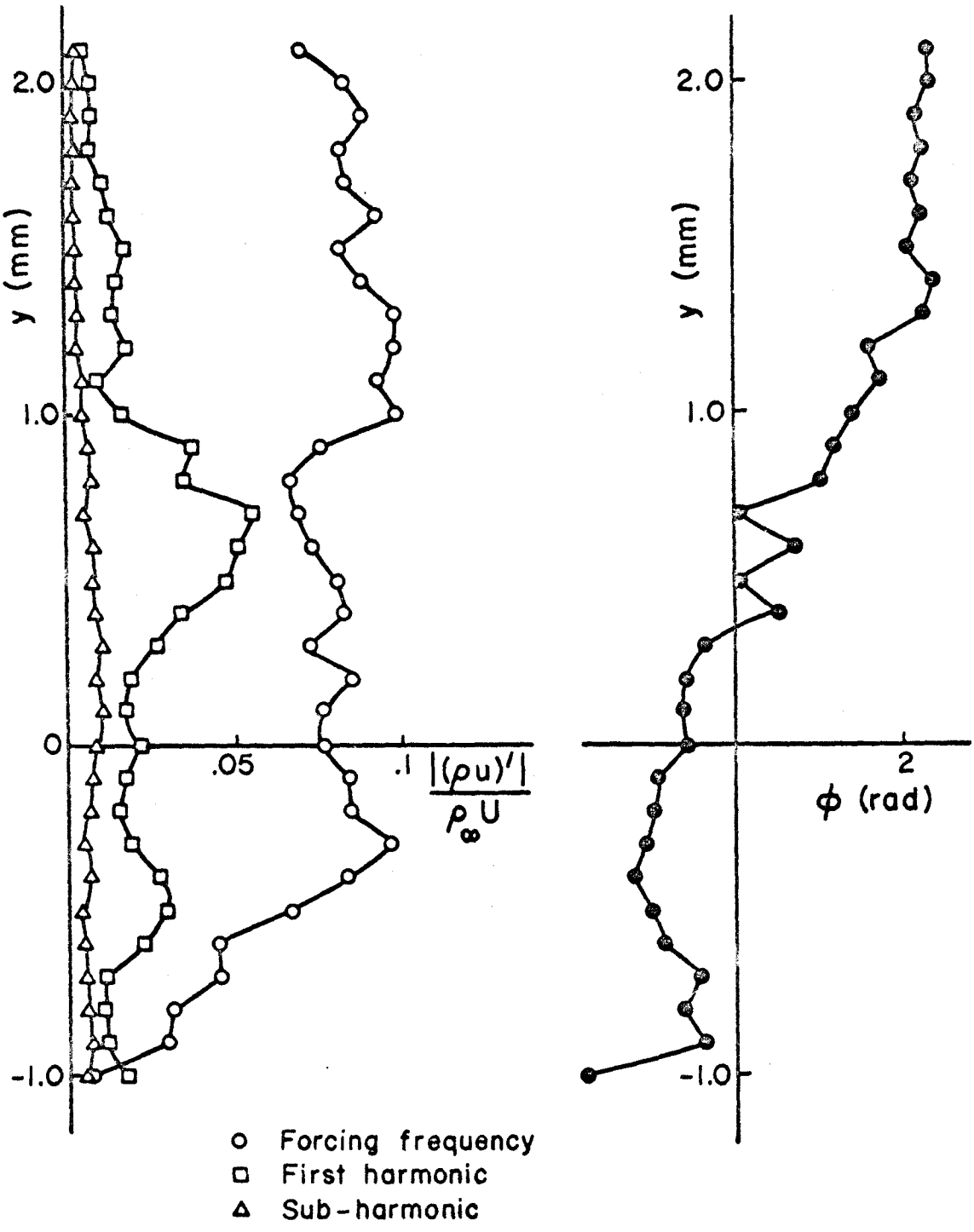

Figure 42. Forcing frequency and harmonic oscillations: Freon 22 into Freon 114, x = 15 mm.

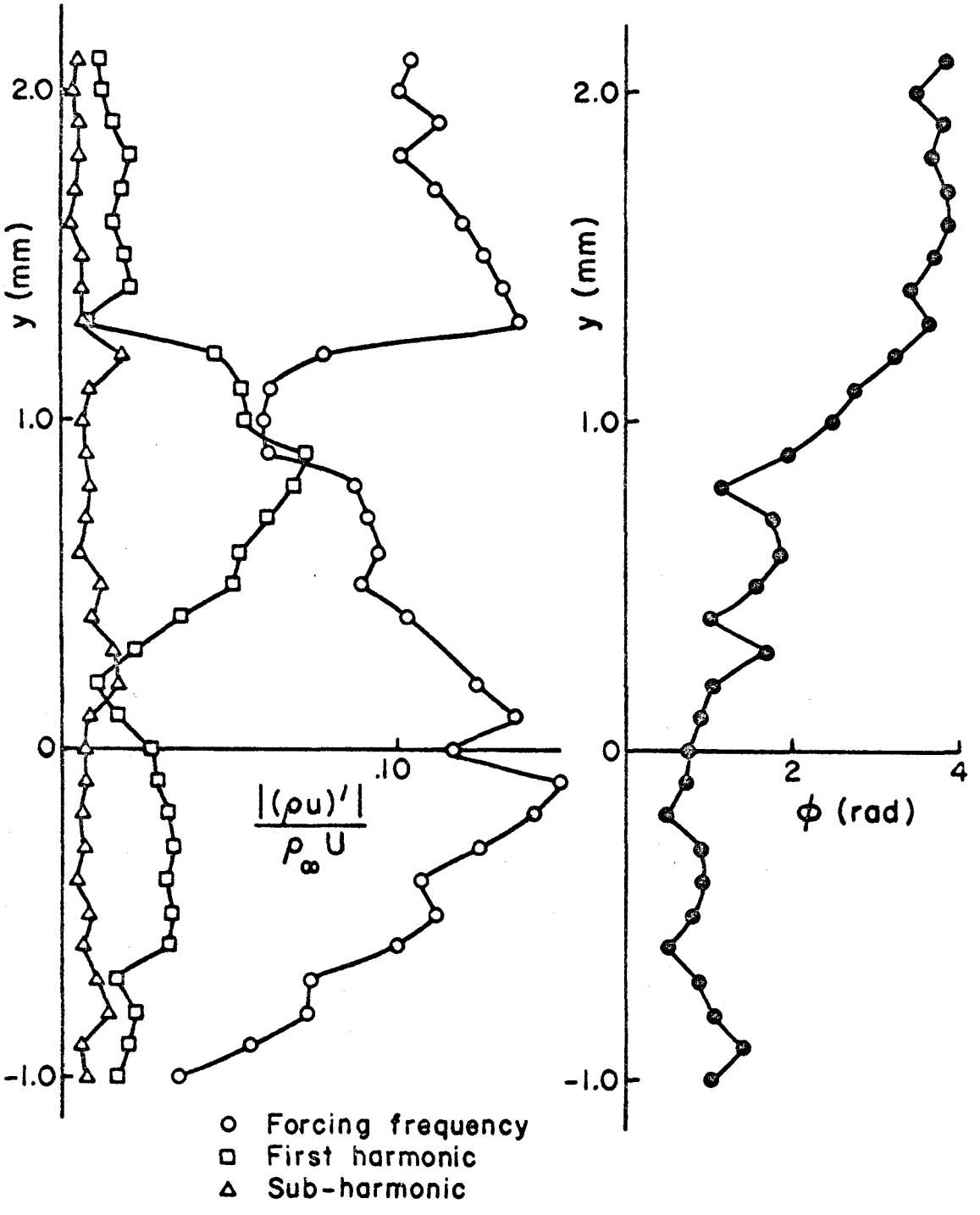

Figure 43. Forcing frequency and harmonic oscillations: Freon 22 into Freon 114, x = 17 mm.

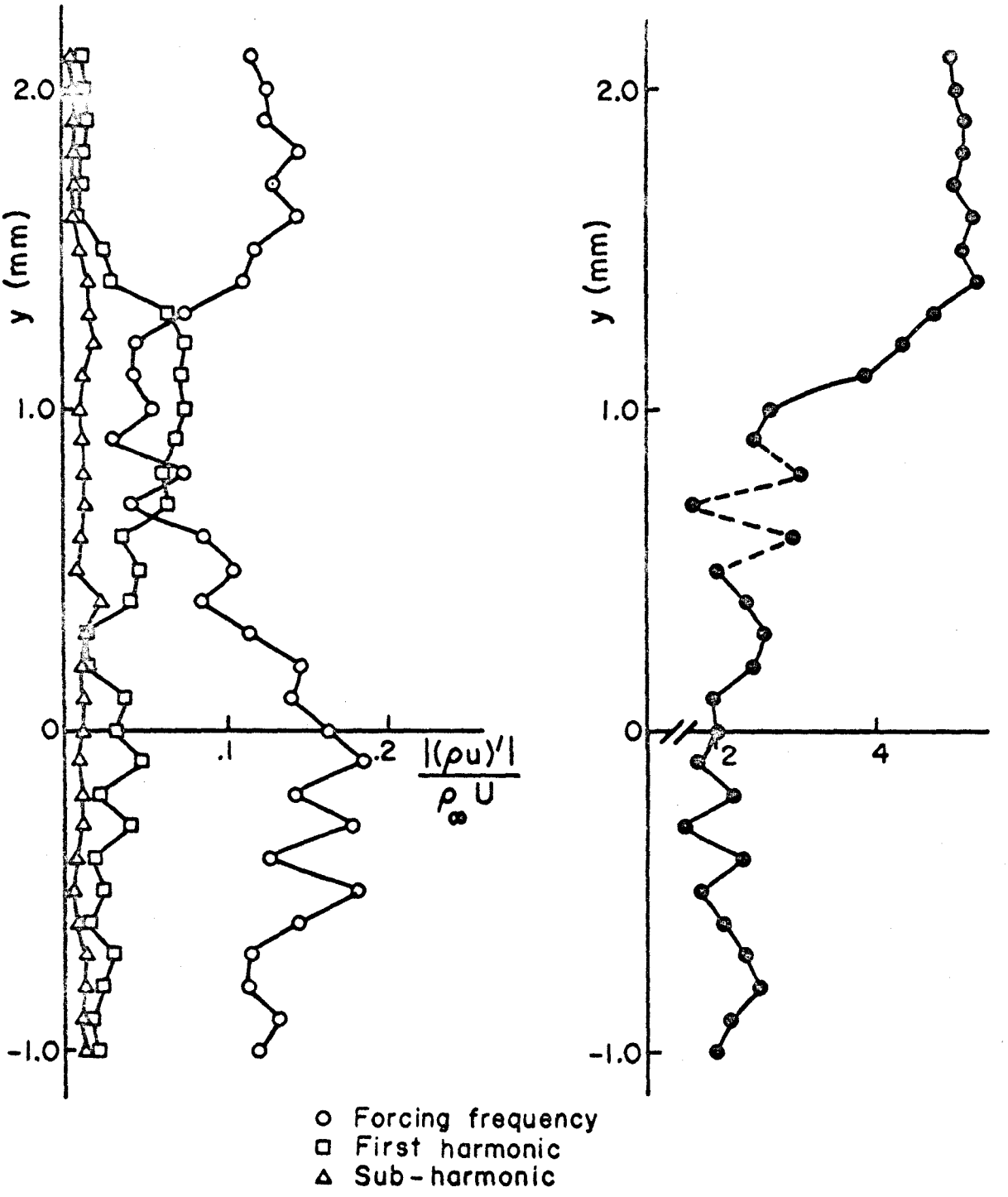

Figure 44. Forcing frequency and harmonic oscillations: Freon 22 into Freon 114, x = 19 mm.

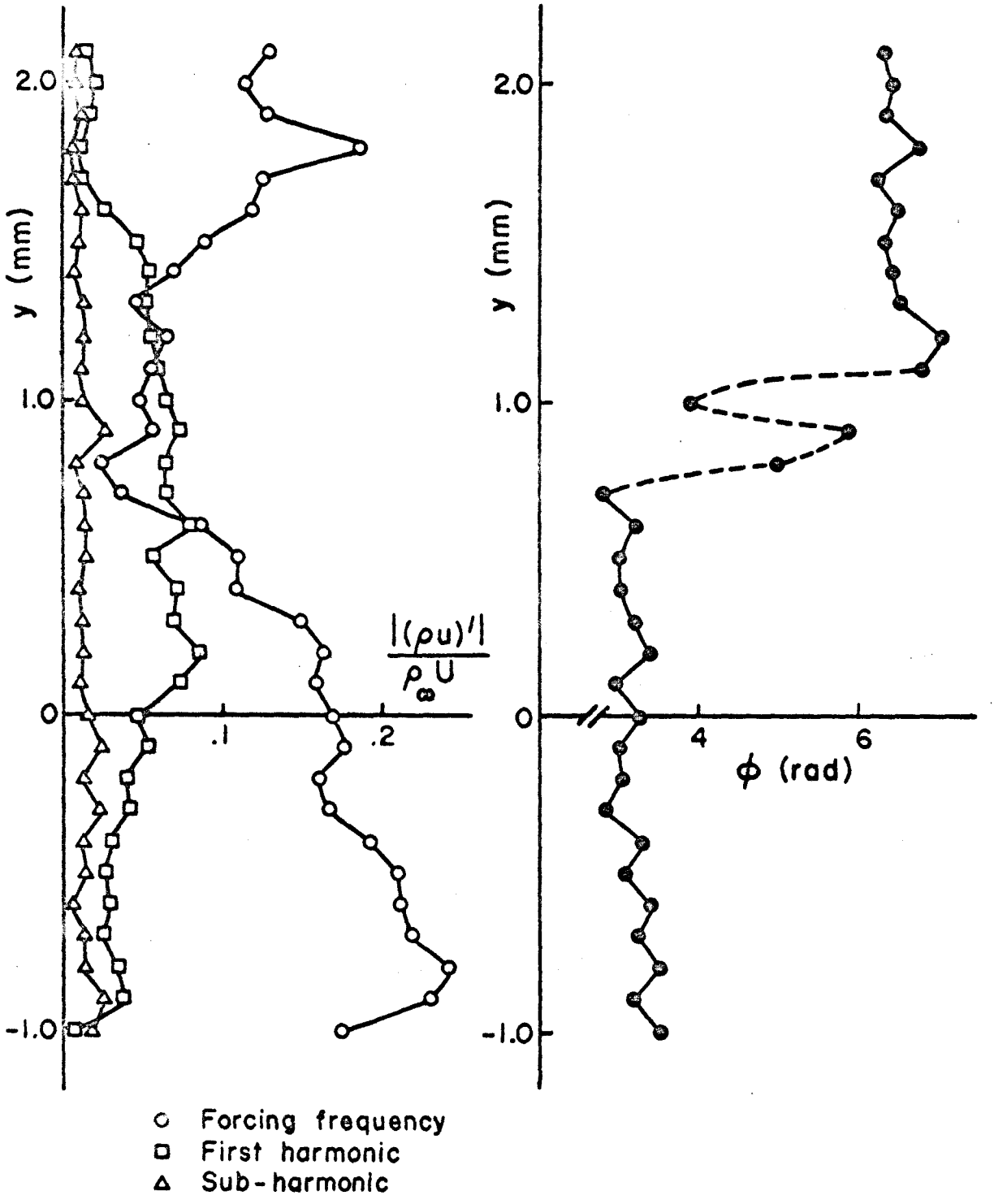

Figure 45. Forcing frequency and harmonic oscillations: Freon 22 into Freon 114, x = 21 mm.

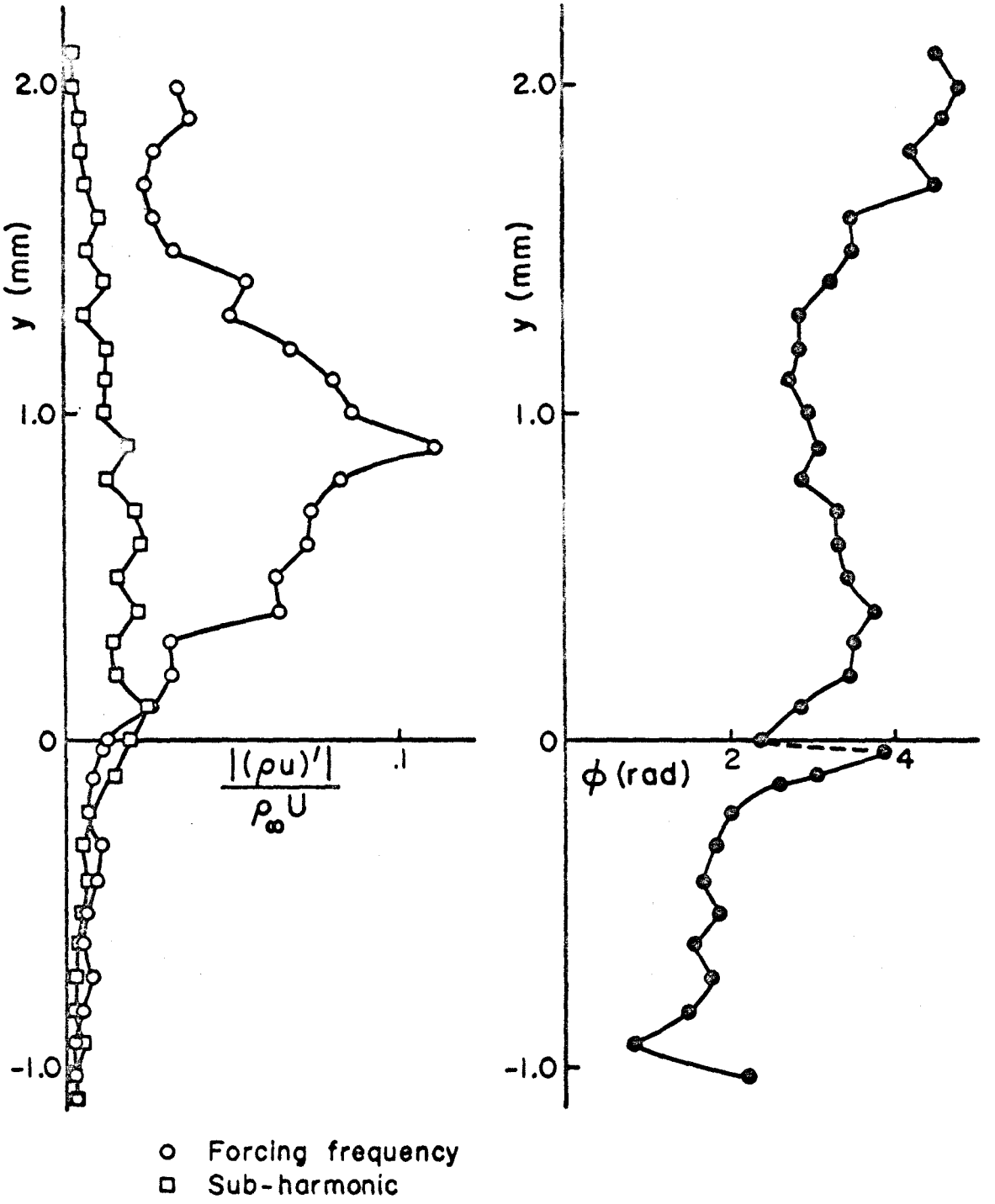

Figure 46. Forcing frequency and harmonic oscillations: Freon 114 into Freon 22, x = 21 mm.

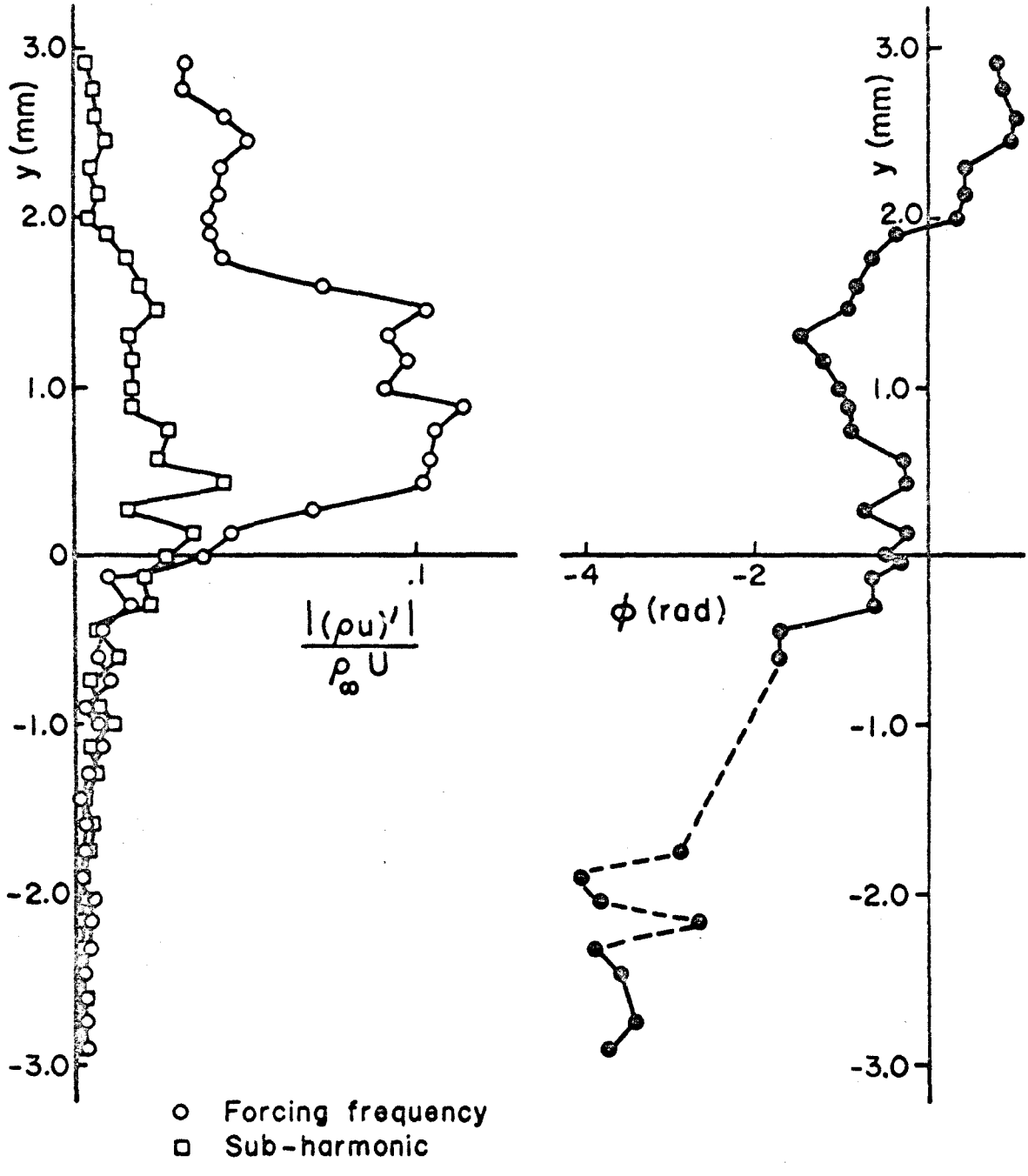

Figure 47. Forcing frequency and harmonic oscillations: Freon 114 into Freon 22, x = 24 mm.

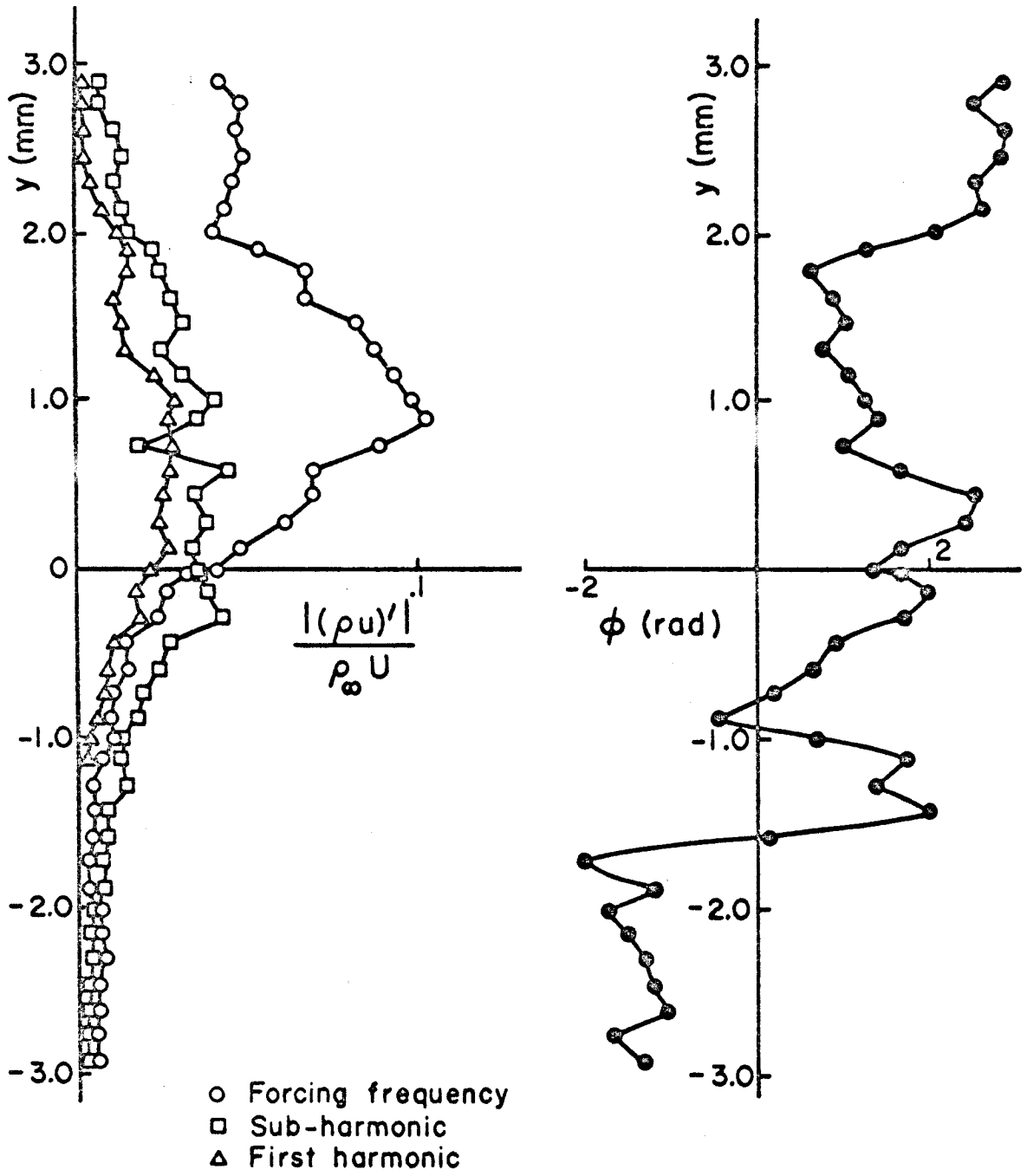

Figure 48. Forcing frequency and harmonic oscillations: Freon 114 into Freon 22, x = 27 mm.